Friedrich-Schiller-Universität Jena

Physikalisch Astronomische Fakultät

seit 1558

Impact of indium sulphide based buffer layers on the electrical properties of CIGSSe thin film solar cells

Dissertation zur Erlangung des akademischen Grades
Doktor-Ingenieur (Dr.-Ing.)

Vorgelegt dem Rat der Physikalisch-Astronomischen Fakultät
der Friedrich-Schiller-Universität Jena
im Juli 2013

von Dipl. Ing. (FH) Stephan Pohlner
geboren am 11.09.1976 in Nördlingen

Gutachter:

1. Prof. Dr. Carsten Ronning, Friedrich-Schiller-Universität Jena
2. Prof. Dr. Gerhard Franz, Hochschule für angewandte Wissenschaften München
3. Prof. Dr. Friedrich Reinert, Julius-Maximilians-Universität Würzburg

Tag der Disputation: 26.11.13

Zusammenfassung

Dünnschichtsolarzellen auf CIGSSe-Basis benötigen zwischen der Absorberschicht und der Frontelektrode eine Pufferschicht. Neben der Aufgabe der Ausbildung des *pn*-Heteroübergangs sowie der elektrischen und optischen Anpassung zwischen den benachbarten Schichten übernimmt diese Pufferschicht eine schützende Funktion des Absorbers vor den Nachfolgeprozessen. Dies wird typischerweise über eine nasschemische CdS-Beschichtung des Absorbers bewerkstelligt. Die inhärente Toxizität und die Prozessführung machen diese Verbindung jedoch für die kommerzielle Nutzung unattraktiv. Eine viel versprechende Alternative zu CdS ist die Verwendung von In_2S_3.

In der vorliegenden Arbeit werden zunächst die strukturellen, chemischen und optischen Eigenschaften von In_xS_y-Pufferschichten in Abhängigkeit ihrer S/In-Verhältnisse analysiert. Die beobachteten Änderungen werden anhand von Kennlinien-Messungen mit den elektrischen Eigenschaften von entsprechenden Solarzellen in Verbindung gebracht und diskutiert. Es wird gezeigt, dass der optimale Wirkungsgrad für einen In-Anteil von etwa 42 at% im Puffer erreicht wird. Abweichend von dieser Zusammensetzung tritt sowohl zu In- als auch zu S-reicheren Schichten eine Degradation des Wirkungsgrades auf. Anhand der Auswertung der zugehörigen Sekundärparameter wird ein Modell entwickelt, welches das beobachtete Verhalten erklärt und auf die Bandanpassung an der Absorber-Puffer-Grenzfläche zurückführt. Bei einer optimalen Zusammensetzung des Puffers tritt eine schwach ausgeprägte Typ-Inversion der Absorberoberfläche auf. Des Weiteren ergibt sich bei S-reicheren Schichten aufgrund einer ausgebildeteren Kristallinität eine erhöhte Cu-Eindiffuion aus dem Absorber, welche die Ladungsträgerdichte im Puffer stark reduziert. Dies führt zu einem Verlust der Inversion und verschlechtert die elektrischen Eigenschaften der Solarzellen aufgrund einer höheren Grenzflächen-Rekombination. Bei einer Zunahme des In-Anteils im Puffer erhöht sich der Anteil an In_6S_7 und InS-Phasen, welche ebenfalls die effektive Ladungsträgerdichte reduzieren und die Inversion aufheben.

Da unter dem Einsatz eines reinen In_xS_y-Puffers eine erhebliche Diskrepanz zu den erreichbaren Wirkungsgraden mit einem CdS-Puffer zu verzeichnen ist, wurde in dieser Arbeit ein Dotierprozess mit Na_2S entwickelt. Die strukturellen, optischen und elektrischen Eigenschaften des hierdurch verbesserten Puffers erlauben eine deutliche Verstärkung der Typ-Inversion des Absorbers, was eine vollständige Schließung der beobachteten Wirkungsgradlücke auf einem Niveau von bis zu 14.9 % für ein 10x10 cm² Modul ermöglichte.

Abstract

Thin film solar cells on CIGSSe basis require the utilization of a buffer layer between the absorber and the front electrode. Besides the task of the formation of the *pn*-hetero-junction as well as the electrical and optical alignment between the neighbouring layers, the buffer protects the absorber during subsequent process steps. Commonly, this is accomplished by a wet chemical deposition of CdS onto the absorber. However, the inherent toxicity and the process management diminish the attractiveness of this compound for a commercial application. A promising alternative to CdS is the utilization of In_2S_3.

The present work analyses the structural, chemical and optical properties of In_xS_y buffer layers as a function of their S/In ratio. The observed changes are associated to the electrical properties of solar cells with the help of the respective diode characteristics and discussed, subsequently. It is shown, that the optimal efficiency is reached at an In-content of about 42 at%. Any deviation from this composition results in a degradation of the efficiency towards both, In- and S-richer films. By evaluating the secondary parameters, a model is developed that explains the observed behaviour, ascribing it to the band alignment at the absorber-buffer-interface. An optimal composition is connected to a slight type inversion of the absorber's surface. Due to a more pronounced crystallinity for S-rich layers, an increased Cu-diffusion from the absorber is induced, which reduces the charge carrier density inside the buffer. This leads to a loss of the inversion and deteriorates the electrical properties of the solar cells because of enhanced interface recombination. For higher In-contents inside the buffer the proportion of In_6S_7 and InS phases increases, which also reduces the effective charge carrier density and diminishes the inversion.

Since the utilization of a pure In_xS_y buffer leads to a significant discrepancy in the achievable efficiency compared to CdS, a doping process for the buffer layer has been developed in this work, using Na_2S. The structural, optical and electrical properties of the improved buffer allow a considerable increase of the absorber's type-inversion, enabling a complete closure of the observed efficiency gap on a level of up to 14.9 % for a 10x10 cm² module.

Table of contents

1 Introduction

In recent years, photovoltaic (PV) generation of electricity has enjoyed tremendous growth rates due to rising awareness of climate change and driven by major funding projects like Japan's "Residential PV System Dissemination Programme" in 1994 [1] or the renewable energy law [2] in Germany. This resulted in an enormous increase in annually installed nominal PV power in the last years: On a world wide scale, a nominal power of more than 16.6 GW_p has been installed within the year 2010 and 27.7 GW_p within 2011 [3]. In total, this increased the world wide accumulated installed photovoltaic capacity to about 67.4 GW_p by the end of 2011. Due to this strongly growing market, the PV module producing companies ramped up their production capacities, while many new companies have been additionally founded. The intensifying competition for market shares eventually lead to an overheating of the sector and the module producing companies increased their overcapacity from nearly 2 GW_p in 2008 to more than 10 GW_p in 2010, which can be deduced from Fig. 1.

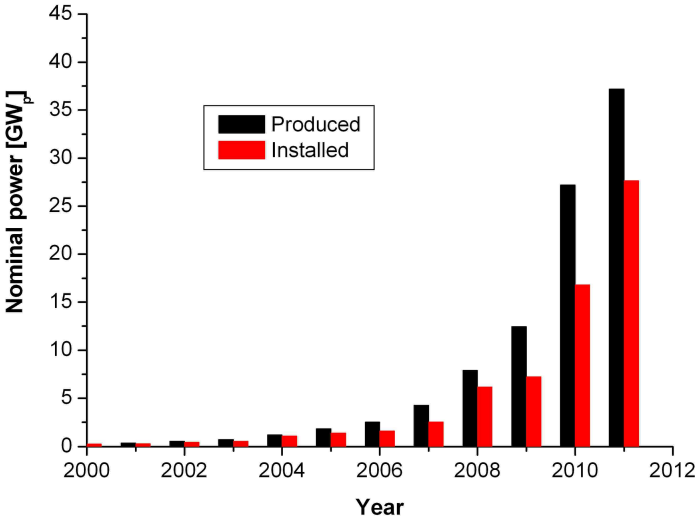

Fig. 1: Comparison of worldwide produced and installed nominal solar module power from 2000 to 2011 after [3-6].

As a result of this increasing overproduction, an uninstalled capacity of nearly 27 GW_p has been accumulated from 2008 to 2011, which resulted in a drastic drop in achievable price per W_p of about 45 % in 2011 and of about 75 % within the timeframe from 2008 to 2012 [7]. Consequently, the manufacturers are hardly able to adapt their facilities to the changing requirements in cost recovery. Hence, the PV industry is expected to experience a "shake out" during which a significant fraction of the module producers will be forced to exit the market until 2014 [8]. However, since the potential in Europe and

the emerging markets in Africa and Asia are by far not saturated yet, it is still assumed that PV will play a substantial role in providing a growing contribution for the world's demand in renewable energy. For those manufacturers of solar modules surviving the "shake out" it hence becomes essential to prepare their current and future factories in a way that they are able to achieve grid parity without the need of governmental subsidies.

Throughout the PV industry many concepts, techniques and material systems are known and do find application to build up solar modules [9]. Comparing the most relevant ones, the mono- and multicrystalline silcon (mc-Si) based technology constitutes the largest fraction in annually produced solar modules with currently about 86 % [10]. The remaining 14 % are apportioned in the thin film industry. In this context, the differences in feasibility of low cost production and sustainability indicators like the energy payback time (EPBT) and the green house gas emission become very relevant for the applicability in the market. Within the thin film industry the CIGS technology, based on the compound semiconductor consisting of the elements copper, indium, gallium and selenium, is known to be very competitive with respect to the mentioned requirements [11]. The technology's EPBT of about 1 to 2 years is very short compared to the module life time of about 25 years [12, 13]. Moreover, the gainable conversion efficiency is already comparable to solar cells based on mc-Si. The present record of 20.3 % for the best CIGS solar cell [14] and 20.4 % for mc-Si [15, 16] has been reached by the "Zentrum für Sonnenenergie- und Wasserstoff-Forschung" and by the "Fraunhofer-Gesellschaft ISE", respectively. The wider spread thin film technologies using either amorphous silicon (a-Si) or cadmium telluride are not yet capable of gaining such high conversion efficiencies. For these approaches Oerlikon Solar Lab reached 10.1 % on an a-Si single junction [17] and First Solar 18.7 % with a CdTe solar cell [18].

The module producer AVANCIS GmbH employs the CIGS technology in combination with the addition of sulphur to achieve a band gap grading through the absorber layer [19]. Based on this technology AVANCIS formerly achieved a world record for independently certified 30x30 cm² modules with a conversion efficiency (aperture) of 15.8 % [20]. The current certified world record of 15.7 % (total area) for a production size module with a dimension of 1.09 m² is held by TSMC Solar [21]. According to internal measurements on respective modules this value correlates to an aperture efficiency of 17.6 % [22].

Within the complete processing sequence of CIGS based solar cells, an important prerequisite for the achievement of such high efficiencies is the utilization of a well

engineered buffer layer between the CIGS compound semiconductor and the front electrode. Most commonly this buffer layer is represented by a thin CdS film, deposited during a wet chemical process step. However, as it is not desirable to use toxic heavy metals in an environmentally friendly product, a substantial research effort has been conducted to replace this layer with less problematic materials [23, 24]. Beyond these general product considerations, there are several more aspects driving the search for alternative buffer layer materials: In the first place, the wet chemical process itself is not very attractive for an implementation into a large scale production environment, since it creates liquid toxic waste [25], which has to be disposed with substantial effort. Therefore, this process is connected to significant operational costs. Another disadvantage of implementing a wet chemical CdS process into a production line is its low productivity, resulting in a large number of deposition tools. Conclusively, an upscaling of the production capacity would require an enormous demand in space and financial investment. Since the PV market has become highly competitive, it is essential for every manufacturing company to reduce these costs and to optimize their operational expenses. At the same time this has to be done together with a continuous improvement of the conversion efficiencies to furthermore decrease the ratio of production cost per W_p of the respective solar modules in order to survive the “shake out” of the market environment.

A promising approach to reduce both the capital and operational expenditure and to replace the CdS wet chemical process is the introduction of the vacuum based evaporation of In_2S_3. However, as it has already been found by different groups, the replacement of the CdS buffer layer without a loss in conversion efficiency is a quite challenging task [23]. In this context, it is of essential meaning to understand the crucial demands on the buffer layer and to adjust the characteristics of the alternative layer to meet these requirements. The goal of this thesis is to take over this issue and to conduct a detailed analysis of the indium sulphide buffer layers and its characteristics, having an influence on the electrical properties of the respective solar cells and modules. Moreover, the origin of observed deficiencies in the conversion efficiencies compared to CdS buffer layers shall be determined. Based on these findings, an approach will be developed to close the efficiency gap and to outline possibilities to further enhance the potential of Cd-free CIGS solar modules.

Within this scope, the second chapter gives an insight in the CIGS technology and engages with the demands on the buffer layer and potential other candidates to replace the CdS layer. With respect to the utilization of In_2S_3 as an alternative, a literature review provides a detailed description of the In_2S_3 bulk and thin film characteristics found by other

research groups. Chapter three will give an overview of the crucial characterization methods for the properties of individual thin films and complete solar cells. As an introduction to the experimental results, chapter four engages with the prerequisites on the In_2S_3 source material and describes both, process and equipment utilized for the deposition of the buffer layers. The experimental results in chapter five include a variety of structural, chemical and optical characteristics found for the buffer layers as a function of their composition, i. e. the S/In ratio. At this point, the dependencies of the electrical properties of solar cells are discussed in detail, while the observed differences are associated with the changes in the characteristics of the buffer and its interaction with the absorber layer. Moreover, a model is presented, describing the influence of the buffer layer's properties on the band alignment at the absorber-buffer-interface. Chapter six outlines an approach for the optimization of the indium sulphide buffer layer towards higher conversion efficiencies by a doping process. The found characteristics of the altered films will be discussed and associated to the electrical properties of solar modules equipped with such buffer layers. Based on the model introduced in chapter five, the findings will be discussed and integrated, respectively. Finalizing the thesis, chapter seven summarizes the results and gives an outlook for further optimization possibilities.

2 Background

2.1 Solar modules based on the CIGSSe technology

As already mentioned, solar cells based on CIGS and related technologies show one of the highest potentials for conversion efficiencies beyond other thin film technologies throughout the literature [26, 27]. However, in order to achieve such high efficiencies, every process step has to be performed as part of an optimized sequence. This starts with a deposition of a thin Si_xN_y layer on a float glass, acting as a barrier against diffusion of undesired elements from the glass into the solar cell thin film stack [19]. The role of the back contact is taken over by a Mo film, which is sputtered onto the barrier layer during the following process step. The metal based constituents of the absorber layer are also sputtered together with a Na containing compound on top of the back contact. Subsequently to the PVD deposition of Se onto the precursor stack, the formation of the semiconducting absorber is done inside a sulphur containing environment at elevated temperatures. In the base case, the resulting *p*-type CIGSSe-absorber layer is coated with an *n*-conducting CdS buffer layer by chemical bath deposition (CBD) based on the decomposition of thiourea. Afterwards, a thin intrinsic ZnO (*i*ZnO) layer and an *n*-type ZnO:Al (*n*ZnO) front electrode is deposited onto the CdS layer [19].

The processing of the CIGSSe absorber itself leads to the formation of different profiles in the elemental distribution of the constituents. Two of the most important ones are an increasing Ga gradient towards the Mo back contact and an also increasing S gradient towards the absorber surface [19]. Both profiles are known to cause an increasing band gap gradient towards higher contents. The Ga gradient at the back contact acts as a back surface field, whilst the S gradient at the absorber surface leads to a higher band gap within the space charge region. Both effects cause an increase in open circuit voltage (V_{oc}). Moreover, sulphur is able to passivate defects, which can also result in an increase in V_{oc} and fill factor (*FF*). Hence, these two gradients have a significant influence for an enhancement of the efficiency potential of the resulting solar cells [19, 28].

The typical *n*-type CdS buffer layer inside the CIGSSe solar cell is deposited to accomplish several functions. In the first place, it is meant to form the *pn*-junction together with the *p*-type absorber [29]. Since the widths of the band gaps of the absorber and both ZnO layers differ substantially from each other, the buffer also takes over the role to accommodate the alignment of the valence- and conduction bands between the absorber

and the front electrode. A lack of band alignment in the conduction band would lead to large band offsets, deteriorating the electrical properties of the solar cells [30]. Since the absorber surface is very sensitive to sputter damage, the buffer layer also protects it during the magnetron sputtering processes of the *i*ZnO and *n*ZnO layers [23].

The *i*ZnO layer is also addressed as second buffer layer. This happens due to the fact that it hampers lateral current flows in the direction of electronically unbeneficial areas on the CdS surface [23]. For example these areas might occur at incomplete coverage of the absorber surface caused by its rough topology. Due to its high resistivity, this layer has to be sputtered by an RF process. The technology has the advantage, that the kinetic energy of the incident ions is significantly reduced when compared to the DC technology. Therefore, the *i*ZnO layer also serves as an additional protection of the absorber-buffer stack [23].

The *n*ZnO film represents the transparent front electrode where the respective majority carriers are withdrawn. This layer features both high conductivity and high transparency to avoid an increase in series resistance but also allowing photons to pass through to the absorber layer [23].

A further big advantage of thin film solar cells is the ability to achieve an integrated series connection of single cells. This is beneficial since it is not necessary to interconnect several diodes via contact leads to attain a complete module. A cross section of the described stack within a complete module is shown in Fig. 2.

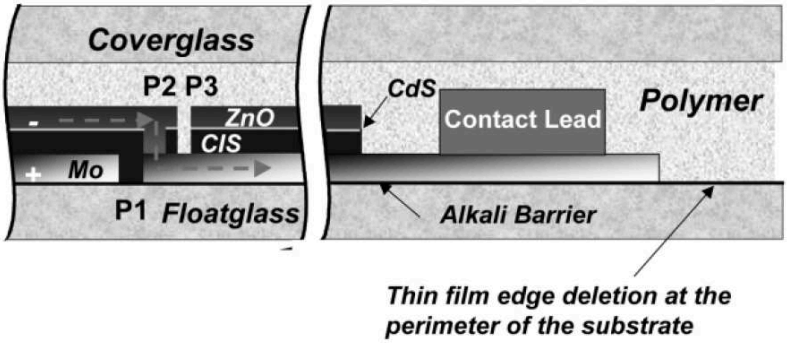

Fig. 2: Schematic cross section of the interconnected thin film solar cells inside an encapsulated module (from [19]).

The features marked with P1, P2 and P3 in Fig. 2 are the patterning lines, allowing the above mentioned serial connection of diodes within the module. Their scribing is partly done by laser ablation and partly mechanically [19]. The generated current is withdrawn via the contact leads located at opposite sides of the serial connection. The so called circuit is laminated with a polymer foil such as polyvinyl butyral and an additional front glass to protect the cells and the contact leads from environmental influences [19]. Typical sizes

within the production line are 1595 x 684 mm². However, since this size is far too large for the development of new processes, research is conducted on either single solar cells without patterning lines, featuring an aperture area of 1.34 cm², or on the basis of 10 x 10 cm² modules.

2.2 The buffer layer

2.2.1 Demands on the buffer layer

It is commonly known that the deployment of a buffer layer between the absorber and the front electrode is essential for the achievement of high conversion efficiencies in CIGSSe solar cells [31]. The buffer has to accomplish several demands in order to fulfil this effect. As mentioned above, it should be *n*-type conducting since it is meant to form one side of the *pn*-junction. Furthermore, it should be highly resistive to prevent a possible shunting through the junction [30]. Looking at this prerequisite one can already conclude that a complete coverage of the absorber's surface is also required. Since internal analysis of the used absorbers showed a relatively rough surface (not shown here), featuring a core roughness depth of up to several hundred nanometres, it can be concluded that a certain minimum thickness of the buffer layer is required to fulfil this task.

With respect to the lattices of both layers, it is desirable that they are in good accordance [30]. Mismatches at this point could result in structural defects, leading to recombination of electron-hole-pairs in the junction. Furthermore, the band gap of the buffer layer should be significantly higher than the one of the absorber. This demand becomes obvious if one considers that photons, absorbed in the buffer region, can no longer create electron-hole-pairs in the absorber, which would lead to a reduction in current density [23]. Following this argumentation, it becomes clear that the transition in the band diagram from the absorber to the front electrode can not happen without discontinuities. The type and the absolute value depend on the relative electron affinities [32]. In this context a positive offset ΔE_c in the conduction band is referred to as "spike", while a negative offset is called "cliff" [33]. Both situations are depicted in Fig. 3.

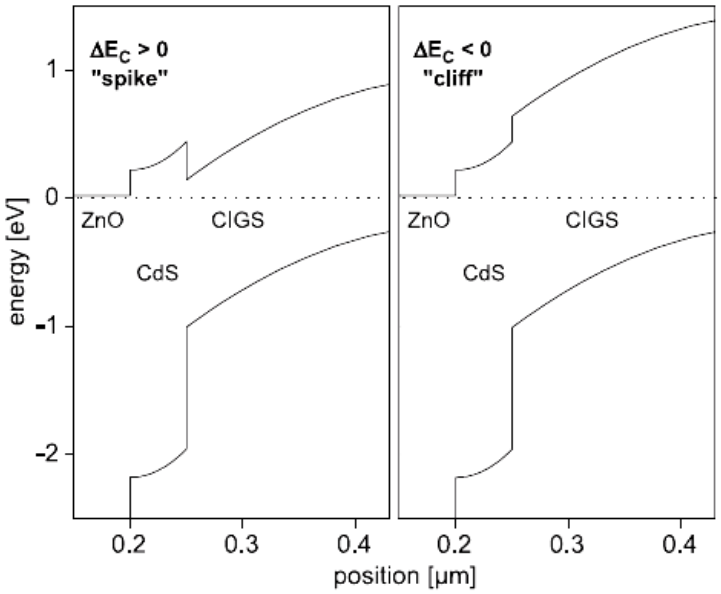

Fig. 3: Schematic view of a possible band diagram in the region around the *pn*-junction of a CIGS solar cell for the case of a positive (left) and a negative (right) conduction band offset (from [33]).

In general, most of the incoming photons are able to pass through the front electrode with a typical band gap of about 3.3 eV [23]. Due to the buffer's smaller band gap of about 2.5 eV in case of CdS [23], part of the photons with higher energies are absorbed before they can excite electrons from the absorber's valence band into the conduction band. Hence, a large band gap is favourable for the buffer layer. However, larger band gaps also lead to higher spikes that hamper the electron transport to the front electrode. Nevertheless, it has been found that a small positive offset of about 0.2 – 0.4 eV in the conduction band does not deteriorate the transition of charge carriers [34, 35]. In contrary, a cliff of about 0.1 eV – 0.3 eV is already able to do so. This can be understood with the accompanied inversion of the absorber's surface in connection with the appearance of a positive conduction band offset [34-36]. Since the buffer layer features an *n*-type conductivity, the Fermi level is close to the conduction band. This means that the electrons at the absorber-buffer-interface are in fact majority carriers and the amount of holes, available for recombination, is reduced. Hence, the *pn*-junction, where the amount of electrons equals the amount of holes, is driven underneath the surface of the absorber and away from the vast amount of defects due to the absorber's exposure to air after the fabrication. In case of a negative conduction band offset the type inversion is lost and the *pn*-junction is close to the interface defects between the absorber and the buffer, resulting in an enhanced recombination [34, 36]. Conclusively, the choice of the buffer layer material and a well designed interface play a crucial role for the utilisation of the efficiency potential of CIGSSe solar cells.

2.2.2 Alternative material systems to CdS

Throughout the literature many different material systems like In_2S_3, In_2Se_3, In(S,OH), ZnS, Zn(S,OH), ZnO, $InZnSe_x$, ZnSe, $Zn_{1-x}Mg_xO$, SnO_2, and SnS_2 have been discussed for the replacement of CdS as buffer layer and also gained remarkable results with efficiencies of up to 18.6 % [37]. However, within the scope of recent studies it became clear that In_2S_3, ZnS and $Zn_{1-x}Mg_xO$ with their derivatives possess the highest potential for an application within a large scale production line [23]. For the deposition of these compounds CBD, atomic layer deposition (ALD), ion-layer gas reaction (ILGAR), physical vapour deposition (PVD) and ultrasonic spray pyrolysis (USP) have been claimed to feature the attributes needed for an industrial use. However, some of these techniques still inherit the already discussed waste issue, like CBD does, or still require some process development regarding their scalability to production size, high throughput, and productivity, like for ILGAR or ALD. The non-vacuum process USP showed the drawback of a relatively low conversion efficiency [23].

Within the scope of the research done at AVANCIS, several different buffer layers have also been tested. This has been done either within the pilotline of AVANCIS or in cooperation with other laboratories [38, 39]. It has been demonstrated that In_2S_3 is the most promising candidate as an alternative to CdS and has hence been investigated more intensively. In the first place this is due to the reason that the utilization of this material system in combination with the CIGSSe absorber led to relatively high conversion efficiencies within several experiments. Furthermore, the process stability and the scalability to high throughputs have been shown to fulfil the requirements for the implementation into a production line. For this reason, the present thesis point's the focus on the use of In_2S_3 as buffer layer for CIGSSe solar cells.

2.3 Indium sulphide and its properties

The properties of In_xS_y have already been investigated and discussed very well in the literature. To outline the relevant aspects for this thesis, the following chapter will review these properties, starting with the crystal structure of the bulk material. Subsequently, the characteristics of the respective thin films will be discussed and an overview will be given on the effects resulting out of the addition of certain third elements into In_xS_y.

2.3.1 Crystal structure of In-S-phases

Starting from the crystal structures that can persist at standard conditions, Duffin et al. [40] found that there are only three In-S-phases to be able to do so. Together with their lattice structures these are:

- In_2S_3 (tetragonal / cubic)
- In_6S_7 (monoclinic)
- InS (orthorhombic)

In its nominal composition and at standard conditions, In_2S_3 is referred as β-phase and crystallizes in the tetragonal structure [41]. This phase is the most mentioned one in the literature and persists from room temperature up to about 420 °C [42, 43]. The structure can be described as defect spinel type. The difference to the regular spinel type is based on the fact that one third of the tetrahedral sites are not occupied, which leads to the quasi quaternary compound formula of $(In_2)_{Oh}(In_{2/3}\square_{1/3})_{Td}S_4$, where $\square$ represents the unoccupied vacancies and Td and Oh indicate the tetrahedral and octahedral sites [44]. The vacancies are ordered on a 4_1 screw parallel to the c-axis of the lattice. The space group has been determined as $I4_1/amd$ by King et al. [41].

At a temperature of 420 °C, the tetragonal structure transforms into a cubic one, which is called the α-phase [43, 45]. Beyond this point the vacancies are no longer ordered but are statistically distributed across the tetrahedral sites. The space group for this phase is $Fd\bar{3}m$ [45, 46]. Since the β-phase is capable to incorporate an excess amount of In, the order of the tetrahedral vacancies is disturbed towards increasing In-contents. Beyond a limit of 40.1 at% [45], respectively 40.5 at% [42], the material can no longer crystallize in

the β-phase. This means that In-rich compositions of $In_{2+x}S_3$ can only persist in a cubic structure if the In-content exceeds the critical value.

The lattice changes one more time into a structure called the trigonal γ-phase for temperatures exceeding 755 °C [47]. The respective space group is P3 m1. At this point, all In-atoms are allocated to the octahedral sites and are layered in series of S-In-S-In-S. The γ-phase can be heated up to the melting point of 1090 °C, which can also be seen in the In-S-phase diagram in Fig. 4.

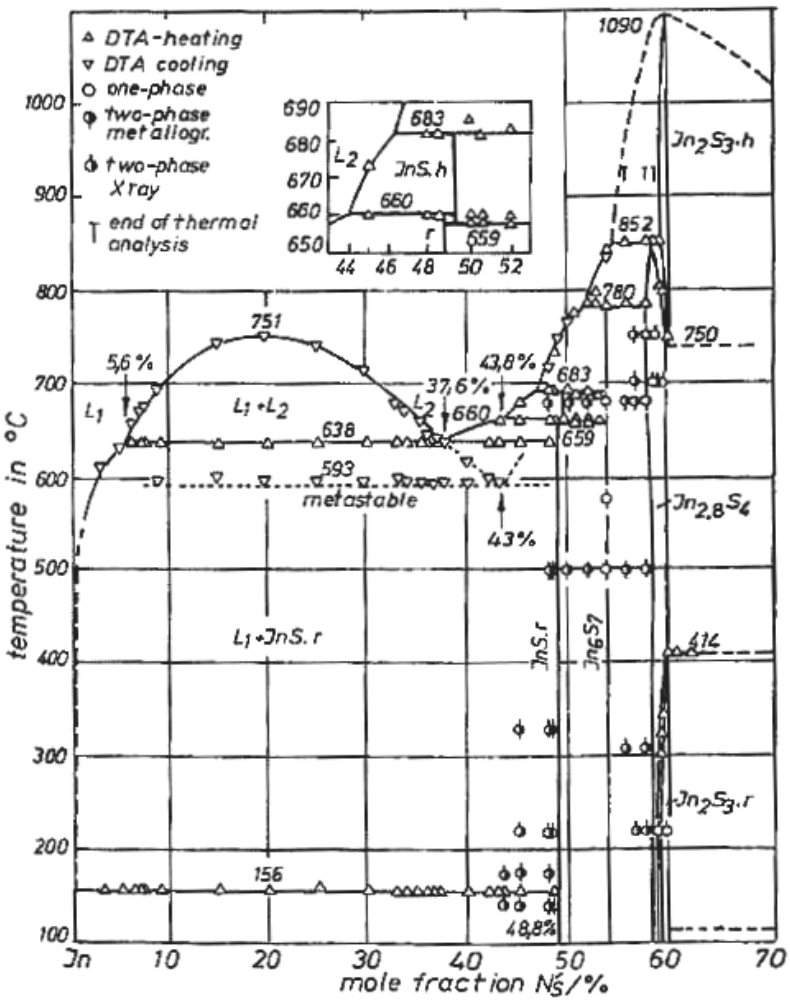

Fig. 4: Phase diagram of the In-S-system including data points (from [42]).

The nomenclature in Fig. 4 differs from the one commonly used in the literature [43]. Consistent to the latter, In_2S_3.r in the phase diagram can be referred to β-In_2S_3, $In_{2.8}S_4$ to α-In_2S_3, and In_2S_3.h to γ-In_2S_3.

At low temperatures, starting from stoichiometric In_2S_3 proceeding towards higher contents of In, one reaches a region in the phase diagram where a coexistence of In_6S_7 and α-In_2S_3 persists. In_6S_7 itself crystallizes monoclinic in the space group $P2_1/m$ [48]. The

complete structure features two separate areas in which the S atoms are positioned in nearly cubic close-packed arrays; whereby the In atoms are in octahedral coordination.

The InS phase crystallizes in an orthorhombic structure in the space group *Pnnm* [49]. In this configuration two In atoms are bound to each other while both of them are connected to three further S atoms. The three dimensional network is then built while three S_3In-InS_3 groups share their S atoms [50].

Table 1 summarizes the above mentioned In-S-phases with their respective structure, their lattice parameters and their space groups. Since the γ-phase is not stable at room temperature, the given lattice parameters are stated as the ones obtained with the help of elemental substitution by As and Sb.

Table 1: Phases in the In-S system with their respective structure, lattice parameters and their space groups (data taken from [41, 45-49]).

Phase	**α-In_2S_3**	**β-In_2S_3**	**γ-In_2S_3**	**In_6S_7**	**InS**
Structure	cubic	tetragonal	trigonal	monoclinic	orthorhombic
Lattice parameters	a=10.72 Å	a=7.61 Å; c=32.24 Å	As: a=3.806 Å; c=9.044 Å; Sb: a=3.831 Å; c=9.049 Å;	a=9.090 Å; b=3.887 Å; c=17.705 Å; β=108.20°	a=4.4493 Å; b=10.6493 Å; c=3.9459 Å
Space group	*Fd3̄ m*	*I41/amd*	*P3̄ m1*	*P21/m*	*Pnnm*

2.3.2 Properties of In_xS_y buffer layers

Regarding the vast possibilities to deposit In_xS_y buffer layers, it is not surprising that the reported characteristics of the thin films vary for the different approaches. Depending on the technique and on the precursor materials, the processes cause different types and amounts of impurities, that can significantly change the thin film properties [44]. Yoshida et al. [23] claimed that their films basically show an excess amount of sulphur compared to In_2S_3 but are free of significant amounts of oxygen, what is usually seen in films deposited by CBD. With respect to composition and morphology, they measured a variation in the S/In ratio and grain size. Besides a potential structural change from β-In_2S_3 to α-In_2S_3, both variations have been assumed to be responsible for a broad shift in the band gap from 2.3 eV to 2.7 eV determined via absorption measurements and calculated for a direct transition. The impact of the grain size has been attributed to quantization effects since they were assumed to be smaller than 10 nm [51]. Barreau et al. [52] have challenged this

assumption while measuring an even higher band gap of 3.7 eV for a CBD process by UV/VIS spectroscopy. In contrast to the films of Yoshida et al. [51] these films were characterised as In-rich but also varied in their S/In ratio in dependence of the bath's pH value. With a determination of the band structure and its evolution they concluded that the band gap widening lies in contradiction to the assumption obtained out of quantization effects but can be associated to the formation of an alloy between $In(OH)_3$ and In_2S_3 [52].

Sterner et al. [29] reported an indirect band gap of 2.1 eV for films that have been deposited by ALD, while a direct band gap of about 2.7 eV has been reported by Naghavi et al. [53] for the same deposition technique. In both cases the band gaps have been ascertained via optical measurements. Also in these publications a possible band gap widening due to the implementation of impurities like oxygen originating from precursor materials have been discussed.

The band gaps with the closest values to the one of the single crystal of about 2.0 eV with a direct transition [54] is reported for In_2S_3 films deposited by PVD. For co-evaporation of In and S Barreau et al. [55] reported an indirect band gap of 2.0 eV, what has been confirmed by Pistor et al. [43] for compound evaporation of In_2S_3. Herrero et al. [56] reported a direct band gap of also 2.0 eV for thin films that have been processed via a chalcogenization of electroplated In-films. According to Barreau et al. [44] the high degree of compliance happens due to the assumption that these films can be grown with least contamination of other elements. Besides these values, Verma [57] found a direct band gap of 2.5 eV for thermally evaporated compound In_2S_3. However, in this context it has also been stated that the source material contained In_2O_3, which might be the reason for this value. Referring to the properties of the more In-rich phases, In_6S_7 single crystals have been found to obtain a band gap in the range of 0.6 eV [58] to 0.9 eV [59]. Furthermore, a band gap of 1.9 eV has been stated for InS [50, 60].

Throughout the literature, both In_2S_3 films [56, 61] and single crystals [54], are reported to be *n*-conductive. For the latter case it has been observed that the *n*-type character is improved when the compound is sulphur deficient. The carrier densities were found to vary in the range of 10^{13} cm^{-3} for stoichiometric β-In_2S_3 and up to 10^{18} cm^{-3} for sulphur deficient β-In_2S_3. Respective carrier densities in thin films have been reported to be in a range of 10^{16} cm^{-3} – 10^{17} cm^{-3} for ALD depositions [53]. The In_6S_7 phase has partly been described to feature *p*-type conductivity with a hole density of $7.4*10^{13}$ cm^{-3} [62], while other researchers determined the phase to be of *n*-character with an electron density of $1.2*10^{13}$ cm^{-3} [63] and $4.7*10^{8}$ cm^{-3} [58], depending on the single crystal growth

conditions and parameters. In both cases, a strong compensation and a contribution of both holes and electrons to the total conductivity has been concluded. For InS single crystals, an *n*-type conductivity with an electron density of $4.7*10^{14}$ cm^{-3} has been determined by Quasrawi et al. [64] and about 10^{18} cm^{-3} by Nishino et al. [50]. The origin of this difference might also be related to different growth conditions, as it has been assumed by Quasrawi et al. [63] in the case of In_6S_7. For measurements on InS thin films Seyam [60] determined an *n*-type conductivity with a charge carrier density of about 10^{15} cm^{-3}.

The electrical conductivity has been found to vary in a relatively broad range. Within sulfurization experiments of heated indium layers, the conductivity decreased from 10^{-2} S/cm to 10^{-6} S/cm for increasing sulfurization temperatures from 300 °C to 600 °C [61]. The lowest conductivity was found to be in the range of 10^{-7} S/cm under light exposure for films deposited by atomic layer epitaxy [65]. For a measurement in dark this value has been mentioned to be even lower. Referring to the observation of photoconductivity of In_xS_y layers, Jayakrishnan et al. [66] determined a dependency on the S/In ratio of the respective films, deposited by chemical spray pyrolysis. This effect has been associated to variations in the defect chemistry at the film's grain boundaries. Yoosuf et al. [61] also investigated the effect of light induced changes in the electrical properties of In_2S_3 films prepared by reactive sulfurization of evaporated indium. As a result of their evaluations, an increasing photoconductivity towards higher sulfurization temperatures has been associated to an improvement in crystallinity. Assuming an enrichment of impurities at the grain boundaries with increasing temperatures, this observation might be in agreement with the results of Jayakrishnan et al. [66].

2.3.3 Effects of foreign elements in indium sulphide buffer layers

As discussed in the previous chapter, the characteristic properties of In_xS_y thin films strongly depend on the way how they were deposited and with this also on the type and amount of impurities. With respect to certain aspects of In_xS_y buffer layers, some of these variations might become useful since the inherently negative aspect of a relatively small band gap can be compensated by the systematic implementation of specific elements. One could think of the possibility to use the effect of band gap widening to adjust the band offsets at the absorber-buffer-interface to an optimal value or to simply reduce the loss in current density in the region of higher photon energies. Several research groups already

worked on these aspects [52, 67, 68] and determined in which way the characteristics of In_xS_y are influenced by impurities.

Barreau et al. [69] deposited compounds consisting of In, S and O at elevated temperatures and found that the oxygen leads to a substitution of sulphur atoms in the In_2S_3 matrix. During this study it has been observed that the band gap widens linearly from 2.1 eV to 2.9 eV with increasing oxygen contents to about 8.5 at%. Within this variation the films stayed *n*-type and the conductivity increased by two orders of magnitude.

From other studies it is known that both Cu and Na are able to diffuse from the absorber into the In_2S_3 layer depending on the process parameters [70, 71]. Hence, the knowledge upon the changes in the characteristics of the buffer layer is of major importance to understand why and how the electronic properties of solar cells are changing. To study this topic, Barreau et al. [72] deposited several thin layers of In, S and NaF on sodium free glass and annealed the stacks at 400 °C. He found that the introduction of Na into the In_2S_3 lattice has an upper limit of 5.0 at% for thin films. The amount of Na exceeding this value has been found to segregate at the surface upon the annealing step. Within the range of 0 – 5.0 at% they found a band gap widening from 2.1 eV to nearly 3.0 eV, as determined via transmission and reflection measurements. Starting from pure In_2S_3, the conductivity has been reported to increase from about $2.0*10^{-8}$ S/cm to $5*10^{-7}$ S/cm when about 0.2 at% Na is introduced into the films. At higher Na-contents of up to 5.0 at%, the conductivity continuously decreases to about $1*10^{-7}$ S/cm. For further increases in the Na-content above 5.0 at% no further increase in the band gap has been found anymore. Albeit the conductivity has been found to further increase, this effect has been attributed to a superficial effect since the Na segregates at the surface. The structure has been proposed to be $(In_{16})_{Oh}(In_{5.33-x}Na_{3x}\square_{2.66-2x})_{Td}S_{32}$ with x varying in the range from x=0 to x=0.9, where Oh represents an octahedral and Td a tetrahedral site. The $\square$ represents a vacancy. In a different experiment [72, 73], $NaIn_5S_8$ has been synthesized from In_2S_3 and Na_2S in a silica tube at 800 °C. The discrepancy in the Na-content of 7.1 at% to the stated maximum for thin films (5.0 at%), has been explained by the different annealing temperatures and/or the sulphur overpressure inside the silica tube.

In contrast to the incorporation of Na, it has been found that the introduction of Cu leads to a reduction of the band gap to a value of 1.5 eV at the point when the amount of Cu has reached a value as high as required for the phase of $CuIn_5S_8$ [74]. For 600 nm thick films the conductivity has been reported to significantly decrease from 10^{-2} S/cm to 10^{-6} S/cm for a variation of the Cu content in the respective range. Furthermore, it has been

reported that the implementation of Cu leads to a reduction of the *n*-type character of the In_xS_y layers [44].

Another very important aspect, that has been considered within a further study [75], is that the diffusion of Na and Cu into the In_xS_y buffer might happen at the same time, as it has also been found by Bär et al. [70]. This could occur either during the deposition or a latter process step. Especially during the *n*ZnO process this could be the case, since it is conducted at elevated substrate temperatures. For this experiment, several tablets have been pressed out of grounded Na_2S, Cu_2S and In_2S_3 in different compositions within the range from $CuIn_5S_8$ to $NaIn_5S_8$. After an annealing step for 7 days at 850 °C, X-ray diffraction measurements confirmed the existence of the phases MIn_5S_8 (M=Na, Cu) and allowed the conclusion of a complete solid solubility in the tested range with the formula $Na_xCu_{1-x}In_5S_8$ ($0 \leq x \leq 1$). Furthermore, it has been shown from optical measurements that the band gap linearly increases towards higher sodium contents. However, pure $NaIn_5S_8$ showed a larger band gap than expected from the linear evolution, indicating a difference in the impact between Na and Cu on the characteristics of the particular solid solution [75]. Referring to the above mentioned demand on large band gaps for the buffer layer, the need to prevent a Cu diffusion into the In_xS_y film becomes obvious. This can be achieved by an enrichment of the absorber surface with Na, since the first diffusion reaction to occur is suppressing the diffusion of the other, i. e. the one of Cu [75]. From the view of the band structure, Lafond et al. [68] have found that it is not only the width of the band gap that changes, but also the nature of the transition. Pure $NaIn_5S_8$ has been determined to feature a direct transition, while $CuIn_5S_8$ and a solid solution with x=0.5 show an indirect one. Besides the changes in the band gaps, all compounds have been reported to remain *n*-type [44]. However, it has also been stated that the introduction of Na leads to a slight enhancement of the *n*-type character, while Cu significantly reduces it.

The observation of a deterioration of the electrical properties of solar cells when Cu is present inside an In_xS_y buffer layer has been confirmed by Abou-Ras et al. [76]. For sputtered In_xS_y layers at a substrate temperature of 340 °C a $CuIn_5S_8$ phase has been found to have formed at the absorber-buffer-interface. Besides a possible additional negative influence of Ga, also being present inside the buffer due to diffusion from the absorber, this phase has been assumed to be responsible for a strong decay in conversion efficiency.

In contrast to the above mentioned studies [75, 76] and the conclusion that a diffusion of Cu into an In_xS_y buffer layer should be avoided to achieve high conversion efficiencies, Pistor [43] reported a beneficial effect of this incidence under utilization of

sulphur free absorbers. Starting from solar cells with In_xS_y buffer layers from compound evaporation with poor efficiencies, the author found that the efficiencies significantly increased after the cells have been annealed at 200 °C for 30 min. This has been attributed to a Cu enrichment in the buffer layer and a depletion of the interface near region of the absorber. The extent of the Cu enrichment in the buffer reached about the composition of $CuIn_5S_8$. It has been concluded that the Cu-depletion of the absorber's surface increased the distance of the Fermi level to the valence band, leading to a significant reduction of tunnelling recombination at the absorber-buffer-interface [43].

Looking at this broad spectrum of characteristic values for different In_xS_y buffer layers, it can be concluded that it is essential to be aware that changes in the deposition method, process control or source material can lead to significant variations in the obtained film characteristics and hence in the electrical properties and performance of the resulting solar cells. Furthermore, this emphasizes that the produced films have to be characterized individually to gain reliable results for relevant values like the band gap.

3 Characterization methods

3.1 Current-voltage-characteristics of solar cells

The most common approach to characterize a solar cells is to record the current density j in dependence on the applied voltage V [77]. It is relatively easy to determine values like the open circuit voltage V_{oc} or the short circuit current density j_{sc} from this curve, as these are the intercepts with the axes of the jV characteristic of the illuminated solar cell. By plotting the power density, which is the product of both parameters, versus the applied voltage one can find the so called maximum power point (MPP) from the minimum of the respective graph. To outline this relationship Fig. 5 shows the diode characteristic of an illuminated 10x10 cm² CIGSSe module with the respective power output.

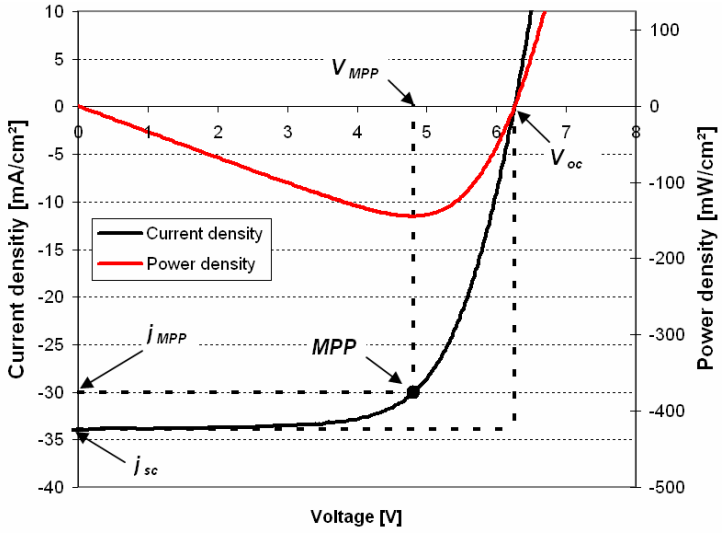

Fig. 5: Diode characteristic of an illuminated CIGSSe 10x10 cm² module together with the respective power density in dependence of the applied voltage (after [77]).

As it can be concluded from the given denotation of the MPP, an operation of the module at a working resistance, given by the values of V_{MPP} and j_{MPP}, leads to the highest power output. With the help of the MPP and the product of V_{oc} and j_{sc} one can furthermore calculate the fill factor FF of the diode characteristic. Multiplying the latter three main parameters of the solar cell and calculating the quotient with the power of the incident light onto the solar cell gives the conversion efficiency η [78]

$$\eta = \frac{V_{oc} \cdot FF \cdot j_{sc}}{p_{in}}, \tag{3.1}$$

where p_{in} is the power density of the incident light.

Since the above described parameters are not sufficient to fully evaluate the properties of a solar cell, further information on the diode characteristic is required. It is necessary to be able to describe the curve by a model and to mathematically fit it to the measured data. Usually, such models are based on either one or two diodes with a shunt resistance R_{sh} connected in parallel and a series resistance R_s describing the behaviour of the solar cell [9]. The respective equivalent network of a single diode model is depicted in Fig. 6.

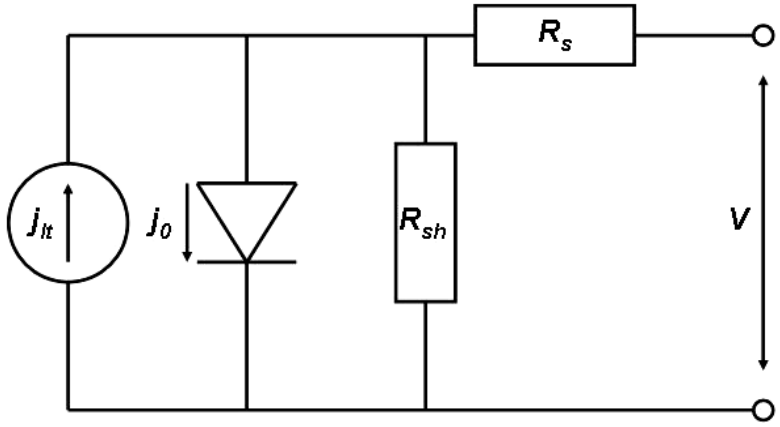

Fig. 6: Equivalent network of a single diode model in order to describe the electrical properties of a solar cell (after [9]).

In this context the shunt resistance is used to describe current paths parallel to the *pn*-junction. For example this can be caused by so called pinholes or scratches in the absorber layer, where the front and the back electrode are in ohmic contact with each other. The resistance of the solar cells front electrode or the contact leads are modelled by the series resistance. For a better comparability, both the shunt and the series resistance are normalized to the solar cell's area. Consequently, with the equivalent network the mathematical model can be written as [79]

$$j(V) = \frac{V - R_s j(V)}{R_{sh}} + j_0 \cdot \left(e^{\frac{q(V - R_s j(V))}{n k_B T}} - 1 \right) - j_{lt}, \tag{3.2}$$

where j_0 is the dark saturation current density, q the elementary charge, n the ideality factor, k_B the Boltzmann constant, T the absolute temperature and j_{lt} the light generated current density.

The straight forward way to fit this model to the measured data is the least square method [79]. However, using this approach often leads to unsatisfactory results with respect to the fit quality of the *jV*-curve around the MPP. Furthermore, noise in the applied bias has a significant effect on the noise of the current density, caused by the steep slope of the curve in the high voltage region. For this reason Burgers et al. [79] have developed the orthogonal distance regression (ODR). This method allows considering both the noise in voltage and current density and also the determination of uncertainties in the computed parameters. Doing so, the ODR assumes that voltage and current noise are independent from each other and minimizes a sum of squares of distances to the measured data pairs of the noise scaled, fitted *jV*-curve. A more detailed description of this method can be found in [79].

This evaluation technique does find its application for both, single solar cells and 10x10 cm² modules. For characterizations on single solar cells, however, it has been found that the fit result for the series resistance does adapt values close to zero ($<10^{-5}$ Ohm*cm²). This observation might be explainable by the fact that the series resistance of single solar cells are simply too small to be evaluable by the fit procedure. For the case of the evaluation of 10x10 cm² modules, the fit procedure does return reasonable values. Nevertheless, since all fits of the series resistance of single solar cells resulted in values close to zero, the uncertainty in the fit procedure is assumed to be comparable for all measurements. To be able to exploit the dependency of the series resistance anyway, an additional method has been implemented into the automated evaluation of the *jV*-characteristics. This method calculates a linear regression line based on several data points around the open circuit voltage of the illuminated diode characteristic. Out of the inverse of the respective gradient of the regression line, the series resistance can be calculated [80]. To outline the origin of this value, it is referred to as $R_s(oc)$, where *oc* stands for open circuit.

The solar cells, 10x10 cm² circuits and modules prepared within this thesis were characterized with a Wacom class A sun simulator WXS-140S-Super. In the beginning of every measurement series, the intensity of the sun simulator was adjusted so that a current density of an externally certified module reaches the corresponding value for an AM1.5 measurement at 1000 W/m². The setup was equipped with a cooling chuck to ensure a characterization under standard conditions. To be able to consider possible light induced changes in the electrical properties of the solar cells and modules, the samples were exposed to the simulated AM1.5 spectrum for two minutes prior to the characterization.

The measurements were done via a four terminal sensing to avoid a falsification of the determined characteristics by contact resistances.

3.2 External quantum efficiency

Besides the *jV*-characteristic, another important measure is the information on the magnitude of which wavelength region contributes to which extent to the total current density, delivered by a solar cell. According to the Shockley-Queisser limit [81], every photon with an energy larger than the band gap of the absorber can create an electron hole pair and can be collected at the contacts of the solar cell. However, for real solar cells this is not the case, since optical and recombination losses cannot be avoided completely. Gaining knowledge about these loss mechanisms can enhance the understanding of the processes taking place inside the solar cell and lead to ideas for optimization. A technique to characterize solar cells in this respective way is the external quantum efficiency (EQE) Q_e. It is defined as the number of electrons collected per incident photon given by [82]

$$Q_e = \frac{1}{q} \cdot \frac{dj_{sc}(E)}{d\Phi(E)}, \tag{3.3}$$

where q is the elementary charge and $d\Phi(E)$ the incident photon flux in the energy interval dE, leading to the short circuit current density $dj_{sc}(E)$.

To irradiate the solar cells with monochromatic light, two different principles are commonly used. These are either based on the utilization of a monochromator or a filter wheel. A setup using a monochromator has the advantage of a high wavelength resolution, but a drawback concerning the size of the measurement spot. Usually this lies in the range of only a few millimetres. In contrary, a filter wheel based setup can achieve a measurement spot size of several centimetres and can hence illuminate complete cells. Due to a limited number of filters, this method carries the disadvantage of a lower wavelength resolution. Since the measured signals are relatively small, the characterization is usually done with chopped light and a lock-in-amplifier [82].

All measurements performed for this work have been conducted in close cooperation with the Friedrich-Schiller-University of Jena. The respective setup included a high pressure xenon lamp as light source and an Oriel Instruments chopper wheel 75160, modulating the light with a frequency of 137 Hz. The utilization of an Oriel Cornerstone 130 double monochromator, allows a wavelength resolution of 1 nm. During the irradiation

of the solar cell, the generated current was converted into a voltage via a transimpedance amplifier 13AMP003 from the company Melles Griot, while a lock-in-amplifier 7265 of the company Signal Recovery allowed the evaluation of the respective data. To avoid a falsification of the measurement due to light induced changes in the conductivity of parts of the solar cell, the characterization was done under bias light with an intensity of 11 % of the AM1.5 spectrum.

3.3 X-ray fluorescence spectroscopy

An important analysis method to characterise thin films is X-ray fluorescence spectroscopy (XRF), which is able to grant access to the elemental composition of the investigated probe [83]. The physical effect used for this technique is based on the ability of high energetic photons to excite electrons from inner shells of atoms to a higher level. Once the created vacancy is filled up by an electron originating from a higher energy state, a characteristic photon is emitted whose energy equals the difference between the energy states before and after the transition. The transition energy from one shell to another is a characteristic value for a specific element. The appearance of the combination of several characteristic peaks in an XRF spectrum enables the determination of the elements at hand. The schematic view of a K_α transition, where a photon with the energy $\hbar\omega_1$ lifts an electron out of the K shell generating a vacancy, is depicted in Fig. 7. The fluorescence signal with the energy $\hbar\omega_2$ originates from the "fall" of one electron from the L down to the K shell.

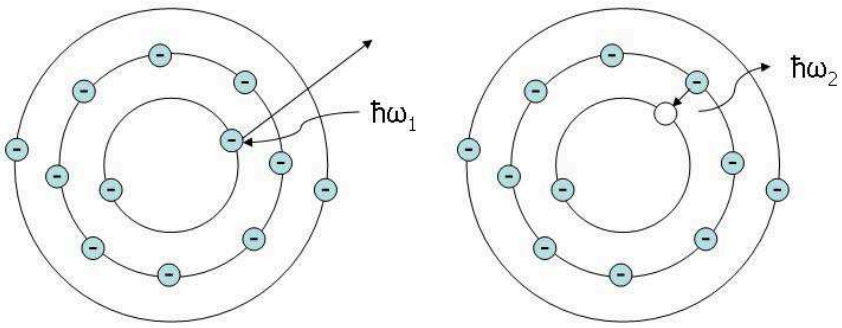

Fig. 7: Schematic view of a K_α transition used for XRF measurments (after [83]).

Regarding the detection of the emitted radiation, one can differentiate between energy dispersive (EDX) and wavelength dispersive (WDX) X-ray spectroscopy [83]. In the case of an energy dispersive detection, the whole spectrum of the emitted radiation is recorded simultaneously. This can be done via an assignment of charge pulses to certain energy slots, which have been generated in a field-effect transistor from the characteristic

radiation. The energy dispersive detection has the advantage of a very fast feedback about the samples composition. However, drawback is the lack of resolution compared to the wavelength dispersive detection. For the latter method, the effect of diffraction of the emitted radiation inside a crystal to certain angles is used. This means that the lattice planes orientation within a crystal is aligned in such a way that a certain wavelength is selected and directed to a detector. By rotating the crystal to different angles, a scan over a complete spectrum can be achieved. Consequently, this means that the wavelength dispersive attributes are the opposite ones of the energy dispersive method, i. e. a high resolution in trade for a longer measurement time. To enhance the advantage of high resolution, specially selected crystals and detectors are utilized for certain spectral ranges [83, 84].

Regarding the thin films analysed for this work, the XRF tool has been calibrated beforehand by composition measurements using Rutherford backscattering (RBS). This technique is a calibration free method to characterize the composition of thin films where α-particles are accelerated towards the film. With a certain probability the α-particle hits the nucleus of an atom in the film and is scattered subsequently. Upon the knowledge of the energy of the incident particles, the amount of lost energy contains information about the type and quantity of elements in the film. A more detailed description of this technology can be found in [85].

For this work, a SRS 3400 and a S8 Tiger from Bruker have been used. Both systems were equipped with a Rhodium anode to generate the X-rays for the wavelength dispersive analyses. For the determination of the In-content of the analysed films, the L_α-line has been used, while the K_α line has been chosen for sulphur and sodium. In the SRS 3400 system a Ge-crystal has been used to diffract the characteristic radiation of the sulphur atoms and a LiF200-crystal for indium. The latter crystal has also been used for indium in the S8 Tiger. Sulphur and sodium were characterized via a XS-Ge-C and a XS-55 crystal. The diffracted photons were detected by a scintillation counter for heavier and a proportional counter for lighter elements.

3.4 Spectroscopic ellipsometry

The optical properties of thin film semiconducting materials are typically characterized via transmission and reflection measurements. The optical band gap can be determined using the so called Tauc plot [86]. This method requires a plotting of the product of $(\alpha h\nu)^p$ vs. $h\nu$, where α is the absorption coefficient and $h\nu$ is the energy of the incident light. The exponent p represents the nature of the band gap and can adapt values of 1/2, 2, 1/3, 2/3. These values indicate an indirect allowed, a direct allowed, an indirect forbidden and a direct forbidden transition, respectively [87]. However, the utilisation of this plot from the transmission and reflection measurements has several downsides with respect to accuracy, repeatability and comparability. In general, the determination of the film's transmission requires the subtraction of the substrate's influence. Hence, it is necessary to characterize the substrate within a separate measurement and to subtract the spectrum from the measured result of the complete sample. However, this approach neglects the influence of the reflection at the film-glass-interface, which results in a measurement error. This can lead to obvious issues like a summation of measured transmission and reflection to values larger than 1 in certain spectral ranges. Regarding the evaluation of the data, the occurrence of interference fringes exacerbates a proper assessment of the measurement. The vast range of different formulas used in the literature [87-89] for the determination of the absorption coefficient additionally aggravates the comparability of the obtained results. Together with the uncertainty of choice of the correct exponent, representing the nature of the gap, the fitting of a straight line to the graph is moreover entailed by the subjectively determined area in which the fit is defined. The summation of these potential sources of errors might also be partly responsible for the wide range of band gaps reported in the literature for In_xS_y buffer layers, which has been discussed in detail in chapter 2.3.2.

A very powerful alternative optical characterisation method is spectroscopic ellipsometry [90]. This method uses polarized light to determine the films attributes. Besides the band gap, this method also grants access to layer properties such as the film thickness and the refractive index including the extinction coefficient. The path of the incident polarized light onto a probe and the indication of the changes in the polarization upon reflection on the sample's surface is shown in Fig. 8.

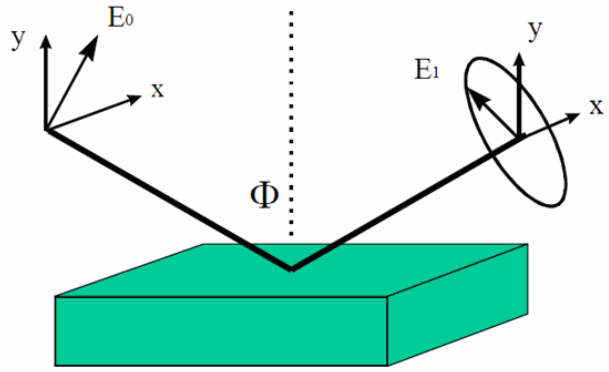

Fig. 8: Sketch of incident, polarized light onto a probe, wherby the polarization of the light changes upon refleciton on the sample's surface (from [91]).

The incident light is linearly polarized under a certain angle (usually about 45°) to the plane of incidence, as indicated by the field vector E_0 in Fig. 8. The field vector E_0 can be split into parallel and perpendicular contributions to the plane of incidence onto the y- and x-axis, respectively. These two contributions feature a certain phase relation to each other. Upon reflection at the sample, both the phase relation and the polarization of the light are altered. As a result, the reflected beam's polarisation becomes elliptic. For the special case of a phase shift of $\lambda/4$ or $\lambda/2$, the polarisation is circular or linear, respectively. The measured parameters by ellipsometry are $\tan(\Psi)$ and $\cos(\Delta)$, where $\tan(\Psi)$ is the amplitude relation of the parallel and perpendicular components of the field vector of the reflected light and $\cos(\Delta)$ is the phase shift between the two components. In this connection, the characteristic information about the films optical properties is described via Fresnel's formulas [90]

$$r_p = \frac{N_s \cos\Phi_i - n_a \cos\Phi_t}{N_s \cos\Phi_i + n_a \cos\Phi_t} \quad \text{and} \tag{3.4}$$

$$r_s = \frac{n_a \cos\Phi_i - N_s \cos\Phi_t}{n_a \cos\Phi_i + N_s \cos\Phi_t}, \tag{3.5}$$

where r_p and r_s are the parallel and perpendicular complex amplitude reflection coefficients. N_s=n_s-ik_s is the complex refractive index of the substrate and n_a the real part of the ambient. Φ_i and Φ_t are the angles of incidence and transmission. With the help of Snell's law [92] Φ_t can be eliminated and the fundamental equation of ellipsometry [90]

$$\frac{r_p}{r_s} = \tan\Psi \cdot e^{i\Delta} \tag{3.6}$$

can be expressed in terms of N_s, n_a and Φ_i. Hence, N_s can be determined with the help of $\tan(\Psi)$ and $\cos(\Delta)$.

This only enables access to the optical characteristics for a reflection at a single interface. However, since the interest of layer properties lies in more complex structures and a certain spectral range, one has to record measurements for different reflection angles and wavelengths and fit a model to the data. For this purpose, several approaches for different material characteristics have already been developed and are usually accessible via already installed features in the tool's software. A variation of the angle of incidence is capable to enhance the amount of available data for the fitting of the used model and to hence increase the reliability of the obtained results [90, 91].

The measurements were performed using a spectroscopic ellipsometer SE850 from SENTECH, which was capable to measure within a spectral range of 280 nm to 2500 nm and for incident angles from 55° to 70°. As a source of light the tool is equipped with a Xe arc lamp for the UV and VIS area until 820 nm and a separate Fourier transform infrared spectrometer system from VARIAN for the NIR region until 2500 nm. Since the characterization of In_xS_y films is only relevant in the UV/VIS area, all measurements were done in the respective area only. Besides a polarizer and a compensator on the emitting side, the SE850 was equipped with a step scan analyzer. This analyzer could be rotated and acquired the data at different angle settings. A subsequent Fourier analysis of the intensities at the different wavelengths resulted in Fourier coefficients that were correlated with Ψ and Δ. This approach granted a high measurement speed and both a high signal to noise ratio and a good accuracy of the obtained data [91].

3.5 Raman spectroscopy

The Raman effect has been experimentally shown by the Indian physicist Chandrasekhara Venkata Raman in the year 1928 and has been rewarded with the Nobel prize in 1930 [93]. This effect describes the way how incident photons are scattered on matter [94, 95]. Basically most of the incoming light onto a sample is either transmitted, reflected or absorbed. However, a small part of photons can also be scattered at the surface. In this case one has to differentiate between elastic and inelastic scattering during which the energetic state of the incident light and the sample is altered. The vast fraction of scattered photons is of elastic nature, meaning that the photons retain their energy and leave the surface without an excitation of the solid state body. This is referred to as Rayleigh

scattering. Besides this, with a probability of 10^{-6} – 10^{-9} compared to elastic scattering, photons can be scattered inelastically, what is referred to as Raman scattering. Here, a photon can either excite a lattice vibration/phonon, leading to a loss in energy (Stokes component) or a lattice vibration/phonon is annihilated and the respective energy is added to the energy of a photon (Anti-Stokes component). The amount of energy added, respectively lost, is symmetric to the wavelength of the incident light and a characteristic value for the analysed material. The scattered light intensity is usually plotted versus the frequency shift relative to the incident light in wavenumbers (reciprocal wavelength in units of cm^{-1}). Usually, only the Stokes component is used for analytical purposes since the shift is identical to the Anti-Stokes component but shows a by far higher intensity due to the low phonon density in the sample at low and moderate temperatures. Depending on properties like the chemical composition, the crystallographic structure or physical stress, the amount, position and shape of the obtained peaks vary for different materials.

To characterize the respective thin films of this work, a Labram system from Horiba was used. Inside the system the laser beam, coming from an argon ion laser (488 nm), was directed towards the sample through an interference filter and via several mirrors. The interference filter narrowed the spectral width of the incident laser beam. Upon reflection and scattering of the light on the sample, usually a notch filter has the objective to reflect the laser wavelength and to transmit the scattered light from the sample. However, since the Anti-Stokes component was not analysed, an edge filter was used instead of the notch filter. On the sample side a confocal microscope was attached, which focused the laser via a 50X objective onto the probe, leading to a spot size of about 1 µm. To avoid damaging or overheating of the material due to high radiation densities, an additional filter has been used to adjust the excitation power density. The scattered light was spectrally resolved by an 1800-grating and detected on a CCD array.

3.6 Transmission electron microscopy

The employment of high resolution transmission electron microscopy (HR-TEM) for the characterization of thin film stacks allows an impressive insight into the properties and the structure of interfaces and grain boundaries in the sub-nanometer scale [96]. To achieve this, transmission electron microscopes are equipped with an electron gun in which the electrons are usually accelerated to energies of about 80 keV to 1200 keV and directed towards the specimen via several lenses. In a conventional TEM-setup the sample is

exposed to a parallel electron beam, allowing an analysis at a certain location on the sample. For a setup that allows a scanning of the sample via a specific area, the electron beam is focused onto the specimen. In both cases the electrons, impinging on the surface of the respective sample, are partly transmitted and partly diffracted at the lattice planes of the respective structure. Subsequently to the resurgence, the electrons are focused by an objective lens onto the imaging plane. The resulting picture of the samples lattice planes cannot be understood as a direct image. It originates out of the phase relation of the directly transmitted and diffracted electrons. Hence, the imaging of HR-TEM is based on phase contrast [83].

To obtain further information about the composition of the analysed area, an additional analysis can be performed by EDX. Equivalent to the above described XRF measurement, the focused electron beam is also capable of interacting with the electrons of the atoms inner shells. Subsequently to the emergence of an atom's electron an X-ray is emitted which can be analysed in a respective way [96]. To establish the relationship to the TEM-analysis, this compositional analysis is referred to as scanning TEM-EDX (STEM-EDX) in the following.

In order to apply TEM as characterization method, the analysed samples have to be very thin to allow the electrons to be transmitted. To achieve this, several different techniques like mechanical and ion polishing or plasma etching can be utilized. In the present case a focused ion beam (FIB) was used to sputter trenches into the film stacks and to obtain a thin lamella. With the help of an additional thinning step, using a FIB cross beam, the samples could be prepared to be analysed in TEM. A more detailed description of the introduced measurement techniques can be found in [96].

All measurements and preparations within in this work have been performed in close collaboration with the centre for nanoanalysis and electron microscopy at the department of material sciences VII at the University of Erlangen. For the sample preparation the tool is equipped with a Gatan ion polishing system and a ZEIS FIB cross-beam. The samples have been analysed using a C_S corrected transmission electron microscope FEI TITAN^3 80-300. The electron acceleration voltage was 300 kV. The complete setup allowed a resolution of 0.08 nm. For the TEM analysis itself a high angular annular dark field detector has been used. The system was also equipped with an EDAX-EDX setup, allowing line scans via the cross sections of the analysed samples.

3.7 Secondary ion mass spectroscopy

Another very powerful technique to analyse the composition of thin films is secondary ion mass spectroscopy (SIMS) [97]. This method is a destructive one, during which the elements of the probed material are sputtered from the surface into vacuum by an incident ion beam. During this process, the ionized atoms and molecules of the sample are analysed by a detector. Usually the identification of the particles is done via time of flight (ToF), magnetic sector or quadrupole mass spectrometers.

The ToF analysis is based on the acceleration of the secondary ions in an electric field. While the particles kinetic energy is given by an electric field, the mass can be calculated by measuring the time it takes the particle from the sample to the detector. An operation of the sputtering ion gun in a pulsed mode is a prerequisite for this method. Since the duty cycles have to be very small, a second ion gun is used to sputter a crater and to obtain the depth information. The magnetic sector method uses the Lorentz force to deflect the particles and direct them towards the detector. Knowing the strength of the magnetic field and the particles velocity, the charge to mass ratio can be determined. By altering the magnetic flux density a scan through different masses can be conducted. A quadrupole mass spectrometer uses an alternating high frequency electric field with a constant offset to filter certain charge to mass ratios passing through a tube with the respective poles.

In general, SIMS allows determining the composition of a probe from light to heavy elements down to very low impurity levels. Depending on the quality of the system setup, count rates of up to 10^9 s^{-1} with a background signal of 1 s^{-1} can be detected. Reducing the sputter rate to very low values, it is also possible to obtain information about the surface composition and to conduct a mapping on a micrometer scale resolution [97].

All measurements conducted within the scope of this thesis have been performed in close collaboration with Saint Gobain Recherche (SGR) in Paris. In the following, two different parameter settings are mentioned since the system setup has been changed during the progress of this thesis. The undoped In_xS_y layers have been characterized using a TOF-SIMS IV instrument from the company ION-TOF. For the analysis cycles, Ga^+ ions were accelerated to energies of 15 keV with a current of 3.0 pA. All doped buffer layers have been characterized inside an ION-TOF TOF-SIMS^5 instrument. In this case the analysis cycles have been performed using Bi_3^{++} ions at energies of 60 keV and a current of 0.38 pA. In both cases Cs^+ ions were used to sputter the crater into the sample. The

respective parameters were 3.0 keV at 70 nA for undoped and 2.0 keV at 120 nA for doped buffer layers.

3.8 X-ray diffraction

X-ray diffraction (XRD) is based on the effect of elastic scattering of photons at the electrons of atoms bound in a crystal [95]. With the contribution of the electrons of all the atoms bound inside a lattice plane, the beam is diffracted and leaves the plane at the same angle as it was incident to the surface. However, since the beam is not only reflected at one lattice plane but on several ones, optical interferences occur, leading to an interference pattern at certain angles of incidence. The interference condition is illustrated in Fig. 9.

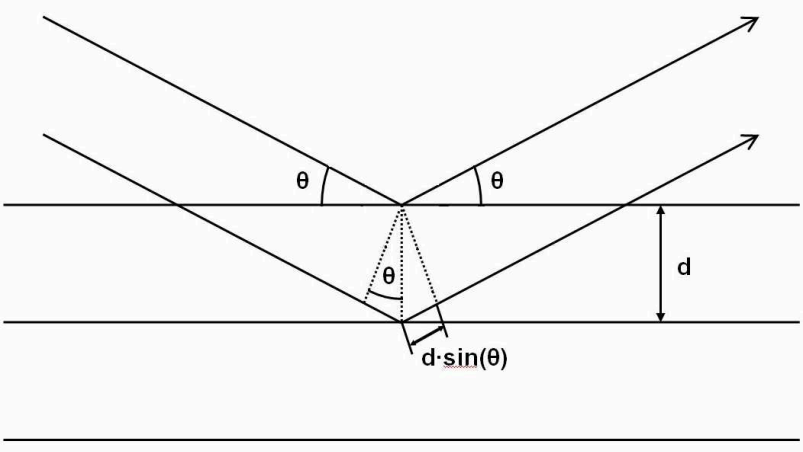

Fig. 9: Illustration for the derivation of Bragg's equation (after [95]).

One can deduce that a difference in the length of the optical path of $2d\cdot\sin(\theta)$ is caused by the reflection of a beam at two parallel lattice planes. For coherent photons this means that a detection of reflected X-rays is only possible when the optical path length difference is a multiple of the wavelength of the incident photons. The mathematical expression for this is given by Bragg's equation [95]

$$2d\sin(\Theta) = n\lambda, \tag{3.7}$$

where λ is the wavelength of the incident X-ray, d the distance of two lattice planes and θ the angle of incidence. n is a multiple integer. For a defined wavelength, the equation predicts that there are only certain angles where the interference is constructive and a reflection can be detected, depending on the distance of the lattice planes. The appearance of multiple reflections at designated angles is furthermore a characteristic fingerprint for

different material systems and phases. One has to be aware of the fact that only crystalline materials can be detected by XRD. As soon as the grains inside the analysed samples become too small or the probe is even amorphous, one will not be able to determine the presence of the material system inside the sample [95, 98].

Since a vast part of the analysed samples are polycrystalline, another specialty of the method becomes obvious. For the case of a randomly distributed orientation of the grains throughout the analysed volume, the diffracted rays' intensities are uniform. However, in case of a preferential orientation of the grains relative to the substrate or a seed layer, the intensities at certain angles become more pronounced [98].

XRD is also a very common technique to characterise thin films on substrates. This task can be challenging since an adequate number of grains are required to obtain sufficient signal intensity. Furthermore, the signals from the substrate might superimpose the information of the layer of interest. To reduce this effect and to be able to focus on the thin film on top of the substrate, the angle of incidence can be reduced to very low values, enlarging the analysed volume and also reducing the penetration depth of the x-rays into the substrate. In this case the angle of incidence is kept constant at values of about 1° and a scan for the respective Bragg angles is done by moving the detector. This technique is known as gracing incidence X-ray diffraction (GIXRD) [98].

All measurements were performed at the "Laboratorium für röntgenographische Materialcharakterisierung" in Munich. The utilized tool for the analysis of solids and powders was a transmission diffractometer with a focusing beam geometry after Guinier using a Type F goniometer supplied by Siemens. The respective Cu-$K_{\alpha,1}$ radiation has been generated inside a Siemens AGF4S X-ray tube. As a primary monochromator, a bent Ge (111) single crystal of the company Huber has been used, while a MW50 position sensitive proportional counter of the company Braun served as detector. All thin films have been characterized using a parallel beam diffractometer also with a Siemens Type F goniometer, which was equipped with a parabolic multi-layer-optic (Göbel-mirror) of the company Incoatec for the beam formation. The measurements have been conducted under grazing incidence at an angle of about 0.5°, using Cu-$K_{\alpha,1}$ and Cu-$K_{\alpha,2}$ radiation of an equivalent X-ray tube as used for the powder diffraction. On the detection side, the tool is equipped with a Soller-collimator and a scintillation counter from Siemens.

4 The deposition of indium sulphide buffer layers by evaporation

4.1 The thermal evaporation process of In_2S_3

In 1963 Miller et al. [99] already found that In_2S_3 sublimates at elevated temperatures as In_2S and S_2 molecules, while Ferro et al. [100] re-investigated the evaporation behaviour and also confirmed the observation, that the vapour pressure of In_2S is about 10^3 higher than the one of S_2 during the initial part of the process. This was the case until about 1 % of the material has been evaporated in both studies. For the remaining material, it has been reported that the vapour composition remains constant throughout the complete evaporation process. The reason for the imbalance during the initial phase of the evaporation might be related to the sulphur deficiency of the surface due to air exposition, prior to the evacuation in the vacuum chamber. Hence, the handling in ambient conditions should be reduced to a minimum level.

The above stated characteristic of a stable equilibrium of the partial pressures of In_2S and S_2 are the prerequisite of a long term stable processing with reproducible compositions of the deposited thin films. From the phase diagram in Fig. 4 one can conclude that it should be possible to heat up pure tetragonal In_2S_3 to its melting point of 1090 °C without any decomposition of the material. However, from own experiments during which the temperature has been increased up to 1000 °C, it became clear that this behaviour is not realistic, since the tested materials melted far below this temperature. The phase diagram indicates that a critical temperature might be reached at 852 °C already. Since the integral composition of the material has to shift towards the In-richer side from this point, one can conclude that a significant part of the sulphur will evaporate into the gas phase. Hence, the residual amount of material inside the crucible becomes more and more In-rich. This indicates that the material features small inhomogeneities in composition, causing a non-ideal behaviour.

A practicable way to reduce this effect does find its application within the molecular beam epitaxy. Here, the source materials are often evaporated from effusion cells. Inside these cells the crucible, holding the respective source material, is typically heated by two independent filaments. In the present case, the crucible has a cylindrical shape and can consist of various materials like quartz, Al_2O_3 or BN. One filament, located in the lower area, is responsible to heat up the source material, while the second filament stabilizes the

temperature in the upper area well above the one of the source material. This is done to avoid recondensation of the evaporated material at the outlet of the crucible, which would lead to an accretion at this position. By deploying an additional insert with a smaller opening aperture than the diameter of the crucible, it is possible to obtain a stable equilibrium of the partial pressures inside the crucible. This approach can help to countervail a decomposition of the source material and enhance the long term stability of the evaporation process. Besides this, the utilization of an insert reduces the time dependence of the evaporation rate since the influence of the surface area reduction over process time decreases.

Usually, the In_2S_3 source material is commercially supplied as powder, with a particle size in the order of micrometers. However, loading the In_2S_3 into a crucible in this form leads to material loss since a part of the powder is sucked out during the evacuation process. Therefore, the material was pressed into tablets before loading it into the effusion cell. This approach also has the advantage of an increased loading capacity, owing to the higher density in comparison to the powder form.

The deposition of the buffer layer is done inside a vacuum chamber at a pressure of about $5*10^{-6}$ mbar. During the process the substrate is located face down on a rotating sample holder and coated in many steps with thin layers, while passing the effusion cell. A sketch of the respective arrangement inside the vacuum chamber and an enlargement of the effusion cell itself are depicted in Fig. 10.

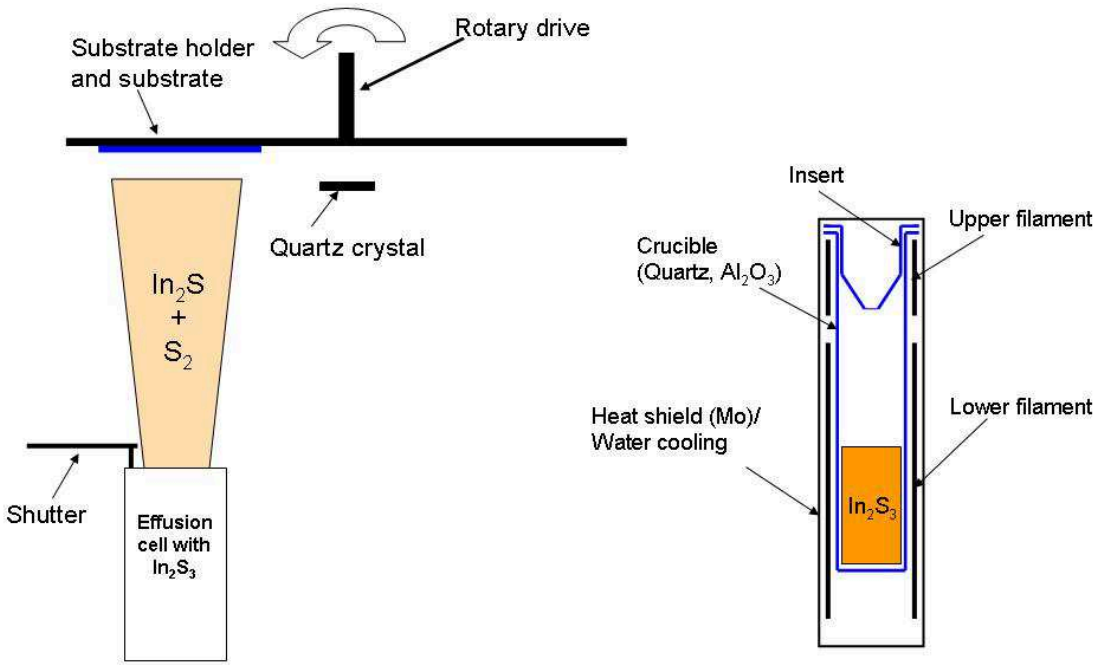

Fig. 10: Sketch of the equipment arrangement inside the process chamber (left) used for the deposition of In_xS_y buffer layers and a cross section of an effusion cell (right).

To be able to conduct several consecutive depositions without breaking the vacuum, the substrates can be loaded and unloaded via a load lock, attached to the chamber. Hence, it is possible to simulate a continuous process inside a large scale production line without the need to cool down the source between successive depositions. An additional sample heater (not shown in Fig. 10) is attached above the rotating substrate holder in order to vary the substrate temperature. The heater is able to raise the temperature of a rotating sample to about 150 °C.

4.2 Variation of the S/In ratio

Within the scope of this thesis it has been found that the S/In ratio has a significant effect on the properties of the deposited layers and also on the respective solar cells and modules. Consequently, it was desirable to be able to control and adjust this parameter for the deposited films. Several approaches have been developed to vary the composition of the In_xS_y buffer layers on the substrate. The two most effective ones are described in the following and have been submitted for patenting [101].

In the previous chapter it has been outlined that In_2S_3 sublimates in the form of In_2S and S_2. Since the two molecules obtain masses that are very different from each other and exhibit different chemical properties, they feature different coefficients for the sticking and reemission probability on the surface of the substrate and other equipment parts inside the vacuum chamber. Thus, a distinct amount of sulphur can be detected in the atmosphere during the process with the help of a residual gas analysis. This sulphur is available for deposition on the substrate and a reaction with the already present In-rich film, since In_2S has a higher sticking probability. Hence, by reducing the partial pressure of sulphur inside the chamber, one can adjust how much sulphur is available for such a reaction. This can be reached by the utilization of a certain area, where the sulphur can either react chemically, e. g. at copper shields, or where it can be bound physically, e. g. an actively cooled trap. Both approaches have been found to be very efficient and are quantified in Fig. 11. The increase in In-content of the processed films is plotted versus the total area of copper introduced into the chamber (a), while the same parameter is depicted in dependence of a controlled temperature of a cooling shield (b).

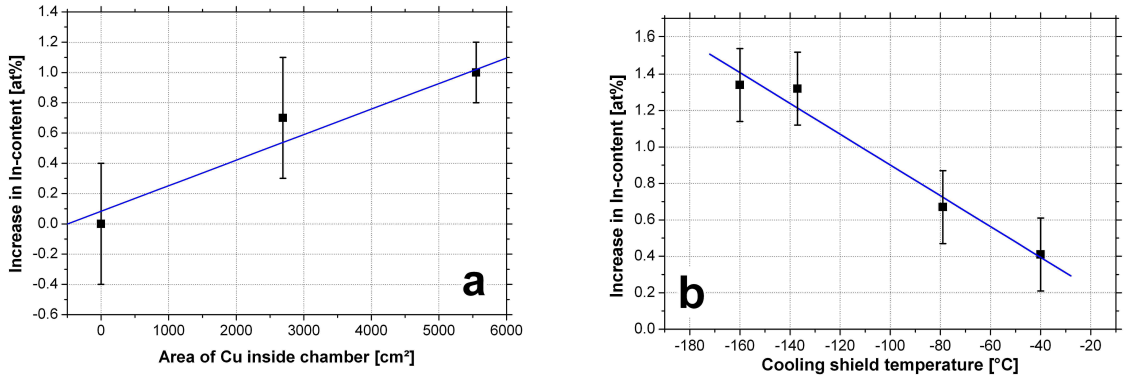

Fig. 11: Increase in In-content as a function of the area of Cu (a) and of the temperature of a cooling shield (b) inside the vacuum chamber.

From Fig. 11(a) one can conclude that the exposition of an increasing area of copper inside the chamber increases the In-content with an extent of up to 1.0 ± 0.2 at%. The result of an experiment during which the temperature of a cooling shield has been adjusted with a certain flow of liquid nitrogen is shown in Fig. 11(b). Here, a maximum increase of 1.4 ± 0.2 at% has been reached. Hence, the desired In-content of an In_xS_y layer can be tuned by either varying the area of copper inside the chamber or by an adjustment of the temperature of a cooling shield.

For the case of an introduction of copper foil into the chamber, the sulphur and the copper react to the composition of CuS. Within the scope of this work it has been found that the reaction does not stop after the surface of the exposed area has been converted, but that the copper completely corrodes to CuS. Hence, the composition can be kept stable throughout an extended amount of time.

The utilization of a cooling shield has the advantage that the composition can be adjusted without the need of breaking the vacuum and hence allows a variation of this parameter within a short response time. During subsequent warm up of the cooling shield, the trapped sulphur is released again since its vapour pressure at room temperature is higher than the base pressure of the equipment used.

By combining both methods, one can reach relatively high In-contents of up to 43.5 at%. A further increase can be reached by evaporating decomposed In_xS_y that has been heated up to temperatures above the already stated critical value of 852 °C. In this case one has to be aware that this approach does not serve for long term stable conditions. However, to gain knowledge about the characteristics of such films, the process has been found to be reasonable stable for single depositions. All buffer layers with In-contents higher than 43.5 at% have been deposited using this approach.

4.3 The source material

As mentioned in chapter 2.3.2, the In_xS_y buffer layer can be deposited by various techniques. At AVANCIS and within the scope of studies conducted at cooperating institutions [39], some of these layers have already been tested with varying success, while the most promising one has been found to be PVD from compound In_2S_3. This method allows very low film contamination with third elements [44] and can be easily implemented into a full vacuum production line, which is a prerequisite for cost efficient manufacturing of solar modules.

In the beginning of the work done for the present thesis, several issues existed regarding the supply of high quality In_2S_3 source material, allowing a process with a reliable reproducibility and long term stability. Therefore, it became necessary to identify the relevant material properties that are responsible for efficiency losses or for issues with respect to the mentioned long term stability, during continuous processing. The analysis methods used to find these differences were XRF for elemental impurities, XRD for phase composition and titration for stoichiometry. While the material vendors usually only specify the metal based elemental purity, this value has been assumed to be reliable.

Comparing the conversion efficiency of solar cells with In_2S_3 buffers, originating from source materials from different vendors, it has been found that the metal based elemental purity is of essential importance. In this context, it was possible to specify a purity of 99.999 % that has to be met in order to obtain a high level in the electrical properties of the respective solar cells. The thorough determination of the specific elements being responsible for efficiency losses was not possible due to time restrictions of this thesis.

Besides the metal based impurities, an oxygen contamination of up to 12 wt% has been measured by XRF in some cases. However, it was not possible to detect specific O-containing phases by XRD. Thus, the specific bonding inside the material is unknown. Nevertheless, heating up such O-rich compositions towards the process temperature resulted in unstable long term conditions regarding the thin films composition. Furthermore, an XRD analysis of the remaining material revealed that an In_2O_3 phase has formed during the evaporation process, resulting in the decision of not using materials with such high oxygen contaminations as source material.

A third important material specification that arose out of a comparison of compounds from different vendors was based on the occurrence of deficiencies regarding

the nominal stoichiometry of In_2S_3. Deviations from this specification were already visually assessable since the material showed a greyish colour in contrast to the usually orange or red one of stoichiometric In_2S_3. It was possible to assign the reason for this observation to the presence of a mixture of pure In, InS and In_6S_7 by an XRD measurement.

With the analytical results obtained for the materials that allowed to deposit buffer layers for solar cells with good conversion efficiencies and also led to long term stable processes, it was possible to formulate the main criteria that need to be met for a reproducible process development. These are listed in Table 2.

Table 2: Summary of crucial demands on In_2S_3 as source material for the buffer layers in CIGSSe solar cells.

Related criteria	Specification
Metal based elemental purity	99.999 % (different methods)
Non metal based elemental purity	Oxygen contamination below 1.0 wt% (XRF)
Structure	Tetragonal with no detectable secondary phases (XRD)
Stoichiometry	S/In=3/2 ± 1 at% (Titration)

A complete avoidance of oxygen is not realistic, since the material is hygroscopic [102]. Here, it can be noted that about 0.4 wt% of oxygen can be estimated to originate from the surface of the analysed samples. A total measure of 1.0 wt% of oxygen, determined by XRF, has been found not to cause any problems for processing and growth of the respective buffer layers. With the demand for a tetragonal structure, a specification towards the stoichiometry is inherent. This results out of the fact, that In_2S_3 features a cubic structure for In-contents higher than 40.5 at% [42], as mentioned in chapter 2.3.1. However, since it is also possible that the material could contain a certain amount of sulphur or indium in an amorphous structure, which might not be detectable by XRD, an additional specification of the stoichiometry is still required. One has to be aware that this requirement can not be characterized by XRF since the information depth of the technique (about 3.6 µm for In-L_α radiation) is smaller than the particle size of the material (about 10 - 15 µm). Hence, one would predominantly analyse the surface of the particles, which tends to be sulphur deficient. This can be concluded out of the fact that In_2S_3 releases an H_2S odor, which has to originate from the surface. Characterising the material composition by XRF after different exposition times to air confirmed this predication with an appearing increase of the relative In-content and lead to values of more than 44 at% for tetragonal In_2S_3. A reliable characterisation of the bulk material regarding the stoichiometry can be done by titration.

5 Properties of indium sulphide buffers in dependence of the S/In ratio

The following chapters will outline the effects that have been found to arise out of a variation of the indium sulphide buffer layer's stoichiometry. In the first place, the discussions will regard both, structural and optical properties in dependence of the S/In ratio. Furthermore, the respective interdependencies within CIGSSe thin film solar cells and the influences of the variation on the electrical properties will be discussed. A layer system for thin film solar cells using such indium sulphide buffer layers has been submitted for patenting [103].

5.1 Raman analysis of bulk indium sulphide

From the phase diagram one can conclude that the S/In ratio of bulk In_xS_y is correlated to the phase composition of the material. Since different phases are expected to feature different signals in Raman spectroscopy, the source material has been characterized initially. β-In_2S_3 features the following Raman lines: 42, 57, 61, 70, 102, 113, 137, 180, 196, 217, 244, 266, 306, 326, 367 cm^{-1} [104]. These values have been compared to the Raman signals of the In_2S_3 source material used for this work (see chapter 4). The summarized Raman signal of three individual measurements, recorded at different locations on an In_2S_3 tablet is shown in Fig. 12. For a better comparability to the nominal Raman bands of In_2S_3 from the literature, the respective positions are indicated by vertical lines.

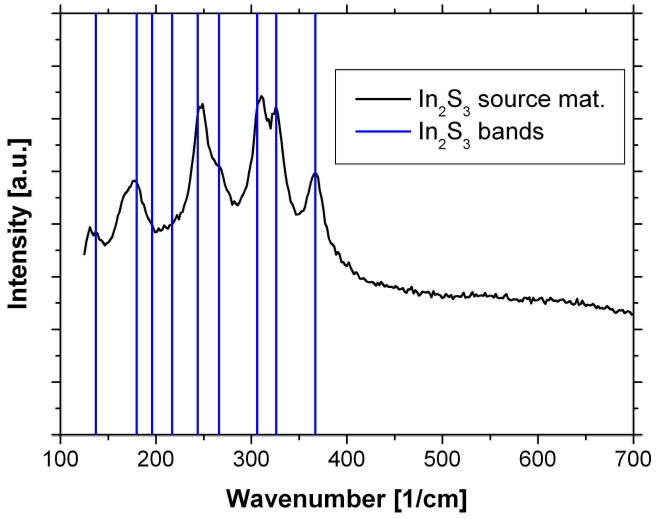

Fig. 12: Raman spectrum obtained from In_2S_3 source material together with the nominal Raman bands obtained from the literature [104].

Within the analysed range of wavenumbers one can find very good agreement of all Raman bands to the nominal values of β-In_2S_3. The excitations at 196 cm^{-1} and 217 cm^{-1} also showed a relatively low scattering probability in the literature, which explains the missing intensity at the respective wavenumbers. Referring to the requirement of a stoichiometric composition of the source material, Raman spectroscopy can hence be assumed to be capable to verify the compliance to this specification.

To assess a probable phase contamination and to be able to assign it accordingly, a literature review has been conducted for the Raman signatures of α-In_2S_3, InS and In_6S_7, too. According to Faradzhev et al. [105], the Raman lines of InS can be found at the wavenumbers: 43, 60, 68, 95, 152, 162, 219, 223 and 319 cm^{-1}. However, to the author's knowledge no Raman spectra of α-In_2S_3 and In_6S_7 have been published so far. Nevertheless, the spectra of α-In_2S_3 and β-In_2S_3 have been expected to be similar, as both phases exhibit very similar IR reflectivity spectra [104, 106].

In order to be able to determine the Raman lines of In_6S_7, a residual material has been analysed that has been heated up to about 880 °C for about 8 hours. Since this temperature is beyond the critical temperature of 852 °C, the material experienced a decomposition, which resulted in a melting of the tablet. According to an XRD analysis, this residual material has been found to consist of a mixture of orthorhombic InS, monoclinic In_6S_7 and cubic In_2S_3, which is depicted in Fig. 13 (a) for a selected range of diffraction angles. The respective summation of three Raman spectra at different locations of the residual is shown in Fig. 13 (b). To be able to compare the experimental data to the values of the literature, the nominal positions of β-In_2S_3 and InS are also indicated as vertical lines in the graph.

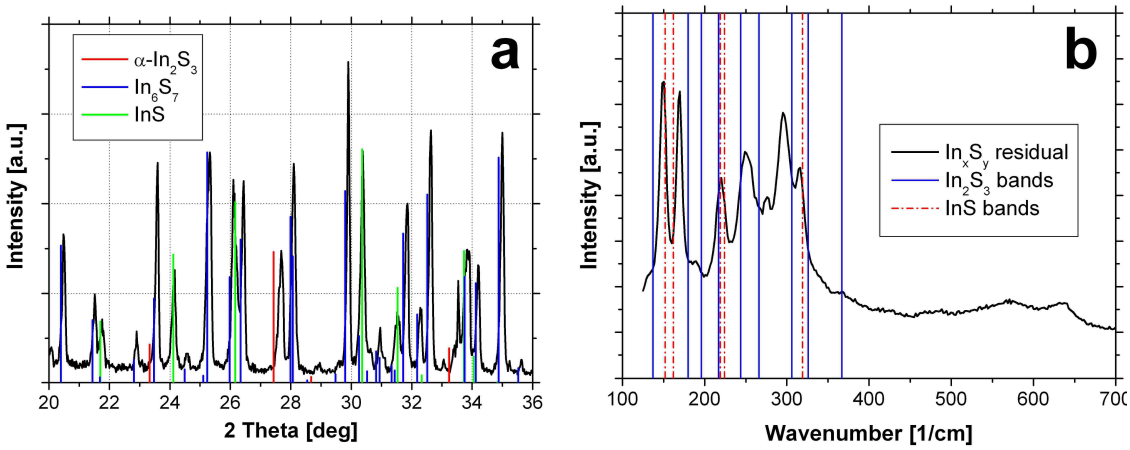

Fig. 13: XRD spectrum (a) and Raman spectrum (b) of residual In_xS_y material after exceeding the critical temperature of 852 °C for 8 h.

From a comparison of Fig. 12 and Fig. 13 (b) one can deduce that a significant amount of both InS and In_6S_7 was present inside the sample, since several new lines appeared in the spectrum. Especially the two signals with the highest intensities in the spectrum at about 150 cm^{-1} and 170 cm^{-1} outline that the amount of the secondary phases is dominating the contribution to the integral composition. Additionally, this observation is supported by the almost vanished signal at 367 cm^{-1}, indicating that hardly any In_2S_3 (either α or β) was left inside the sample. Under consideration of a slight shift in the position of the wavenumbers (± 3 cm^{-1}) one could associate three of the additional lines to the phase of InS. However, a vast part of the spectrum cannot be explained by the lines of In_2S_3 and InS. Hence, a significant amount of the lines most likely originates from In_6S_7. Their respective positions are assigned and depicted in Table 3.

Table 3: Overview of the Raman band positions of InS, In_6S_7 and β-In_2S_3, compiled from literature and own measurements [104, 105].

β-In_2S_3 (cm^{-1})	In_6S_7 (cm^{-1})	InS (cm^{-1})
137	170	152
180	191	162
196	251	219
217	272	224
244	278	319
266	297	
306		
326		
367		

It is not quite clear to which phase the weak signals at 570 cm^{-1} and 641 cm^{-1} can be attributed to, since literature data for InS and β-In_2S_3 was only found up to a wavenumber of about 400 cm^{-1}.

5.2 Raman spectroscopy of indium sulphide thin films on glass

As shown in the previous chapter, a simultaneous presence of all three indium sulphide phases (In_2S_3, In_6S_7 and InS) is possible for bulk material. Since it is of major interest in which way In_xS_y grows on a substrate, several thin films with different S/In ratios have been deposited and analysed by Raman spectroscopy on soda lime glasses (SLG) and on the CIGSSe-absorbers. However, the CIGSSe-absorber also features pronounced Raman lines in parts of the same regions like In_xS_y does. Hence, the spectra of the In_xS_y buffer layers interfere with the ones of the substrate, aggravating the interpretation

of the spectral changes. Therefore, the shown evaluations refer to the measurements on SLG only. Nevertheless, it can be mentioned that all conclusions drawn have been found to be transferable to the depositions on the CIGSSe-absorber.

A comparison of Raman spectra of two thin films with an integral In-content of 39.9 ± 0.2 at% and one with 43.9 ± 0.2 at% is depicted in Fig. 14, outlining the coexistence of several phases inside the analysed samples. The integral compositions have been determined by XRF.

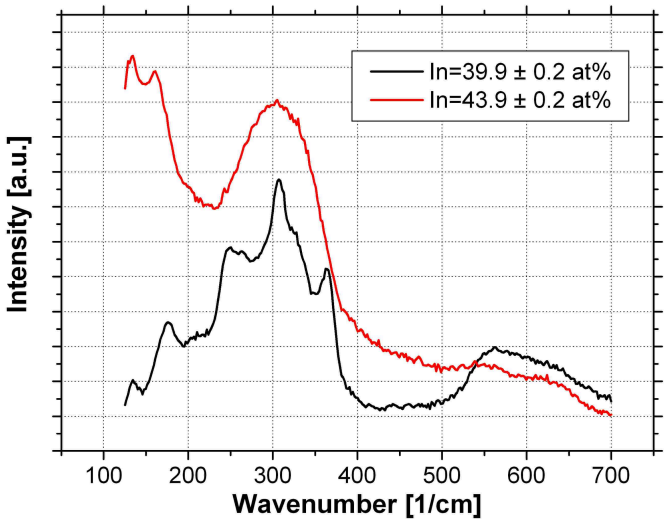

Fig. 14: Raman spectra of two In_xS_y thin films on glass with different In-contents.

In the same way like in the comparison of the analysed source material in Fig. 12 and Fig. 13 (b), a strong increase of the Raman intensity in the wavenumber region between 125 cm^{-1} and 200 cm^{-1} becomes obvious. Furthermore, one can see that the spectrum of the stoichiometric layer shows a slightly declining gradient with increasing wave numbers, while the In-richer film shows an inclining one. The first effect can be attributed to an increase in the phase contribution of InS or In_6S_7. The second effect might be related to different fluorescence behaviour [94], while the broader signals in the region above 400 cm^{-1} originate from the SLG, as determined from measurements of uncoated glass. A third, very important and apparent distinction between the two spectra is the missing pronounced lines in the wavenumber region of 240 cm^{-1} and 400 cm^{-1}. This observation can be associated with a reduced grain size in the analysed material, as the full width at half maximum (FWHM) of the single lines depend on the crystallinity of the analysed material (see chapter 3.5). This means that the more fine crystalline a sample is, the broader the respective peaks will become. Considering that the phases of InS, In_6S_7 and In_2S_3 feature different lattice structures, one can understand that the formation of these phases at the

same time are impeding the crystal growth of each other. Hence, one can assume that a decreasing integral S/In ratio of a thin film is accompanied by a decreasing crystallinity.

To support these conclusions and to obtain an alternative measurement technique to XRF, an empirical approach for the quantification of the phase composition in thin films on glass has been developed, which is based on the respective Raman spectra. First, it was necessary to limit the effect of different background inclinations in the spectra in order to avoid a falsification of the evaluation by different fluorescence behaviour of the analysed samples. This can be done by the definition of a linear baseline with several reference points between 400 cm^{-1} and 500 cm^{-1} and one more at 700 cm^{-1}. As it can be concluded from Fig. 14 for an In-content of 39.9 ± 0.2 at%, only very low contents of In_6S_7 or InS should be present inside the film. Therefore, the respective Raman intensity of the lines below 200 cm^{-1} is reduced to relatively low intensities.

Assuming that the phases in thin films behave as indicated in the phase diagram for bulk material, an increasing In-content inside the layer has to increase the amount of In_6S_7 and InS. As shown above, this is accompanied by increasing peak intensities in the region of wavenumbers below 200 cm^{-1}. Thus, one can use this area to quantify the amount of secondary phases inside the films. To avoid a dependence from a variation of the overall signal intensity, which might be related to fluctuations in the laser power or slight variations in the focussing of the laser beam on the substrate, the quantification can be done by the calculation of a quotient from defined integrals at selected parts of the spectrum. For these types of evaluation, the measurement program provides the possibility to define several Gaussian-Lorentzian-curves with designated peak positions. The peak intensities and the FWHM can be fitted in such a way that the complete spectrum is emulated. The mathematical product of both characteristics (amplitude and FWHM) of the single peaks can be used to appraise the area underneath them. Fig. 15 shows an example of this technique for a fitted spectrum, while Fig. 16 depicts a comparison of normalized spectra with successively increasing In-content under consideration of the subtraction of the linear baseline. To achieve a better comparability a value of 0.1 has been added to every data point to separate the spectra from each other.

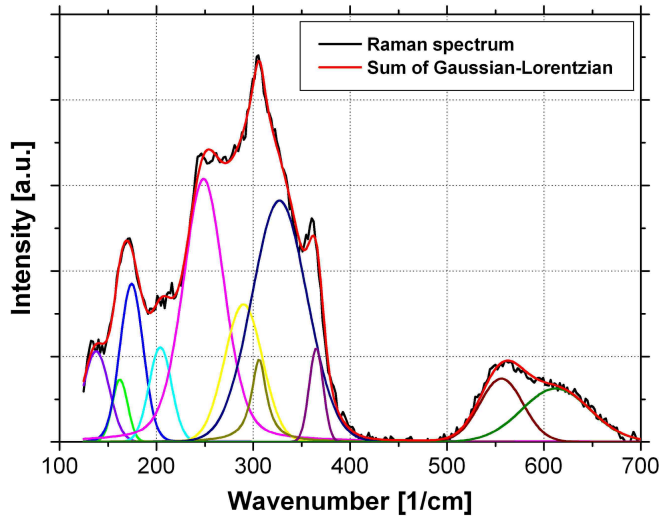

Fig. 15: Example for the result of a fit procedure of a Raman spectrum via several linear combinations of Gaussian and Lorentzian functions of an In_xS_y thin film on glass with an In-content of 40.7 ± 0.2 at%.

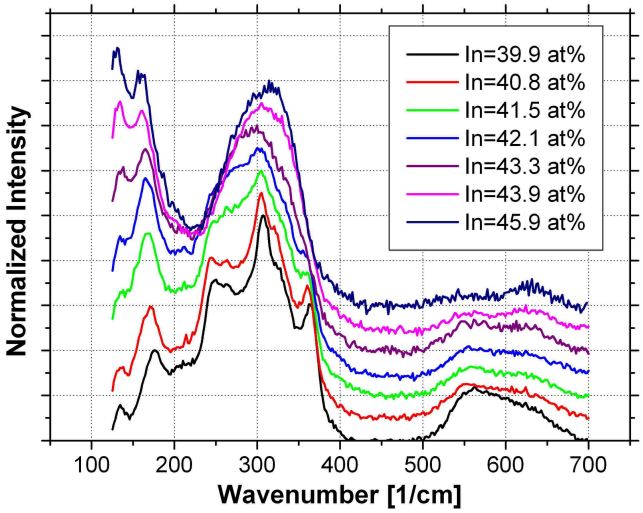

Fig. 16: Comparison of several Raman spectra of In_xS_y thin films on glass with varying In-contents (Standard deviation for XRF-measurements equals 0.2 at%).

Most likely due to matrix effects, individual peaks experience some shifting in their position in dependence of the S/In ratio. Therefore, their positions are not always at the identical wavenumber as stated in Table 3 but are chosen in a way that a good fit can be obtained for the process relevant variation in the S/In ratio. In order to limit the degrees of freedom, it has been avoided to introduce all peak positions. This has been found to be necessary to increase the reproducibility of the fit results. Nevertheless, by calculating the ratio of the spectral intensity from 125 cm^{-1} to 200 cm^{-1}, mostly originating from In_6S_7 and InS, to the signal in the range from 200 cm^{-1} to 400 cm^{-1}, a very good correlation to the integral thin film composition was achieved. This dependency is depicted in Fig. 17 and

referred to as “Raman ratio”. The spectra used for this evaluation are the same ones as shown in Fig. 16. For every data point, two different macroscopic spots with three variations in their microscopic location have been measured per sample to obtain a higher statistical reliability. Furthermore, the latter three spectra have been summarized to average the obtained information. The respective error bars indicate one standard deviation based on the average of two evaluations.

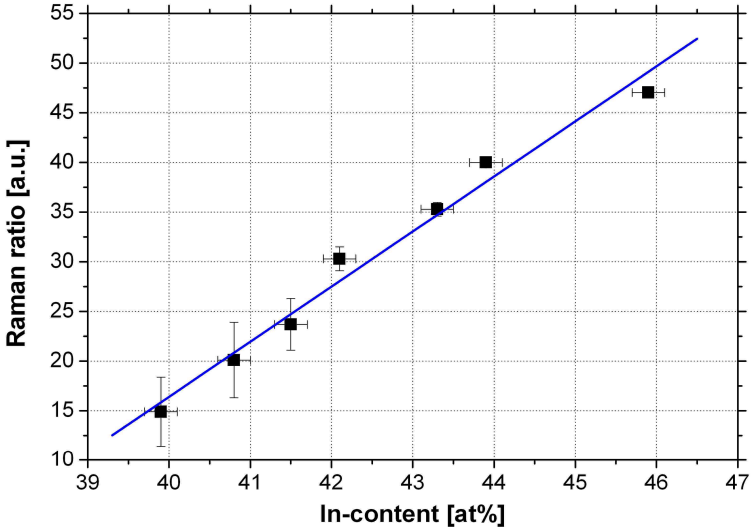

Fig. 17: Correlation of the Raman ratio, determined by Raman spectroscopy, to the integral film composition, determined by XRF.

This evaluation technique clearly correlates an increasing In-content to an increasing phase contribution of In_6S_7 and InS. Because of the different lattice structures of the three phases, this is accompanied with a reduction of the crystallinity and should hence lead to smaller grains inside the film. As already mentioned above, the same conclusions hold for In_xS_y layers deposited on absorber layers. A slight modification of the evaluation technique described above, allows the determination of the buffer layers composition directly on the CIGSSe absorber. Since the latter contains both In and S, a direct quantification of the buffer’s composition on the absorber by XRF is not possible anymore. Hence, this alternative characterization technique becomes important for the verification and the control of the process stability without the use of witness glasses.

5.3 Secondary ion mass spectroscopy of In_xS_y thin films on absorber layers

In chapter 2.3.3 it has been mentioned that several research groups already found a significant interdiffusion of elements at the CIGS-In_xS_y interface [43, 70, 71, 75]. Furthermore, it was shown that the amount and type of foreign elements can have a significant influence on the electrical and optical properties of the buffer layer itself. Hence, a characterization of the composition of the buffer layer as it persists inside the complete solar cell should enhance the understanding of its influence on the solar energy conversion efficiency. Since Pistor [43] outlined that a significant part of the elemental diffusion only happens at elevated temperatures, it is important to characterize the buffer layer after all processes have been conducted, that are necessary for the fabrication of the complete solar cell. Especially the deposition of the *n*ZnO layer, conducted at about 200 °C, is expected to induce a change in the composition of the In_xS_y buffer layer and its interface to the CIGSSe-absorber with respect to the "as deposited" situation. In general, ToF-SIMS is known to possess sufficient resolution to obtain reliable depth information on elemental composition in thin films. However, due to a pronounced surface roughness of the absorber and a total ZnO thickness of about 1.3 µm on top of the buffer film, it is rather unlikely to gain clear information about the buried, thin buffer layer. To resolve this issue, it was decided to selectively remove the *i*ZnO and *n*ZnO layer of fully processed solar cells. This can be done with the help of an acetic solution. An etching of the buffer layer during this step can be avoided by using diluted glacial acetic acid (CH_3COOH) with 50 % deionised water [107]. After an etching time of about 5 min the window layer was completely removed. Subsequently, the samples have been characterized by sputtering slowly through the In_xS_y buffer into the absorber layer by ToF-SIMS.

For this analysis three cells with different buffer compositions have been chosen. Their In-contents were 39.9 ± 0.2 at%, 43.0 ± 0.2 at% and 45.9 ± 0.2 at% with thicknesses of 81.7 ± 0.2 nm, 88.4 ± 0.2 nm and 90.2 ± 0.2 nm, respectively. The complete profile (a) and a magnification of the Cu distribution (b) are shown in Fig. 18. The distribution of Na can be found in Fig. 19. The intensities have not been normalized and are shown as they were measured.

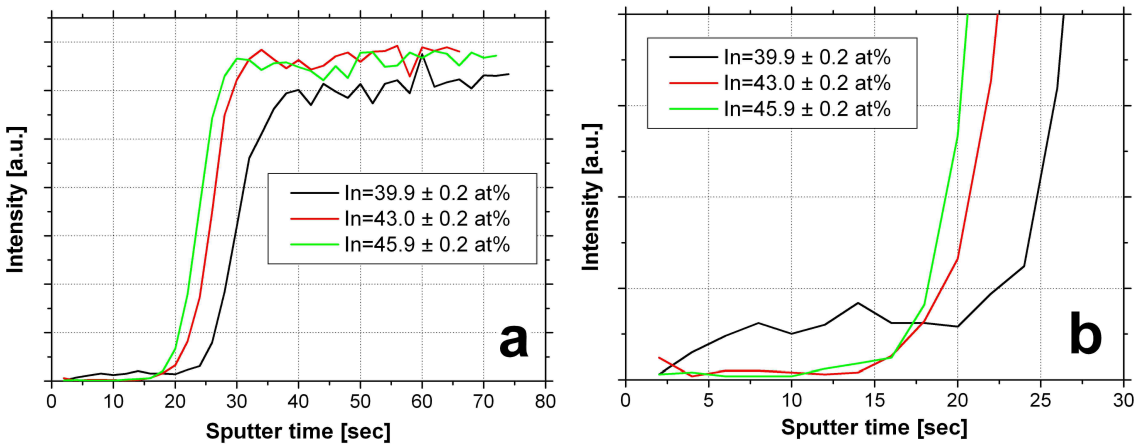

Fig. 18: ToF-SIMS profile of the Cu distribution starting from the surface of the buffer layer into the absorber (a) with a magnification of the buffer region (b).

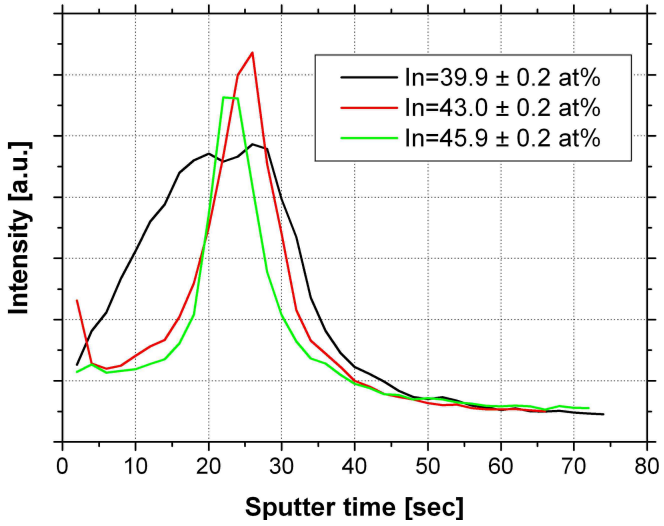

Fig. 19: ToF-SIMS Profile of the Na distribution starting from the surface of the buffer layer into the absorber.

From the steep increase in the intensity of the Cu signal in Fig. 18 one can conclude that the In_xS_y buffer layer has been sputtered through after about 20 seconds. The difference in the apparent thickness of the buffer layer with an In-content of 39.9 ± 0.2 at% can most likely be related to composition dependent sputtering yield. Nevertheless, Fig. 18 (b) clearly shows that hardly any Cu diffusion has been taken place in the cases where the In-contents were 43.0 ± 0.2 at% or 45.9 ± 0.2 at%. In contrary to this, the profile for an In-content of 39.9 ± 0.2 at% features a well measurable Cu signal throughout the buffer region. Furthermore, the reduced slope of the Cu signal at the beginning of the absorber layer for the sample with the stoichiometric buffer indicates a loss in Cu at this place, which supports the hypothesis stated above.

In the case of the Na distribution in Fig. 19, one can see a pronounced peak at the interface between the buffer and the absorber at about 25 sec. This is not surprising since

earlier analyses (not presented here) of the uncoated absorber layer already showed that a certain amount of Na is present at the absorber's surface [70]. From this point some of the Na apparently diffuses into the buffer layer towards the front electrode. In comparison to the buffer with nominal stoichiometry, both In-richer buffer layers show relatively moderate incorporation of Na, while the peak of the former one is significantly broadened.

Summarizing, one can conclude that the SIMS analysis showed an increased diffusion of Cu and Na into the buffer layer for samples with In-contents close to the nominal value of In_2S_3 with respect to the ones with higher In-contents. The reason could be related to the reduced crystallinity of buffer layers with In-rich compositions, as it was deduced form the Raman analysis. An accompanied lower diffusivity with more fine crystalline structures could explain an impeded Cu and Na migration into the deposited In_xS_y buffer layers.

5.4 High resolution transmission electron microscopy

In order to verify the SIMS measurements and the Raman results, high resolution transmission electron microscopy (HR-TEM) was applied to analyse the structure of the prepared In_xS_y buffer layers, embedded in CIGSSe solar cells. This has been done in collaboration with the group of Prof. Dr. Spiecker at the University of Erlangen [108]. However, due to the substantial effort for the sample preparation and the analysis itself, it was only possible to conduct this method on two representative samples.

The most obvious changes in the characteristics of the In_xS_y film are expected within a comparison of a stoichiometric buffer layer and one with a significantly higher In-content. Hence, two corresponding cells have been chosen for this characterization. Two samples, originating from neighbouring positions of an absorber layer, have been selected to avoid any potential interaction with the characteristics of the absorber layer. According to XRF analysis of the reference film samples on glasses, the two buffer layers featured an In-content of 40.4 ± 0.2 at% and 41.9 ± 0.2 at%. The thicknesses have been determined to 85 ± 0.2 nm and 79 ± 0.2 nm, respectively. The corresponding HR-TEM images of the buffer layers between the *i*ZnO/*n*ZnO front electrode and the absorber layer are shown in Fig. 20 and Fig. 21.

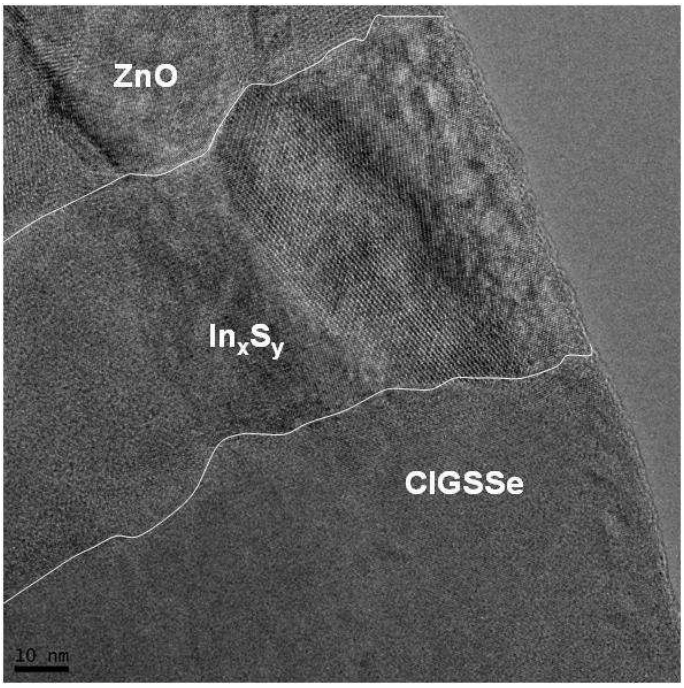

Fig. 20: HR-TEM picture of an In_xS_y buffer layer with an integral In content of 40.4 ± 0.2 at%.

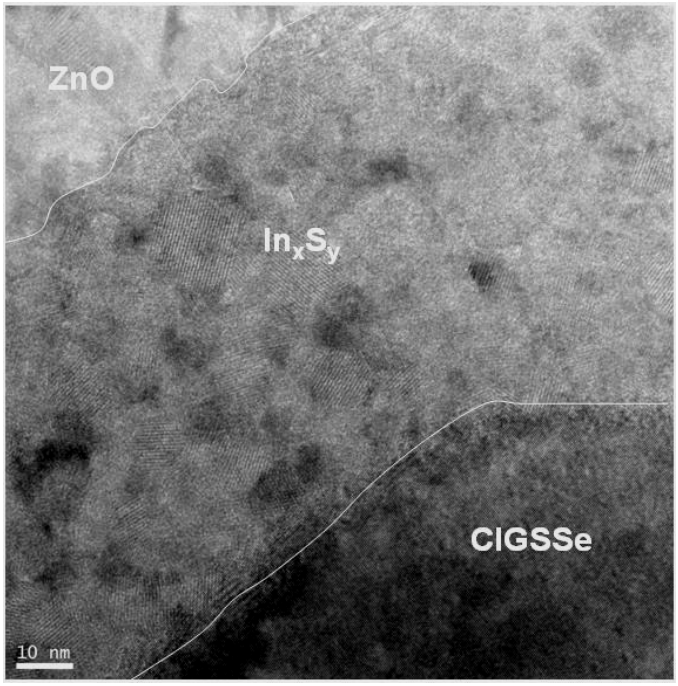

Fig. 21: HR-TEM picture of an In_xS_y buffer layer with an integral In content of 41.9 ± 0.2 at%.

A comparison of these two micrographs clearly reveals that the grain size is significantly reduced for the buffer layer with the higher In-content. From Fig. 20 it can be seen that the grain size already reaches the thickness of the buffer layer, while there are only smaller grains visible in Fig. 21. Referring to the hypothesis of an enhanced elemental diffusion when the buffer layer features a more pronounced crystallinity, a comparison of Fig. 20 and Fig. 21 gives reason for the assumption that it is enhanced for lower In-

contents. The more fine crystalline layer in Fig. 21 would therefore act as a more effective barrier for diffusion. An evaluation of the average grain sizes in these two buffer layers lead to values of about 30 nm ± 20 nm for the layer with an In-content of 40.4 ± 0.2 at% and 10 nm ± 20 nm for the one with an In-content of 41.9 ± 0.2 at%.

In order to verify if those expected differences in elemental diffusion can be observed directly, the thin lamella has been characterized via a line-scan across the buffer layer from the absorber to the front electrode by STEM-EDX. The respective profiles of the elemental compositions are depicted in Fig. 22 and Fig. 23.

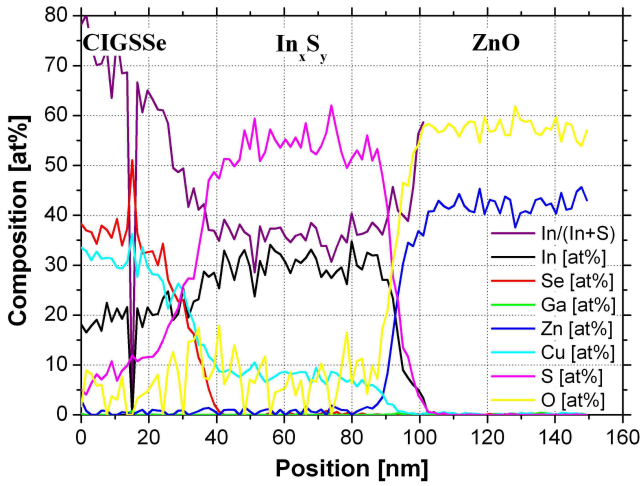

Fig. 22: Graph of a STEM-EDX profile regarding the composition of a buffer layer with a nominal In-content of 40.4 ± 0.2 at%.

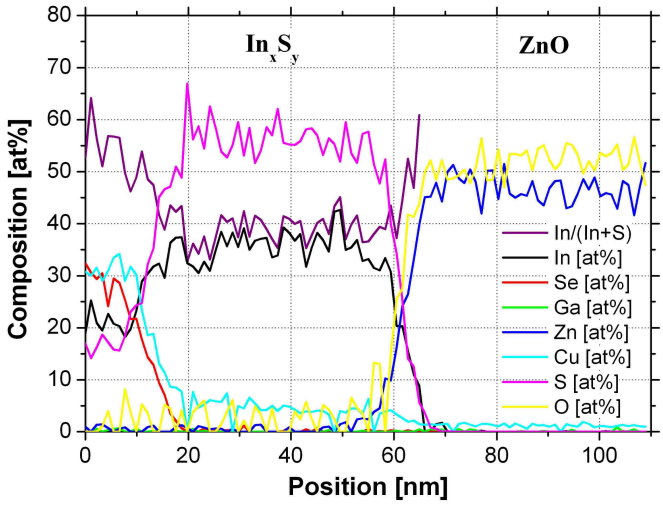

Fig. 23: Graph of a STEM-EDX profile regarding the composition of a buffer layer with a nominal In-content of 41.9 ± 0.2 at%.

Following the scanned direction one can see a steep increase in the sulphur content, which marks the beginning of the buffer layer. The increase in the Zn-content corresponds to the beginning of the front electrode. For both cases one can identify a pronounced in-

diffusion of Cu throughout the whole buffer layer. However, when comparing the Cu-profiles it becomes obvious that the buffer layer with the lower In-content of 40.4 ± 0.2 at% has been penetrated by a higher amount of Cu. To quantify the difference, Table 4 lists the average contents for both samples. As one can deduce from a direct comparison of the nominal In-contents of the buffer layers and the In/(In+S) ratio determined by STEM-EDX, the latter one is slightly reduced in both cases. This might be associated to uncertainties in the measurement of the applied technique. Nevertheless, consistent to the XRF-analysis of the reference glasses of the respective deposition, the sample in Fig. 23 shows a higher In-content than the one in Fig. 22.

In contrast to the behaviour of Cu, no clear diffusion of Se into the buffer has been found in both samples. Furthermore, the recorded intensity for a diffusion of Na into the buffer layer was below the resolution of the used STEM-EDX setup of about 1 at%.

The reason for the relatively large difference in the oxygen contents of the *i*ZnO layers might be related to according residuals on respective surface, while the deviation of the In/(In+S) ratio to the In-content determined by XRF on witness glasses could also be associated to calibration issues or the lower resolution of the EDX setup.

Table 4: Comparison of the obtained amount of Cu diffused into the In_xS_y buffer layer in dependence of its In-content.

In-content (at%)	Evaluated depth (nm)	Average Cu-content (at%)
40.4 ± 0.2	40 - 88	8.4 ± 1.2
41.9 ± 0.2	20 - 58	4.6 ± 1.7

Summarizing the results obtained by HR-TEM and STEM-EDX, one can conclude that a deposition of In_xS_y close to its nominal stoichiometry leads to significantly larger grains as compared to buffer layers with a higher In-content. Hence, this method of analysis confirmed the conclusions deduced from Raman spectroscopy in chapter 5.2. As a result of the enhanced grain size, it became obvious that the In_xS_y thin film is more susceptible for an in-diffusion of Cu when the layer is deposited close to its nominal stoichiometry. This observation is also consistent with the conclusions drawn from the SIMS analysis.

5.5 *Optical properties of indium sulphide thin films*

5.5.1 The Tauc-Lorentz oscillator

The fundamental band gap is one of the most characterized optical properties of semiconducting thin films. As discussed in chapter 3.4, this value is commonly ascertained via transmission and reflection measurements and determined via a Tauc plot [29, 53, 73, 86]. However, this approach entails a rather high uncertainty and incomparability due to the utilization of different formulas for the calculation of the absorption coefficient, the assumption of different types of band gaps (direct or indirect) and the subjective choice of fit area to the Tauc plot. Hence, it is desirable to be able to characterize the thin films with a different technique that doesn't have these drawbacks. Within this thesis a series of samples with different S/In ratios have been characterized by spectroscopic ellipsometry on SLG. To obtain the optical characteristics from these measurements, a mathematical model had to be chosen that was capable to describe the film's attributes. For the In_xS_y thin films, the Tauc-Lorentz model has been found to fulfil this task. According to Jellison et al. [109], this model is adequate to describe amorphous layers. The imaginary part of the dielectric function is based on the Tauc expression multiplied with a Lorentz oscillator, leading to [109]

$$\varepsilon_2(E) = \frac{AE_0\Gamma(E-E_g)^2}{E[(E^2-E_0^2)^2+\Gamma^2E^2]}\cdot\Theta(E-E_g), \qquad 5.1$$

where E_g is the optical band gap, E_0 the peak in the combined density of states, Γ a broadening factor and A a prefactor that includes the optical transition matrix elements. Θ is the Heaviside Theta function with $\Theta(E<0)=0$ and $\Theta(E\geq 0)=1$ [110]. Therefore, this model is only valid for interband transitions. Responses from infrared transitions, the Urbach tail or core transitions can not be described with this approach.

The real part of the dielectric function can be obtained by a Kramers Kronig integration of ε_2, which leads to [109]

$$\varepsilon_1(E) = \varepsilon_1(\infty) + \frac{2}{\pi}P\int_{E_g}^{x} d\xi \frac{\xi\varepsilon_2(E)}{\xi^2-E^2} \qquad \mathbf{5.2}$$

with P, the Cauchy principal part of the integral and $\varepsilon_1(\infty)$ as the high frequency dielectric constant. Usually $\varepsilon_1(\infty)$ equals 1, but it can be larger than this value for the case of a

significant optical transition outside the range sampled by the ellipsometer. From both ε_1 and ε_2 the complex refractive index can be calculated via the formulas [95, 109]

$$\varepsilon_1(E) = n^2 - k^2 \quad 5.3$$

$$\varepsilon_2(E) = 2nk, \quad 5.4$$

where n is the refractive index and k is the extinction coefficient.

5.5.2 Modelling and measurement

Since the polarized light of the ellipsometer is not only reflected at the surface, but is also transmitted through the film and into the glass, this effect has to be taken into account. In any case, the refractive index of the substrate has to be determined in order to evaluate the reflection from the glass-film-interface. Furthermore, one has to be aware that a significant amount of light is reflected from the backside of the substrate. Depending on the thickness of the glass substrate and the size of the measurement spot, it is possible that this signal superimposes with the reflected light from the thin film surface and the film-glass-interface. Since the thickness of the substrate is not part of the model, the additionally detected signal would result in a falsification. Hence, it is necessary to blind out this reflex, which can simply be done by a roughening of the substrate's backside.

As stated in the previous chapter, the Tauc-Lorentz model is capable to describe the optical properties of the In_xS_y thin film upon reflection on the sample. However, due to a certain complexity of the optical features, it has been found that one single oscillator can not describe the measured data. This can be associated to spectral ranges with different absorption behaviour, which will be discussed below. Thus, a second oscillator has been implemented into the model. This introduction was capable to improve the fit quality significantly. Since the thin films have been exposed to air and also feature a certain surface roughness, a so called effective medium approximation layer has also been introduced on top of the stack. This layer represents a mixture of the characteristics of the ambient and the bulk material. In addition to the optical parameters of the oscillators, the fit procedure included both the film and the surface thickness with its roughness.

Since the most interesting part of the In_xS_y thin film's spectrum is centred around 2.0 eV, the characterization was set to values between 300 nm and 820 nm. Every sample has been measured under seven different angles of incidence to increase the amount of data

available for the fit procedure. This enhances the reliability of the obtained coefficients. The quality of the subsequent fit results, quantified by the mean square error (MSE), strongly depended on the starting values of the two Tauc-Lorentz oscillators. It was hence necessary to vary the start values and to compare the results in order to obtain the global minimum of the MSE. The measured data points of Ψ and Δ for a sample with an In-content of 43.1 ± 0.2 at% and the respectively fitted model are depicted in Fig. 24 for the different angles of incidence.

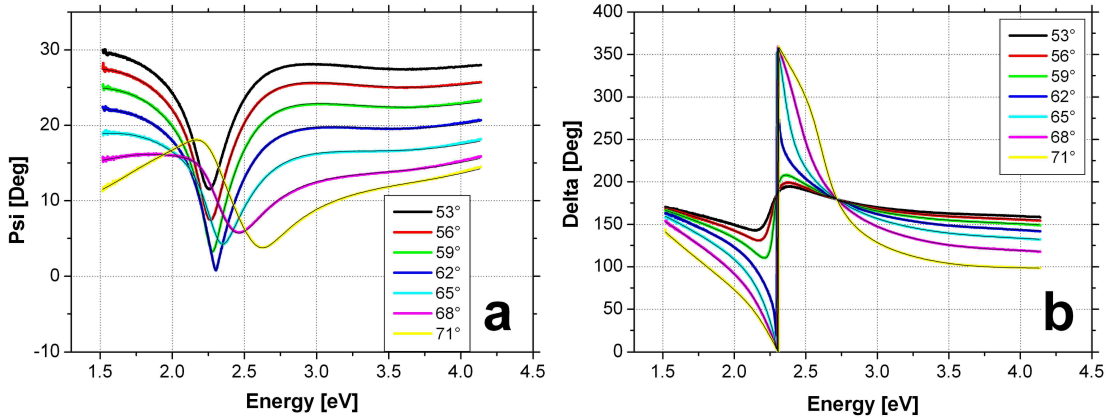

Fig. 24: Plot of the fitted Tauc-Lorentz model to the measured data of Ψ (a) and Δ (b) for a buffer layer with an In-content of 43.1 ± 0.2 at% on glass under varying angles of incidence.

Once the fit with the lowest MSE was found for one sample, the respective set of coefficients has been used as start parameters for the sample with the closest variation in the S/In ratio. In this way it was possible to gain very good fit qualities for the complete series of analysed films.

5.5.3 Refractive indices and band gaps of indium sulphide buffer layers on glass

Taking into account that thin films with varying compositions consist of different phase contributions, it is likely that their optical properties are altered by this influence. Referring to this context, Fig. 25 and Fig. 26 show the evolution of the refractive index n and the extinction coefficient k obtained by spectroscopic ellipsometry for thin films with varying In-contents.

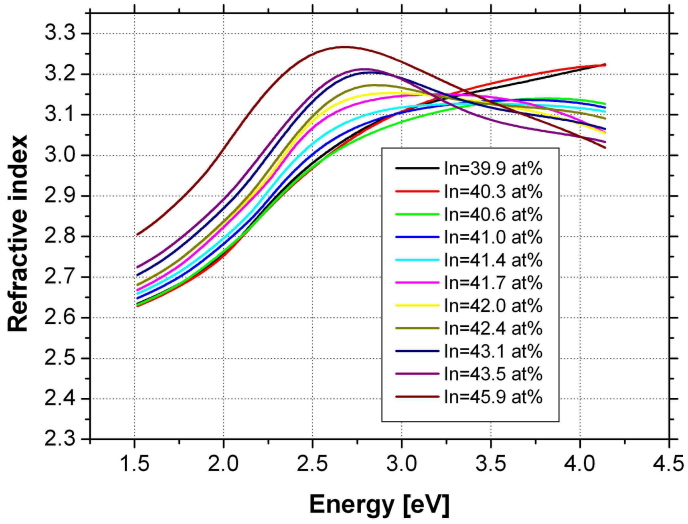

Fig. 25: Refractive index of In_xS_y buffer layers in dependence of the photon energy for varying In-contents (Statistical error of In-contents equals ± 0.2 at%).

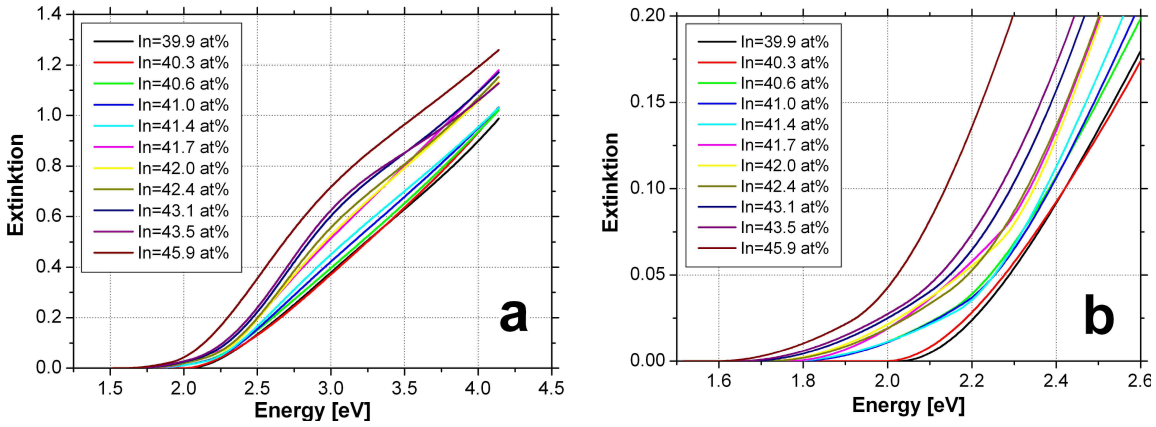

Fig. 26: Extinction coefficient of In_xS_y buffer layers in dependence of the photon energy for varying In-contents (a) with a magnified view (b) of the energy region near the band gap on the right side (Statistical error of In-contents equals ± 0.2 at%).

From Fig. 25 one can conclude that the refractive index continuously increases towards higher In-contents for energies smaller than about 2.5 eV. Within this region, the optical behaviour of the thin films is consistent with most transparent materials. However, for higher photon energies, an increasing anomalous dispersion does occur, which becomes more dominant for higher In-contents. According to the literature [92], this effect is known to happen in spectral areas with strong absorption. Taking into account that these films have an increasing content of the In_6S_7 phase with a band gap of about 0.7 eV [111], the enhanced absorption becomes plausible.

The evolution of the extinction coefficient in Fig. 26 is consistent with this observation and proves that the absorption of the films is significantly increasing towards higher In-contents. Furthermore, the magnified view of the graph in the energy region close to the band gap in Fig. 26 (b) outlines that the band gap continuously decreases with

increasing In-contents. Besides this, it can be clearly deduced that the films have an optically indirect transition for In-contents above 40.5 ± 0.2 at%. This follows from the relatively moderate increase in absorption until a direct transition becomes possible at higher energies [95]. In contrary, the films with 39.9 ± 0.2 at% and 40.3 ± 0.2 at% show a significantly reduced low energy absorption tail. This behaviour still indicates an indirect band gap, but a second direct transition from the valence band to the conduction band becomes possible for photon energies very close to the band gap energy of the indirect transition. The described evolution for stoichiometric In_2S_3 is supported by band structure calculations conducted by Barreau et al. [55]. To quantify the behaviour of the declining band gap, the coefficients of the band gap parameters of the two Tauc-Lorentz-Oscillators are depicted in Fig. 27.

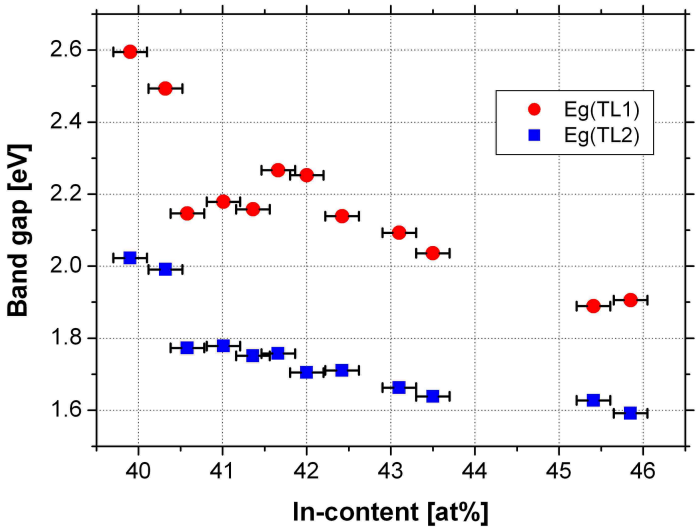

Fig. 27: Evolution of the band gaps delivered by the two Tauc-Lorentz oscillators of the ellipsometer model (Standard deviation of the band gap within five repetitive measurements on one sample equals ± 0.003 eV).

In this graph TL2 represents the value of the optical band gap. In case of the films with In-contents above 40.5 ± 0.2 at%, the value of TL1 can be understood as the energy limit from which on direct transitions from the valence band to the conduction band are possible. For In-contents below 40.5 ± 0.2 at% this observation does not meet the described behaviour. Since these films already show a character close to a direct behaviour and the extinction coefficient does not indicate a stronger absorption at this value, it can be assumed that TL1 is not of essential meaning for the description of the optical behaviour. A modelling of the respective data with only one oscillator has been found to result in the same band gap of about 2.0 eV with an increased MSE for the fit quality. Nevertheless, it can be mentioned that Rehwald et al. [54] also found another critical point at an energy of

2.5 eV for absorption measurements on single crystals, which would be comparable to the values of TL1 at the respective composition.

Moreover, Fig. 27 reflects a change in the absorption behaviour by a discontinuity in the evolution of the onsets of the extinction coefficient. Both films with an In-content below 40.5 ± 0.2 at% have a significantly larger band gap than the ones with lower S/In ratio. At this point, the value of 2.0 eV is consistent to the band gap stated for single crystal In_2S_3 [54]. Beyond the limit of 40.5 ± 0.2 at% the band gap continuously decreases from 1.8 eV to 1.6 eV at an In-content of 45.9 ± 0.2 at%.

As already discussed in the literature review, In_xS_y features a phase transition from β-In_2S_3 to α-In_2S_3 (tetragonal to cubic structure) when increasing the In-content above a value of 40.5 ± 0.2 at% [42]. Assuming that the bulk characteristics of In_xS_y also persist in thin films, the appearance of a discontinuity in the evolution of the band gap might be originated in this transition. Taking into account that the lattice parameters also show a significant change during the transition and that the band gap depends on this value [95], this argumentation becomes plausible.

Summarizing the observations, the dependency in the width of the band gap on the In-content of the In_xS_y buffer layer could also explain part of the discrepancies in the optical properties of buffer layers reported in different publications [44]. Especially the contradictions in the type of the band gap might be related to slight variations in the buffers composition as it can be concluded from the evolution of the extinction coefficient in Fig. 26.

5.6 Electrical properties of solar cells in dependence of the S/In ratio

5.6.1 Main parameters

It has already been observed that the electrical and optical properties of In_xS_y buffer layers strongly depend on the film composition [29, 44, 51, 53]. The discussion mainly focused on the influences of the respective impurity levels. In this context, it has been found that good conversion efficiencies can be obtained for sulphur deficient buffer layers [57, 112]. However, up to now no detailed investigation over a wider range of the S/In ratio has been published.

Since it is already known from the previous sections that the optical and structural properties significantly change with the S/In ratio, one can assume that there has to be an optimum value for a maximum in the conversion efficiency. To outline this dependency,

Fig. 28 and Fig. 29 show the main parameters of the best solar cells of two cell strips on a 5x10 cm² substrate with a total of 16 cells versus the buffer's In-content. For this experiment the respective absorber layers have been coated with In_xS_y buffer layers with large variations in the S/In ratio, followed by ZnO layers, front contacts and cell patterning. The evaluation of the best cell per strip has been done to emphasize the potential in the electrical properties that can be reached at the respective composition. To avoid any interaction with possible variations of the properties of the absorber layer, all values shown refer to solar cells fabricated on neighbouring parts of the same absorber. In addition to the data points for the cells with an In_xS_y buffer, the plots also show the reference values for a cell with a CdS buffer, indicated by a horizontal line in the graphs.

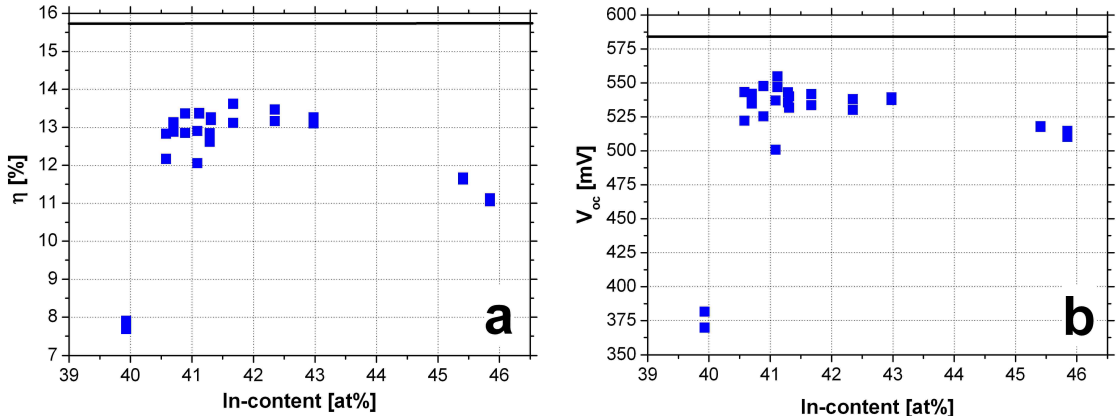

Fig. 28: Conversion efficiency (a) and open circuit voltage (b) for best solar cells as a function of the S/In ratio of the In_xS_y buffer layer (Statistical errors out of repetitive measurements: In-content: ± 0.2 at%; η: ± 0.1 %; V_{oc}: ± 0.5 mV).

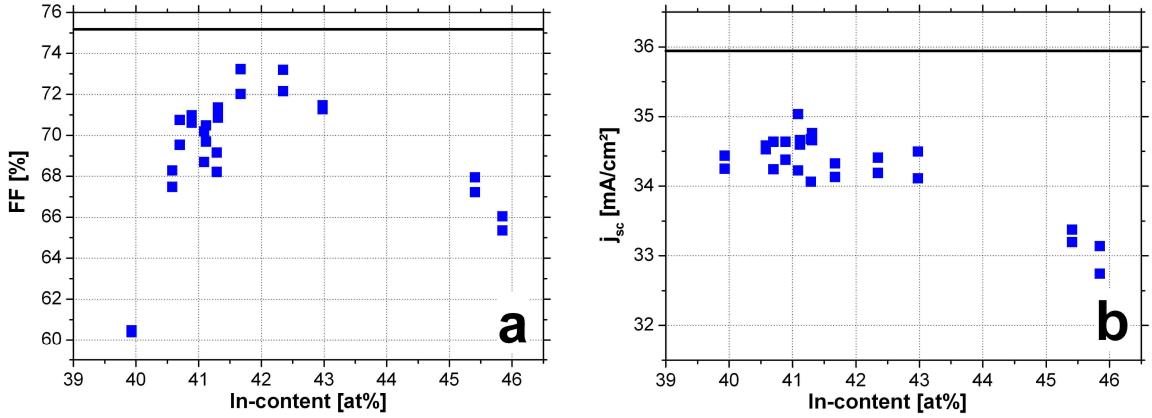

Fig. 29: Fill factor (a) and short circuit current density (b) for single solar cells as a function of the S/In ratio of the In_xS_y buffer layer (Statistical errors out of repetitive measurements: In-content: ± 0.2 at%; *FF*: ± 0.1 %; j_{sc}: ± 0.1 mA/cm²).

A clear dependence of solar cell performance on the buffer layer composition is observed. The efficiency degrades towards the nominal composition of In_2S_3, strongly driven by a drop in open circuit voltage and fill factor. Besides this decay, Fig. 28 (b) also

shows that the achievable open circuit voltage is hardly influenced when the buffer's In-content varies in the range of 40.5 at% and 43.0 at%. However, a slight loss in open circuit voltage is observed when an In-content of 43 at% is exceeded. The fill factor, depicted in Fig. 29 (a), features a distinct maximum at about 42 at%. Moreover, a stronger decay of this parameter into the direction of stoichiometric In_2S_3 becomes obvious when comparing it to the In-richer side. In contrary to fill factor and open circuit voltage, the short circuit current density does not show a drop for the stoichiometric composition. However, towards higher In-contents of the buffer, a reduction of the current density becomes obvious, as shown in Fig. 29 (b).

The decrease in current density can already be understood in connection with the results from the characterization by ellipsometry. Here, it has been shown that the extinction coefficient increases with steeper inclination for higher In-contents. Within a solar cell this leads to an enhanced absorption of photons in the buffer region and hence lost potential for the generation of electron hole pairs in the absorber layer (see also chapter 2.2.1).

Since the band gap of the buffer layer does not change significantly within the range of 40.5 ± 0.2 at% and 43.0 ± 0.2 at% (about 0.1 eV), it can be assumed that there is also hardly any changes in the band alignment from the buffer to the absorber in the same region. However, proceeding towards stoichiometric In_2S_3 the results from spectroscopic ellipsometry indicate a change in absorption behaviour, while the SIMS and STEM-EDX analyses state a significant diffusion of Cu and Na into the buffer layer. These variations might be responsible for an unbeneficial electronic situation with respect to the formation of an offset in the conduction band at the interface, what will be discussed in more detail in the next chapter.

The combination of the three parameters (V_{oc}, FF, j_{sc}) leads to the conversion efficiency η, which is plotted in dependence of the buffer layer's composition in Fig. 28 (a). As it can be seen, a maximum can be deduced at an In-content of about 42 at%. Regarding the strong decay below 40.5 ± 0.2 at% and considering a safety margin for process fluctuations, one can define an utilizable process window for the composition of the In_xS_y buffer layer from 41.5 at% to 43.0 at%. Besides the general trends discussed so far, the figures also depict that all main parameters show a significant gap to the respective values obtained by solar cells with a CdS buffer layer. Referring to this, Table 5 quantifies these differences for the best cells each.

Table 5: Electrical characteristics of the best solar cell within the described experiment in comparison to the values obtained for the best cell with a CdS buffer.

Buffer	In_xS_y	CdS
η (%)	13.6 ± 0.1	15.8 ± 0.1
V_{oc} (mV)	542 ± 0.5	584 ± 0.5
j_{sc} (mA/cm²)	34.3 ± 0.1	35.9 ± 0.1
FF (%)	73.2 ± 0.1	75.2 ± 0.1

Since an achievement of high conversion efficiency is of essential meaning to be competitive on the solar cell market, this comparison outlines that further development of the In_xS_y buffer process has to focus on closing these gaps and possibly even surpass the CdS reference values.

5.6.2 Secondary parameters

Within the thin film stack several characteristics have a significant influence on the electrical properties of solar cells. As an example, the conductivity of the front electrode affects the series resistance of a module. Furthermore, it is possible that certain changes in the region of the *pn*-junction can alter recombination paths [34]. As previously discussed, the so called secondary parameters in equation 3.2 are capable of describing these changes in the electronic behaviour of cells and modules [113]. Hence, the knowledge upon the dependencies of these parameters on the buffer composition should increase the understanding about the loss mechanisms and can therefore lead to new ideas of how to optimize the layer's attributes for better conversion efficiencies. In this context, Fig. 30 depicts the dependencies of the shunt (a) and series resistance (b) from the In-content of the buffer layer. Furthermore, Fig. 31 describes the relation of the ideality factor (a) and the saturation current density (b) to the buffer's composition.

Due to the fact that the series resistance is evaluated via a linear regression to the illuminated diode characteristic (see chapter 3.1), Fig. 30 (b) shows the respective dependency for the illuminated diode characteristic (IDC), only. For all other cases of the remaining secondary parameters, the evaluation has been done for both, the illuminated and the dark diode characteristic (DDC), using the standard fitting procedure described in chapter 3.1.

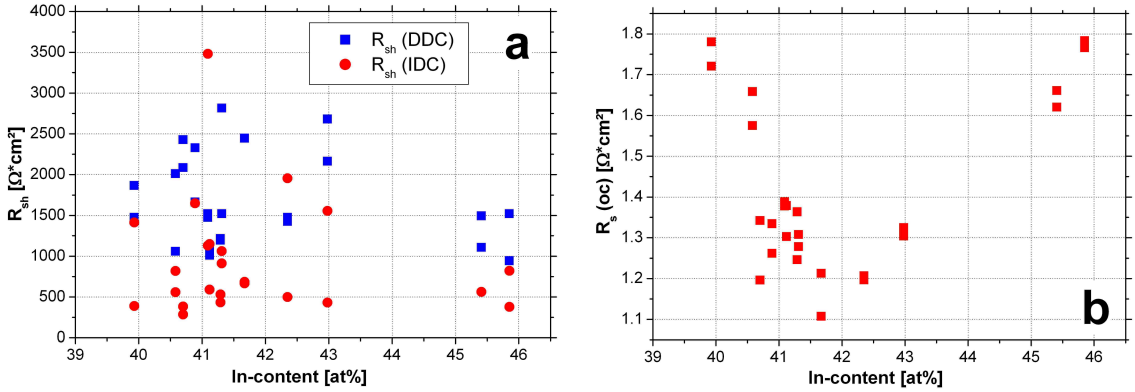

Fig. 30: Shunt resistance (a) for both DDC and IDC and series resistance (b) for the IDC of solar cells in dependence of the In-content of the In_xS_y buffer layer (Statistical errors out of repetitive measurements: In-content: ± 0.2 at%; R_{sh} (DDC): ± 252 Ohm*cm²; R_{sh} (IDC): ± 1638 Ohm*cm²; $R_s(oc)$ ± 0.02 Ohm*cm²).

As it can be seen in Fig. 30 (a), the shunt resistance of the DDC is somewhat higher than the one of the IDC, which can be attributed to a certain photoconductivity of the In_xS_y buffer. This increase in conductivity under illumination has also been observed for single crystals by Ho et al. [114]. Also taking into account that the statistical error for the values of the IDCs shunt resistance are very large, no clear correlation between the shunt resistance and the S/In ratio of the In_xS_y layer can be deduced for both parameters. It should be noted that the values of three outliers are outside the plotted area.

In contrary to the shunt resistance, the series resistance does show a clear dependency on the buffer's composition. From Fig. 30 (b) it can be concluded that a local minimum exists for an In-content of about 42 at%. For a deviation from this composition to both sides, a substantial increase in the series resistance from about 1.1 Ohm*cm² to 1.8 Ohm*cm² can be deduced. This observation could either be explained by the appearance of a conduction band offset or changes in the photoconductivity of the buffer layer due to the varied S/In ratio [30] and will be discussed in more detail in chapter 5.6.3.

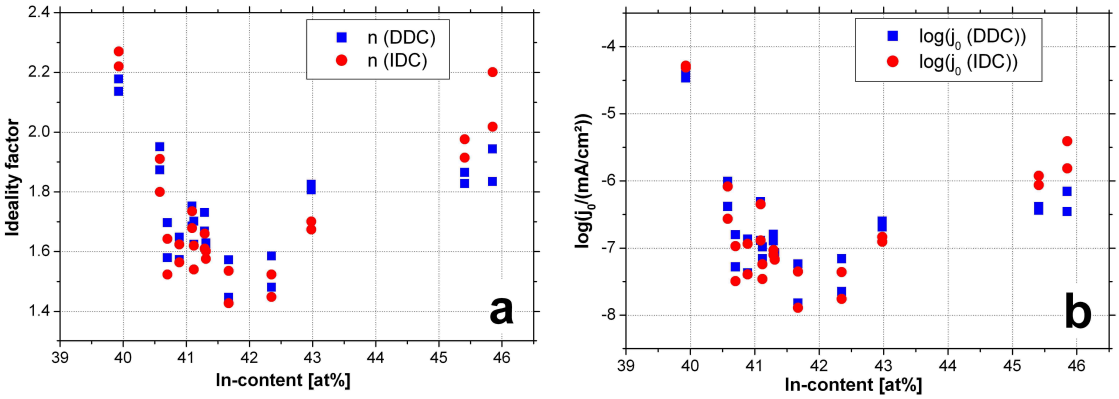

Fig. 31: Ideality factor (a) and saturation current density (b) of single solar cells in dependence of the In-content of the In_xS_y buffer layer for both the DDC and the IDC (Statistical errors out of repetitive measurements: In-content: ± 0.2 at%; *n* (DDC): ± 0.2; *n* (IDC): ± 0.1; log(j_0 (DDC)): ± 0.2; log(j_0 (IDC)): ± 0.2).

The ideality factor, displayed in Fig. 31 (a), shows a minimum of about 1.4 at an In-content of around 42 at% and increases to values above 2.0 for stoichiometric In_xS_y as well as for In-contents above 45 at%. Both, DDC and IDC fit values are in good agreement. Referring to an ideal solar cell, recombination processes caused by a limitation of the diffusion length in the field free bulk region of the absorber lead to an ideality factor of 1. Recombination in the space charge region yields a value of 2. Values larger than 2 can usually be seen in cases of tunnelling enhanced recombination processes [115] and interface recombination [116]. As stated in chapter 3.1, the evaluations of the *jV* characteristics conducted during this thesis are based on a 1-diode-model. Hence, it can be concluded that the value of the ideality factor represents the contributions of the different recombination mechanisms present in the respective solar cell, since the ideality factor is a free parameter for the *jV* fit procedure. Thus, the values obtained between In-contents of 40.5 at% and 43.0 at% suggest that the dominant recombination happens in the bulk and in the space charge region. At In-contents of about 40 at% or above 45 at%, one can assume that a significant part of the generated electron hole pairs recombine via tunnelling enhanced processes or defects at the buffer absorber interface. Consequently, this means that the band alignment between buffer and absorber changes significantly between an In-content of 40 at% or 45 at% and In-contents of about 42 at%.

The dependency of the saturation current density on the buffer layers In-content shown in Fig. 31 (b) confirms this observation. Similar to the ideality factor, a minimum at about 42 at% can be seen for both the DDC and the IDC, while a strong increase of more than three orders of magnitude can be observed for either de- or increasing In-contents. Since the saturation current density features attributes of the solar cell behaviour under reverse bias, the increase in this value can be understood as a certain current flow through

the *pn*-junction in opposite direction [117]. For solar cells with only few recombination or shunt paths in the junction, this value should be very small and should only increase for the cases where such paths are present. Taking into account that no dependency of the shunt resistance from the S/In ratio has been found in Fig. 30 (a), the evolution of the saturation current density also indicates that the recombination behaviour is significantly altered by the buffer composition.

Referring to several investigations and simulations by other research groups [30, 33, 116] and the experimental results presented in this thesis, the strong decay in the electric properties of the solar cells with buffer layer compositions close to stoichiometric In_2S_3 could be explained by an appearance of a negative offset in the conduction band's alignment at the absorber-buffer-interface.

Following this assumption, the interface should either have a flat transition in the conduction band alignment or a small spike (i. e. 0.05 – 0.10 eV higher in the buffer than in the absorber), for the favourable composition at an In-content of 42 at%. According to the literature [34, 36] the persistence of a spike is connected to an inversion of the absorber's surface from *p*- to *n*-type conduction. This means that the electronic location of the *pn*-junction is situated underneath the interface to the buffer layer. Hence, the junction is shifted away from the vast amount of defects that are expected at the absorbers surface due to its exposure to air after fabrication. This positive offset in the band structure can be reduced until it changes into a negative offset when the buffer's band gap decreases or if the Fermi level of the buffer is reduced [34, 35]. This leads to the effect that the induced type inversion disappears and the electron-hole-pairs recombine via the defects at the absorber buffer interface [36] (see also chapter 2.2.1).

Indeed, the characterization of the buffer layers on glass by spectroscopic ellipsometry in chapter 5.5.3 outlines an increase of the band gap towards stoichiometric In_2S_3, which should be beneficial for the band alignment. However, as it has been shown in the previous chapters and as it was discussed in the literature review, the enhanced Cu diffusion into the buffer layer leads to a reduction of the buffer's band gap in the solar cell [74]. Furthermore, it has been reported that the introduction of Cu into In_xS_y causes a reduction of the charge carrier density inside the buffer layer [44]. Therefore, an abolishment of the type inversion could be caused.

Starting from an In-content of 42 at% towards the In-richer side, it is already obvious from the evolution of the band gap of pure In_xS_y films (Fig. 27) that its width decreases. Conclusively, this observation has to be connected to an increased absorption of

light in the buffer region and hence a reduction in the solar cell's current density [34]. According to Barreau et al. [55] the orbitals of the sulphur atoms in In_2S_3 form the top of the valence band. A lowering of the buffer's S/In ratio is therefore expected to reduce the distance of the valence band to the Fermi level and to be not relevant for the conduction band alignment. Furthermore, it has been reported that a lack of sulphur relative to the In_2S_3 composition enhances the charge carrier density and therefore the *n*-type characteristic of the thin film [44, 54]. Hence, the situation should be beneficial for the desired band alignment, since the distance of the conduction band to the Fermi level should be reduced [34]. However, one has to take into account that the results of Raman spectroscopy in chapter 5.2 indicate a growing fraction of In_6S_7 and InS when increasing the film's In-content. These additional phases have been reported to feature different transport properties: As it has been discussed in chapter 2.3.2, In_6S_7 does either show *p*-type conductivity [62] or an *n*-type with a very low electron density [58]. InS has been reported to be *n*-conductive with lower electron densities than In_2S_3 [50, 64]. Hence, one can assume that increasing fractions of In-rich phases inside the film lower the charge carrier density in the buffer layer. This has the effect of a reduced band bending and with this an abolishment of the type inversion of the absorber [34, 113]. Conclusively, the fraction of interface recombination is enhanced again, which can explain the deterioration of the electrical parameters (V_{oc} and *FF*) of the solar cells with increasing In-contents.

5.6.3 Photoconductivity and effects on the series resistance

In the previous chapter it has been shown that the series resistance of the solar cell is dependent on the S/In ratio of the buffer layer. This observation can be explained by a varying photoconductivity of the In_xS_y thin film or, alternatively, by the appearance of an offset in the conduction band at the buffer-absorber-interface. In an ideal solar cell, the illuminated diode characteristic is a copy of the dark diode characteristic (DDC) shifted by the short current density. This means that the IDC and the DDC should not cross in their respective graphs. However, while evaluating the characteristics of solar cells with different buffer compositions it became obvious that several graphs do show an intersection at certain voltages, which is usually also referred to as cross over. To illustrate this, Fig. 32 shows four examples with both diode characteristics of solar cells with different buffer compositions.

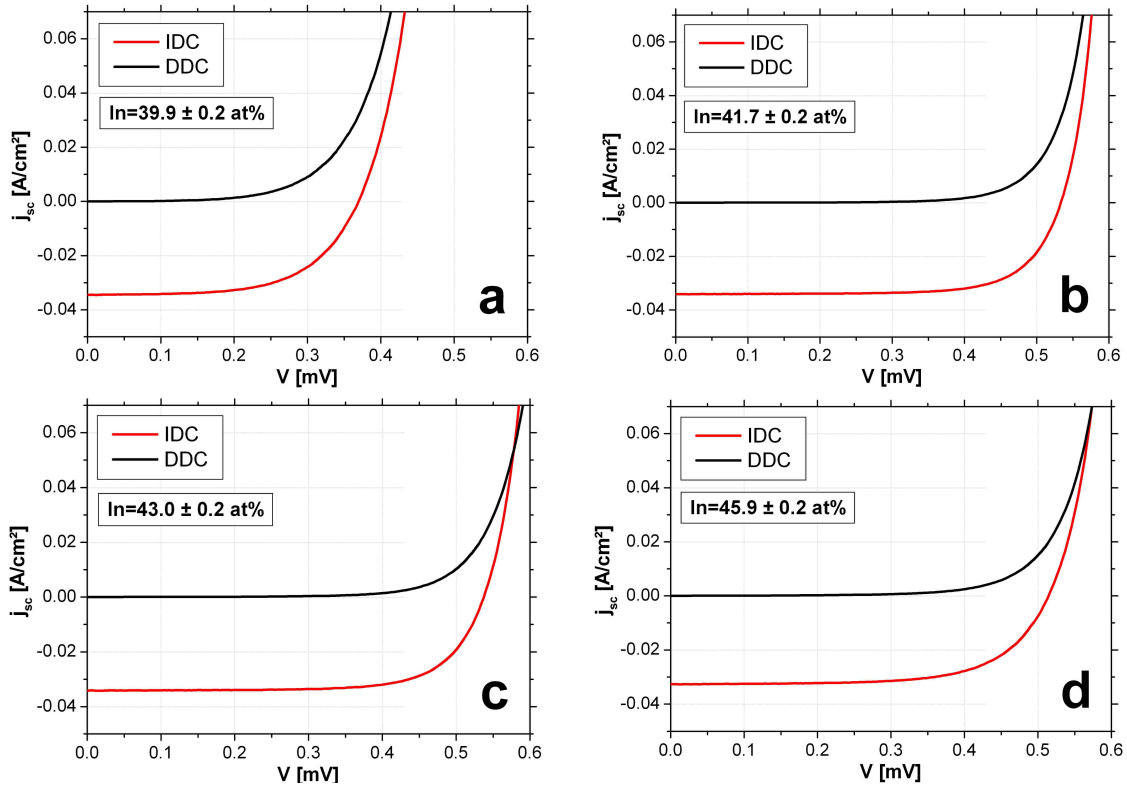

Fig. 32: Illuminated and dark diode characteristics of four solar cells with different buffer compositions.

The *jV*-characteristics have been recorded with a limitation of a maximum current flow of 100 mA in forward direction to avoid a damaging of the solar cell. Hence, the evaluable range is limited to the depicted scale. However, from the comparison of the graphs, one can assume that the appearance and the magnitude of the cross over might be dependent on the S/In ratio of the buffer layer. To quantify this observation over the varied range of the buffer composition, the distance of the respective intersection to the open circuit voltage has been computed for all cells discussed in the previous chapter. This means that large contributions of photoconductivity will yield a small value for the calculated distance. For the cases where no cross over occurs in the recorded range, the distance has been set to zero. The obtained values are plotted over the buffer's In-content in Fig. 33.

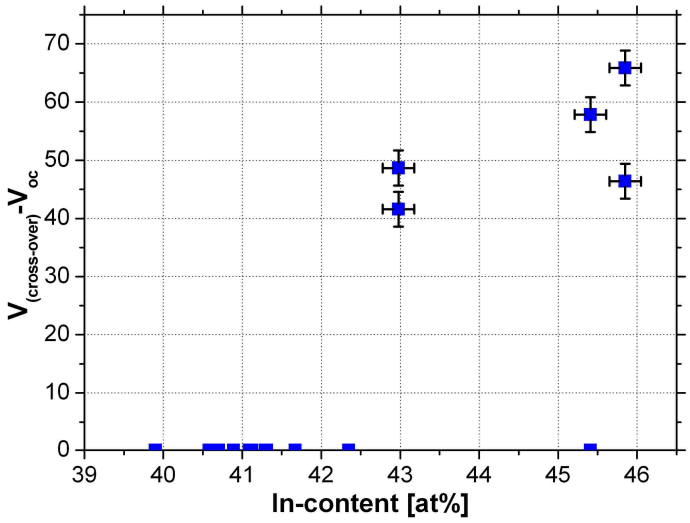

Fig. 33: Distance of the appearing cross over of the dark and illuminated diode characteristic from the open circuit voltage in dependence of the buffer's In-content.

With respect to the earlier hypothesis of a possible impact of the buffer's photoconductivity on the series resistance of the solar cell, one can deduce that the calculated distance does not correlate with the observed dependency in Fig. 30 (b). According to Fig. 33, the effect of a cross-over occurs more often towards In-contents of about 43 at%. According to Pudov [30] the appearance of a cross-over requires the existence of a secondary barrier in the conduction band. Conclusively, the observation that no cross-over is observed up to an In-content of about 43 at% supports the hypothesis of a rather flat alignment in the conduction band at an In-content of 42 at% and a cliff situation for lower In-contents. For the case of an In-content above 43 at%, at least a small spike has to be present in the conduction band at the buffer-absorber-interface. Thus, the considerations in the literature [55] of a predominant effectiveness of a sulphur deficiency on the valence band is confirmed.

Referring back to the evolution of the series resistance, an assignment to the appearance of a negative conduction band offset for low In-contents becomes likely. As discussed in more detail by Malmström [118] a cliff situation can lead to interface recombination, while the *FF* is both indirectly affected by a drop in V_{oc} and by an increasing ideality factor, which is consistent with the experimental results in Fig. 28 (V_{oc}) and Fig. 31 (ideality factor) and can also explain the increasing series resistance for lower In-contents in Fig. 30 (b). The increase in series resistance at higher In-contents is partly related with the appearance of a spike in the conduction band [30]. However, as it has been discussed above, the increasing fraction of In_6S_7 and InS can lead to lower net charge

carrier density in the buffer. Hence, a contribution to the evolution of the series resistance towards higher In-contents by the higher amounts of In-rich phases is also plausible.

5.7 External quantum efficiency

From Fig. 29 (b) it is known that the short circuit current density shows a slight dependency on the buffer's composition. Hence, it is of special interest in which wavelength region a limitation of this parameter becomes evident. Knowing about the cause of this limitation can lead to ideas of how to optimize the thin film stack towards higher conversion efficiencies. As it has been outlined in chapter 3.2, a characterization of solar cells in their external quantum efficiency (EQE) is capable to describe the wavelength resolved contribution of photons to the total current density. Since the previous chapters already outlined that the buffer's band gap depends on the respective S/In ratio, an analysis with a respective variation has been conducted. The EQE of several solar cells on equivalent absorbers have been determined in collaboration with the group of Prof. Dr. Ronning at the University of Jena [119] and are compared in Fig. 34.

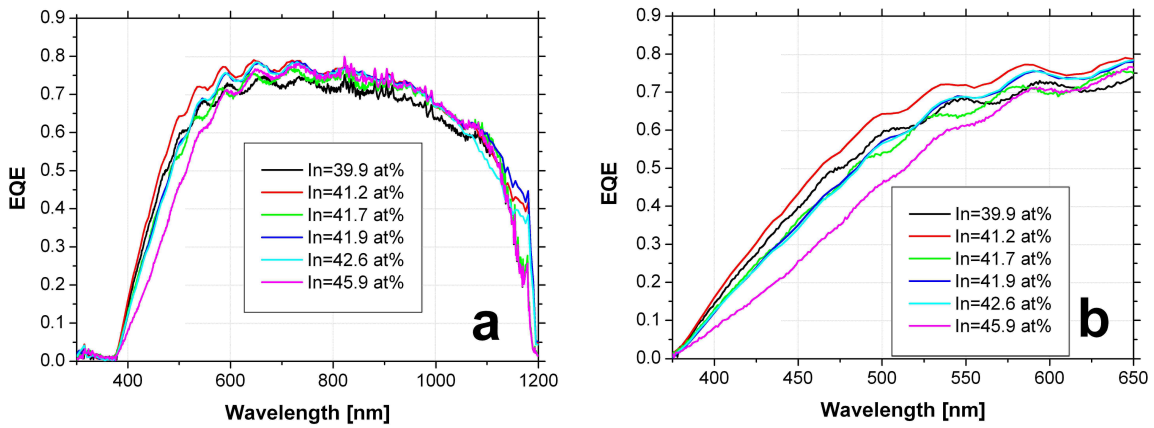

Fig. 34: Comparison of the EQE of several solar cells with different S/In ratios (a) of their buffer layer with a magnification (b) of the spectral range near the band gap (Statistical error of In-contents equals ± 0.2 at%).

From the EQE measurements, some variation in the maximum quantum efficiency can be seen in the wavelength range of about 600 nm to 1000 nm. Part of this can be associated to the increasing absorption of the buffer layer, as it can be concluded from the extinction coefficients in Fig. 26. However, this spectral range is also affected by other influences such as variations in thickness and the optical quality of the ZnO layers. Since the *n*ZnO layer has a thickness of 1200 nm several interference fringes are superimposed in the respective wavelength region.

A comparison of the wavelength region below 600 nm shows that the onset of absorption is consistent with the evolution of the band gaps in Fig. 27, determined by spectroscopic ellipsometry. Furthermore, it becomes obvious that a variation in the range of 41.7 ± 0.2 at% to 42.6 ± 0.2 at% does not show a significant effect in this context. This can be related to the only small variation in the band gap of about 0.1 eV in the respective range and to uncertainties in the measurement. Moreover, this behaviour is consistent to the evolution of the solar cells short circuit current densities with the In-content of the buffer, plotted in Fig. 29 (b).

However, the solar cell with an In-content of 39.9 ± 0.2 at% in the buffer layer clearly shows a reduced EQE compared to the one with an In-content of 41.2 ± 0.2 at%. In contrary to this finding, the EQE referring to the In-content of 39.9 ± 0.2 at% should feature higher values since its band gap is larger (see also Fig. 27). The fact that this is not observed reconfirms the result of the ToF-SIMS and HR-TEM measurements, where an enhanced Cu diffusion has been found for buffer layers close to the nominal stoichiometry of In_2S_3. As a result of the increased Cu diffusion the band gap is significantly lowered as it has already been mentioned in chapter 2.3.3 [74]. Therefore, this observation supports the above stated model, during which the Cu diffusion can induce a negative conduction band offset, which is responsible for the strong decay in efficiency for stoichiometric In_2S_3 buffer layers.

Unfortunately, an evaluation at higher wavelengths beyond 1100 nm cannot be conducted since the calibration in the measurement setup with an Si reference sample was not reliable in this region.

5.8 Summarizing discussion and conclusions

This chapter demonstrated that the S/In ratio has a significant effect on the structural and optical properties of the deposited In_xS_y buffer layers. In the first place this has been shown to be the case for thin films on glass. It has been found that an increasing In-content results in a growing fraction of In_6S_7 and InS phases inside the film. This leads to a reduced crystallinity, since the simultaneous presence of phases with different crystal structures impedes the grain growth during the deposition. The observation has been confirmed by HR-TEM measurements of the buffer's cross-section, where a reduced average grain size has been found for In-rich compositions compared to the situation close to the nominal stoichiometry of In_2S_3. Furthermore, the more fine crystalline nature has been associated to

be responsible for an impeded diffusion of Cu from the absorber into the buffer. A verification of this hypothesis has been done by ToF-SIMS analysis, during which a compositional profile has been recorded through the buffer into the upper part of the absorber. In addition to the enhanced Cu diffusion for buffer layers, with an In-content close to 40 at%, an accumulation of Na at the absorber-buffer-interface has been determined for all analysed samples. The diffusion of Na into the buffer layer has also been found to be increased for the nominal composition of In_2S_3. A quantification and confirmation of the enhanced Cu-diffusion was done by STEM-EDX measurements on cross-sections of the buffer layer inside the solar cell, however, the Na-content was below the detection limit of about 1 at%.

Referring to the optical properties of In_xS_y buffer layers on glass, an In-content of 40.5 ± 0.2 at% has been found to be a crucial value for the characteristics of the thin film. Below this value, the refractive index shows a normal dispersion and a band gap of about 2.0 eV. The evolution of the extinction coefficient indicates a transition close to a direct nature. Above an In-content of 40.5 ± 0.2 at%, the band gap is clearly indirect in its nature, while the width drops at 40.5 at% to about 1.8 eV and decreases linearly towards higher In-contents. This behaviour can be explained by the transition from a tetragonal structure to a cubic one in the respective phase diagram [42]. Furthermore, the extinction coefficient indicates a soaring absorption in the photon energy region above 2.5 eV, which is connected to an increasing anomalous character of the refractive index.

The S/In ratio of the In_xS_y buffer layer also has a significant effect on the electrical properties of solar cells. Both open circuit voltage and fill factor have been found to be strongly reduced when the buffer is deposited with an S/In ratio of 3/2. With respect to the highest conversion efficiency, an optimum composition has been found at an In-content of about 42 at%. Increasing the In-content to even higher values, another deterioration of the electrical properties is found. The short circuit current density does not show a strong dependence on the S/In ratio within a relatively broad range. However, very high In-contents result in enhanced light absorption inside the buffer layer and hence to reduced current densities.

An explanation of this behaviour is given by an interpretation of the solar cells secondary parameters in connection with the identified structural, optical and electrical characteristics of the buffer layers. To illustrate the proposed model, Fig. 35 shows a qualitative sketch of the changes in the band alignment when the In_xS_y buffer is either deposited close to the stoichiometry of In_2S_3 or with a higher In-content of about 42 at%.

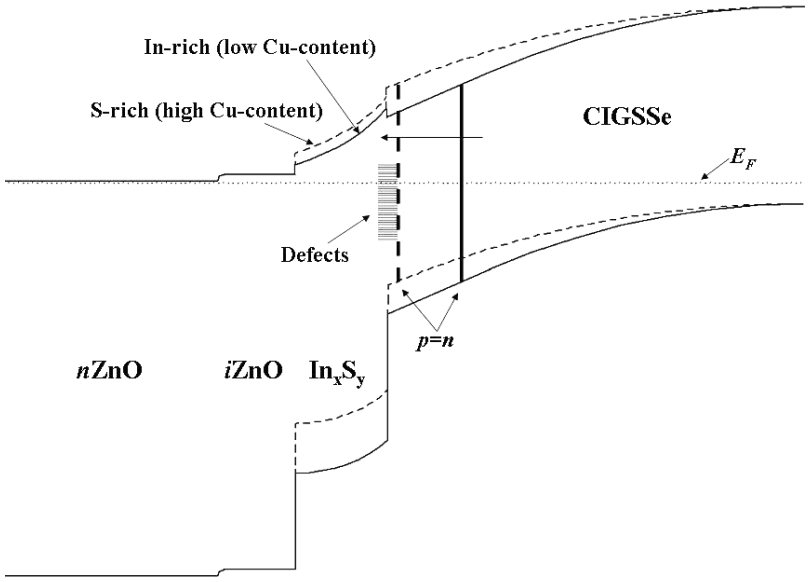

Fig. 35: Qualitative sketch of the band diagram and alignment at the absorber-buffer-interface for an In-rich (solid lines) and a S-rich (dashed lines) In_xS_y buffer in a CIGSSe solar cell.

In case of an In-content around 42 at% (solid lines in Fig. 35) the Cu-diffusion is impeded by the fine crystalline structure of the buffer layer. Here, the position of the Fermi level in the buffer and the width of the band gap in connection with the properties of the absorber allow a slight inversion of the absorber's surface. This is indicated by the position of the vertical solid line, labelled as *p=n*. At this location, the amount of holes equals the amount of electrons available for a possible recombination [34]. However, since there is only a limited amount of defects present at this location, the actual recombination of the charge carriers is reduced.

The introduction of Cu into the buffer layer reduces the width of the band gap [74]. Besides this effect, it has also been discussed that the Cu inside In_xS_y mainly affects the position of the valence band and reduces the *n*-character of the buffer layer [44]. This means that the density of the majority charge carriers in the buffer layer is lowered. Hence, the distance of the Fermi level to the conduction band increases, while the band bending on the absorber side is reduced. The combination of these changes results in a negative conduction band offset at the absorber-buffer-interface, which is depicted as the dashed situation in Fig. 35. This evolution shifts the position, where *p* equals *n* to the direct vicinity of the defects at the respective interface and with this to a significantly increased amount of interface recombination and a deterioration of the electrical properties of the solar cell [34-36].

For In-contents higher than 42 at%, the reason for the observed decreasing fill factor and open circuit voltage is similar. According to the literature, a sulphur deficiency in the

β-In_2S_3 phase mainly has an impact on the valence band maximum [55] and increases the charge carrier density [54]. However, as it has been outlined above, the thin films prepared within this thesis consist of several phases when the In-content is increased. Hence, the impact of the additional phases also has to be taken into account. In_6S_7 has been controversially reported to be a *p*-type semiconductor with a hole density of $7.4*10^{13}$ cm^{-3} by Al-Orainy et al. [62], while Gamal et al. [58] determined this phase to be of *n*-character with an electron density of $5.7*10^{8}$ cm^{-3}. However, the latter study also mentioned the possibility of contributions of both holes and electrons to the total conductivity. The InS-phase has been reported to be *n*-conductive with an electron density in the range of 10^{18} cm^{-3} [50] to 10^{15} cm^{-3} [60]. Referring to the reference value for the electron density of about 10^{18} cm^{-3} for sulphur deficient β-In_2S_3 [54], a reduction of this value can be assumed for increasing fractions of In_6S_7 and InS inside the complete thin film. As a result, the Fermi level of the buffer has to decrease, which also reduces the band bending from the absorber to the buffer [113]. Hence, the spatial distance of the *pn*-junction to the interface defects is reduced and the fraction of interface recombination increases again [34-36]. As it can be withdrawn from Fig. 33, a cross-over of the dark and the illuminated diode characteristic is still present at an In-content of 45.9 at%. Conclusively, a positive conduction band offset still has to be present at the absorber-buffer-interface [30]. This means that the rate of increasing interface recombination is slower for the case of an In-content above 42 at% than below this value. Therefore, the dependency of the solar cells efficiency of the buffer's In-content can be explained by the evolution of the electron density in the buffer layer. Obviously, an increasing Cu-content in the buffer layer has a stronger effect on the transport properties than an increase in In-richer phases. Hence, the conversion efficiency experiences a stronger decay from the optimum composition to the S-rich side than to the In-rich side, as it has been observed experimentally.

6 Doping of indium sulphide with sodium sulphide

Throughout the previous chapters it has been seen that In_2S_3 films can in principle be used as alternative to CdS buffer layers in CIGSSe solar cells. However, it is also obvious that a significant gap between conversion efficiencies of solar cells with CdS and In_xS_y buffers remains unclosed. Since it is not desirable to lose any of the high efficiency potential of CIGSSe by a replacement of the Cd containing layer, it is of high importance to close the mentioned efficiency gap. In the literature review in chapter 2.3.3 some approaches have already been outlined. Furthermore, the effects of the incorporation of third elements on the optical and electronic properties of the In_xS_y buffer layers have been discussed. In this context, the results of several experiments have proven that the use of Na_2S as doping material has a beneficial effect in combination with the CIGSSe absorbers used for the work on this thesis. The following chapters will discuss the characterization results of these layers and solar modules. In this work, both the Na/In and the S/In ratio have been varied since it is already known from the previous chapters that the S/In ratio in undoped buffer layers has a significant effect. The optimization of indium sulphide buffer layers for CIGSSe solar cells by this approach has been submitted for patenting [120].

6.1 Coevaporation of indium sulphide and sodium sulphide

6.1.1 Sodium sulphide as source material

The choice of Na_2S as doping material has become apparent, since this compound does not entail a fourth element in the resulting buffer layer. This has been assumed to be undesirable since a possible additional effect of a fourth element cannot be separated during the doping process.

Referring to the requirement of an elemental purity of 99.999 % for the In_2S_3 source material (compare chapter 4.3), it is also obvious that a contamination with additional elements besides Na should be avoided. Since a source of supply, being capable to deliver the same purity as for In_2S_3, could not be found, a purity of 99.99 % was used for the Na_2S source material. Taking into account that the added quantity of doping material lies far below the amount of In_2S_3, this impurity level has been assumed to be acceptable. Due to the distinct hygroscopic nature of Na_2S, the compound has only been available as nonahydrate ($Na_2S{:}9H_2O$). However, this did not lead to problems since the H_2O molecules

are released by the compound during evacuation of the process chamber and subsequent heating of the material.

6.1.2 The simultaneous deposition of sodium sulphide and indium sulphide

From the aspect of the process control, one of the main advantages of using In_2S_3 as buffer material is the dry, vacuum based technology. Hence, it was self-evident to rely on the experience gained during the evaporation of In_2S_3 and focus on the development of a process that allows a coevaporation of In_2S_3 and Na_2S. Therefore, the vacuum chamber has been equipped with a second effusion cell. Due to geometrical reasons inside the chamber, it was not possible to align the two sources onto one focal point. Instead, the sources were arranged in such a way that they were situated on opposite sides of the chamber underneath the substrate holder. A respective sketch of the arrangement inside the chamber is shown in Fig. 36.

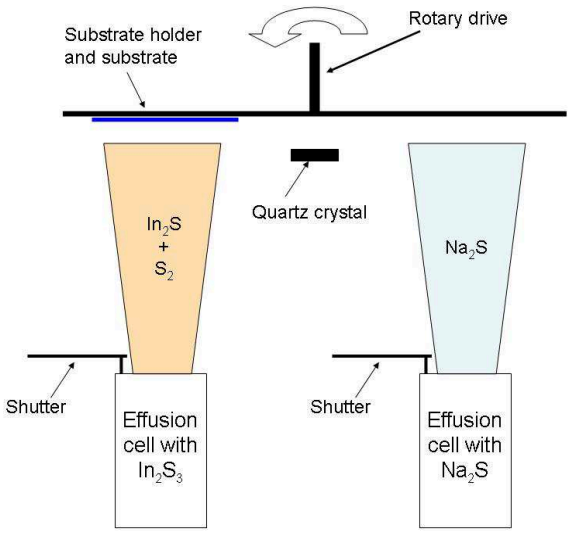

Fig. 36: Sketch of the arrangement of the In_2S_3 and the Na_2S source inside the vacuum chamber.

Thus, the preparation of $NaIn_xS_y$ films did not occur in a proper simultaneous deposition, but can be regarded as a stack of many thin layers of In_xS_y and Na_2S. However, since a deposition process of about 45 nm includes up to 80 rotations over the sources, the intermixing of the components is regarded to be sufficient enough to be comparable to a classical coevaporation. Since the evaporation rates of both In_2S_3 and Na_2S depend on their temperatures, a variation of the In_xS_y/Na_2S ratio in the films has been achieved by an adjustment of the respective effusion cell temperatures.

6.1.3 Process control and determination of the Na-content inside indium sulphide thin films

As initially no calibration for the Na-containing In_xS_y films existed for the XRF tool, it was necessary to develop a method to quantify the amount of Na_2S introduced into the films. Nevertheless, it was already possible to determine the individual evaporation rates of the sources via a quartz crystal by closing the shutter of the respective other effusion cell (see Fig. 36). Thus, it has been chosen to evaluate the increase in film thickness caused by the addition of Na_2S in dependence on the ratio of the deposition rates, as recorded by the quartz crystal. The film thicknesses themselves have been determined by spectroscopic ellipsometry on reference samples. This allowed the generation of a parameter, being independent of the geometrical situation inside the chamber and can be reproduced in other deposition systems. Subsequently to the determination of the process window, three samples have been characterized by RBS measurements in the respective range. Based on the obtained composition information, the XRF system has been calibrated for depositions on crystalline Si wafers. The utilization of Si wafers instead of SLG as substrate is necessary since the Na-content in the SLG would falsify the result of an XRF measurement. The particular correlations of the thickness ratio from ellipsometry to the evaporation rate ratio from the quartz crystal measurement and the Na/In ratio from RBS characterization are shown in Fig. 37. At this point, it has to be stated that the RBS measurements also found a significant amount of oxygen inside the analysed thin films. This can be attributed to the strong hygroscopic nature of Na_2S. However, since the amount of oxygen inside the film is assumed to be dependent on the film's exposition time to air, it can not be regarded as representative for the buffer layer deposited on top of the CIGSSe absorber. To limit this influence, the samples have to be characterized as soon as possible after the deposition. Referring to the evaluation of the XRF measurements, the oxygen content has not been taken into account.

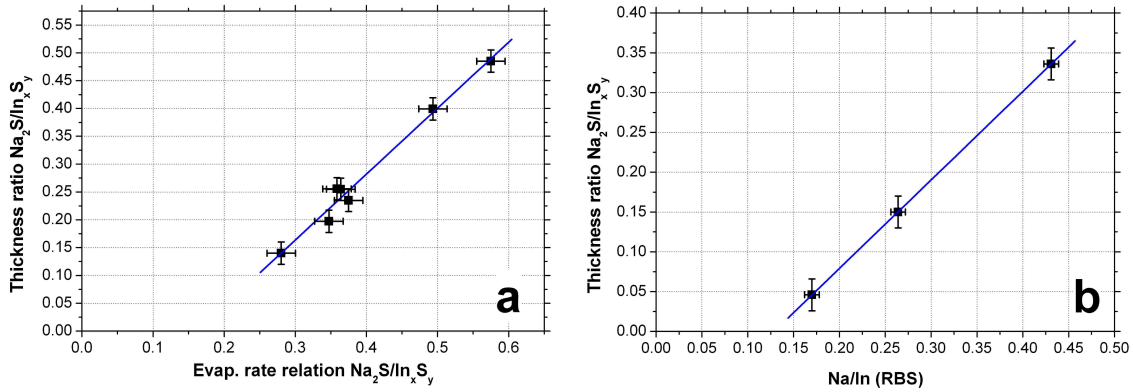

Fig. 37: Thickness ratio of Na_2S/In_xS_y in dependence of the respective evaporation rate ratio (a) and the correlation to the quantification of Na/In by RBS (b) (Uncertainty for Na/In ratio represents the absolute error of the RBS measurement (~0.01)).

From the linear regression line in Fig. 37 (a) one can conclude that the thickness ratio of the complete stack is in good correlation to the recorded evaporation rates. However, it becomes obvious that the regression line does not intercept the origin of the coordinate system. This behaviour is also observed in the correlation vs. the Na/In ratio determined by RBS. An extrapolation of the correlation in Fig. 37 (b) results in a Na/In ratio of 0.13 ± 0.02 for the intercept with the X-axis. The same evaluation can be done for the thickness ratio vs. the S/In ratio, leading to a respective value of S/In=1.45 ± 0.06. The Na-content for the intercept can hence be calculated to 5.0 ± 0.8 at%.

As it has been discussed in chapter 2.3.3, Barreau et al. [72] also reported an upper limit of 5.0 at% (Na/In=0.13) for the Na incorporation into the lattice of thin film In_xS_y. It has been shown that the lattice parameter increases while raising the Na-content from 0 at% to 5 at%, however, an effect on the thickness of the layers has not been evaluated. Referring to those results, it can be concluded that an introduction of 5.0 at% of Na into the In_xS_y lattice in the present case is very likely. Beyond this limit the Na_2S is incorporated in a different way. However, a detailed analysis of how the excess Na_2S is bound inside the thin films could not be completed within the scope of this thesis. Nevertheless, it can be noted that the Na-content of all deposited films lies above the stated limit of Barreau [72].

6.2 *Structural and compositional properties of the buffer layers in dependence of the Na_2S content*

6.2.1 Raman analysis of sodium containing indium sulphide thin films

In the previous chapters it has been outlined that the structure of the grown films can hamper the diffusion of Cu from the absorber into the In_xS_y layer and thus prevent a reduction of the buffers band gap and carrier density. Therefore, it is of special interest how the thin films grow on the absorber and on reference samples. Since Raman spectroscopy has already proven to be capable to characterize structural changes caused by an alteration of the S/In ratio, the Na_2S-containing films were analysed accordingly. Referring to the depositions performed for the calibration of the XRF tool, SLG has been coated in addition to the Si wafers for the RBS measurements. Hence, the composition of the $NaIn_xS_y$ layers on the glass substrates are well known and can be compared to the films that have been processed without the addition of Na_2S. All depositions have been performed without a pre-heating step of the substrates. Therefore, a diffusion of sodium from the glass into the films is expected to be negligible. The effect of an increasing Na_2S content in In_xS_y layers on the respective Raman spectra is depicted in Fig. 38. Consistent with the evaluation described in chapter 5.2, a linear baseline was subtracted from all spectra.

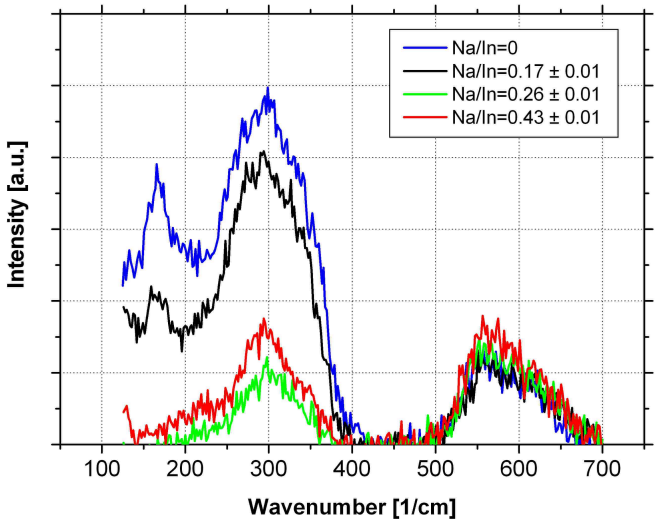

Fig. 38: Raman spectra of Na containing In_xS_y buffer layers on SLG as a function of composition (Uncertainty for Na/In ratio represents the absolute error of RBS measurements).

The reference sample, not containing any Na, shows a spectrum of an In_xS_y film with distinct contents of In_6S_7 and InS, indicated by the enhanced intensity in the wavenumber region of 125 cm^{-1} to 200 cm^{-1} (see also chapter 5.2). As it can be deduced from the spectra with increasing Na/In ratios, an increasing Na-content reduces the proportion of these phases inside the film. This behaviour can be understood considering

the fact that the increasing amount of sodium is connected with an increase in sulphur at the same time, as Na_2S is added. The additional sulphur obviously hampers the formation of such In-rich phases and suppresses them completely when sufficient sulphur is present. Nevertheless, it can be concluded that the crystallinity of the films does not increase as no distinct Raman bands arise for any composition. This is supported by XRD measurements for several depositions on Si wafers, which will be discussed in chapter 6.4.1. The persistent fine crystallinity can be explained since the lattice of In_2S_3 is only capable of incorporating sodium up to a Na/In ratio of 0.13 [72], as it has been outlined in the previous chapter. Due to the fact that all depositions feature a Na/In-ratio beyond this value, the respective lattice is expected to be oversaturated with Na, leading to a reduction of the crystallization as it has been seen for undoped In_xS_y films. Referring to the blocking behaviour for diffusion of the more fine crystalline In_xS_y, when deposited In-rich, this can be interpreted as beneficial since the fine crystalline structure should also hamper the diffusion of Cu from the absorber into the buffer layer.

6.2.2 ToF-SIMS analysis of Na containing indium sulphide films on absorber layers

As already shown in chapter 5.3, ToF-SIMS analysis is capable of giving insights in the diffusion of absorber elements into the buffer layer. Since this topic has already been identified to be crucial for the electrical properties of solar cells, four samples with different buffer compositions have been chosen for ToF-SIMS analysis. In order to be able to compare the results to the standard In_xS_y buffer layers, one of the analysed solar cells buffer layer was undoped. The ZnO front electrode has been removed by wet chemical etching as it has been done for the samples in the previous chapter. It was again possible to sputter slowly through the buffer layer into the absorber and to obtain detailed compositional information on the respective layer. A comparison of the obtained Cu profiles (a) together with a magnification of the buffer area (b) is shown in Fig. 39. The respective Na-distribution is depicted in Fig. 40. The Na/In ratios have been calculated from ellipsometer measurements via the regression line depicted in Fig. 37 (b) since no Si wafers have been deposited but only SLG as reference samples.

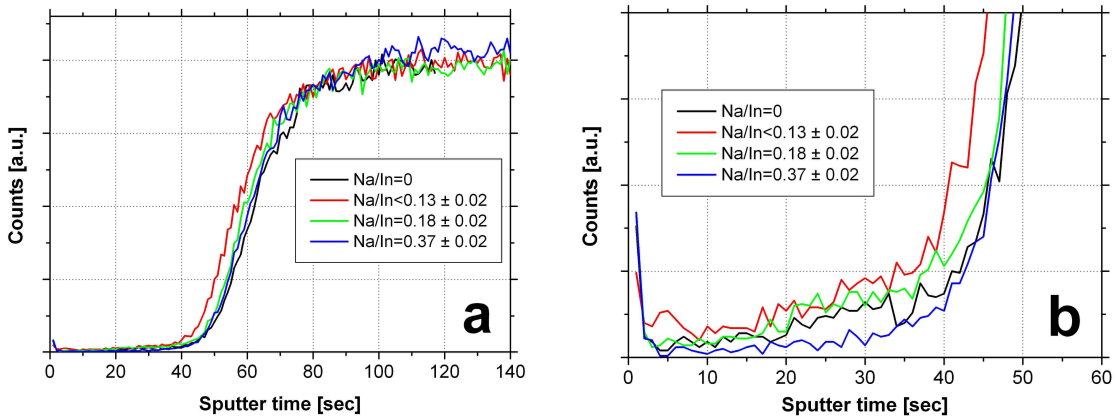

Fig. 39: ToF-SIMS profile of the Cu distribution inside doped In_xS_y buffer layers (a) together with a magnification of the buffer region (b).

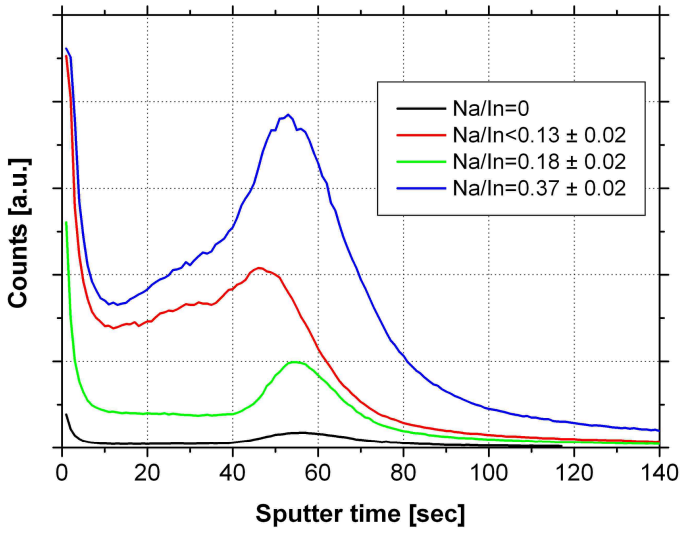

Fig. 40: ToF-SIMS profile of the Na distribution inside In_xS_y buffer layers that have been doped with different quantities of Na_2S.

From the Cu distribution in Fig. 39 (a) one can conclude that the absorber's surface has been reached after a sputter time of about 50 seconds, where the Cu content significantly increases. To verify whether and to which extent Cu has diffused into the buffer layer, Fig. 39 (b) shows a magnified view of the relevant profile. Since the reference sample (Na/In=0) has been coated with an In_xS_y layer, which featured an In-content of 41.8 ± 0.1 at%, only little Cu diffusion is expected at this point (see also chapter 5.3). Within the resolution of the measurements, no significant de- or increase can be observed for the buffer layers that have been doped with Na_2S. Solely, for the profile of the buffer layer, with a Na/In ratio of 0.37 ± 0.02, even less diffusion of Cu is detectable.

An overall increase in the intensity of the Na signal for increasing Na/In ratios can be deduced from Fig. 40. However, it can also be seen, that the order in the increasing intensity is swapped for the profiles of Na/In<0.13 ± 0.02 and Na/In=0.18 ± 0.02.

Unfortunately, it was not traceable whether the samples have been mixed up during the sample preparation or the analysis. According to the documented, adjusted evaporation rates of Na_2S and In_2S_3 the order should be the other way round, too. Since the expected gain in comprehension of a repetition of the analysis did not justify the additional expenses, it has been chosen not to repeat this experiment. Nevertheless, it is surprising that all profiles feature a distinct peak at the interface to the absorber. Since the evaporation rate of the Na_2S source has been kept constant during the processes, one would expect a flat profile through the buffer layer. Comparing this result to the distributions in the Na-contents for the undoped buffer layers in Fig. 19, it can be noted that an accumulation at the absorber-buffer-interface has been found in this case, too. Following Cadel et al. [121], Na can be found in a higher concentrations at grain boundaries of CIGSe absorbers than in the crystalline volume of grains. This observation has been confirmed by Cojocaru-Miredin et al. [122], who also suggested that Na has an important influence on the electrical properties of grain boundaries. As it has been mentioned previously, the absorber was exposed to air after the fabrication, leading to an increased amount of defects at the interface [36]. The combination of both arguments is hence likely the explanation for the accumulation of Na at the buffer-absorber-interface. A diffusion of Na could be induced by the *n*ZnO process, which is conducted at elevated substrate temperatures. Due to the increased defect density at the interface, a segregation of larger fractions of Na becomes plausible. Thus, a passivation of the interface defects by Na might be possible and in this case beneficial for the electrical properties of solar cells and modules since it reduces the amount of active recombination centres.

6.3 Optical properties of sodium containing indium sulphide films

In chapter 2.3.3 it has been discussed, that different institutions already characterized Na containing In_xS_y thin films and found an increasing band gap towards higher Na-contents [68, 73]. Since these investigations have also been made by transmission and reflection measurements, it was desirable to investigate the deposited layers by spectroscopic ellipsometry.

It has been found, that the utilization of two Tauc-Lorentz oscillators was also capable to describe the measured values of $\tan(\Psi)$ and $\cos(\Delta)$ for Na-containing films, like it was the case for pure In_xS_y layers. In order to obtain a good fit quality, the parameters of chapter 5.5.3 have been used as start values for the film with the lowest doping level. While

proceeding to higher Na-contents and using the parameters obtained before, a good fit quality was reached for all analysed thin films. The refractive indices and the extinction coefficients depicted in Fig. 41, correspond to the same samples, which have been analysed by Raman spectroscopy in chapter 6.2.1.

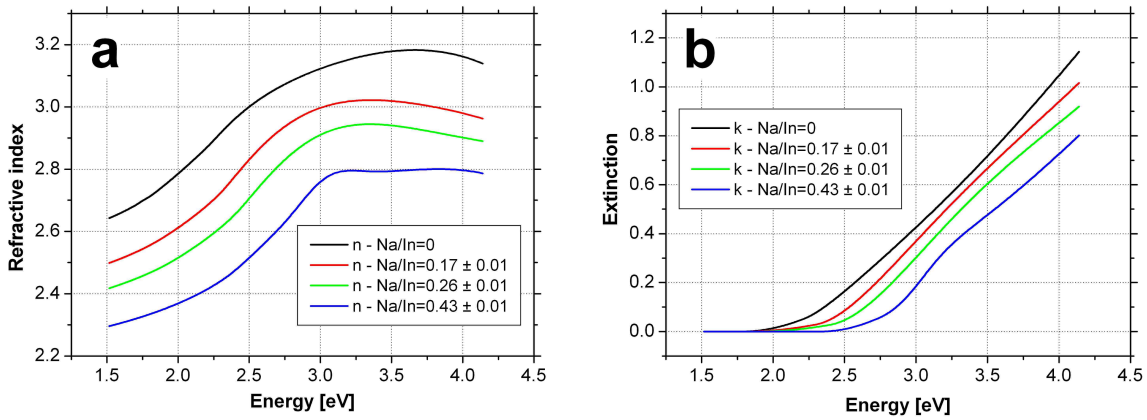

Fig. 41: Comparison of the refractive index (a) and the extinction coefficient (b) in dependence of the Na/In-ratio of Na containing In_xS_y films on SLG (Uncertainty of the Na/In ratio represents the absolute error out of RBS measurements).

The refractive index of the layers obviously decreases with increasing Na/In ratios. In the same way as it has been seen for the Na-free layers and higher In-contents, an anomalous dispersion partly arises for photon energies above about 3.3 eV, indicating a stronger absorption in this energy range [92]. The dependency of the extinction coefficient indicates that the width of the band gap increases towards higher Na-contents. However, in contrary to the literature this is the case for Na-contents above values of 5.0 at%. As it has already been discussed in the literature review (chapter 2.3.3), Barreau et al. [72, 73] reported an increase of the band gap from 2.1 eV to 3.0 eV for a variation of the Na-content in the range of 0 at% to 5 at% (Na/In=0.13). Above the content of 5 at% no further increase has been found. To compare these values with the ones of this study, Fig. 42 shows the evolution of the two band gaps obtained from the two Tauc-Lorentz oscillators.

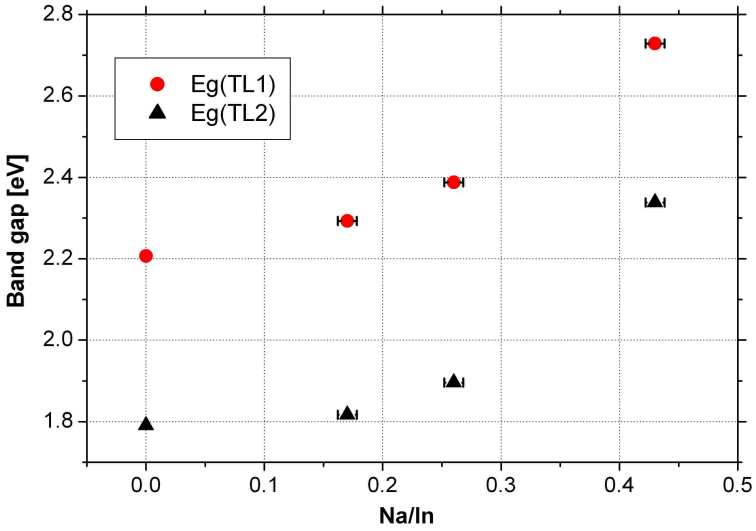

Fig. 42: Evolution of the band gaps of the two Tauc-Lorentz oscillators obtained by spectroscopic ellipsometry as a function of the films Na/In ratio (Standard deviation of five repetitive measurements on one sample equals ± 0.003 eV; uncertainty of the Na/In ratio represents the absolute error out of RBS measurements).

In the present case, the band gap increases from 1.8 eV to a value of 2.3 eV for the highest Na/In ratio. The discrepancy to the values of Barreau et al. [73] (direct transition with E_g=3.0 eV at Na/In=0.13) might be explainable by the fact that their layers have not been processed by coevaporation but by annealing of a stack of several In, S and NaF layers at 400 °C. Here any Na-content above 5.0 at% has been reported to have segregated at the surface of the layers and is no longer effective in the bulk of the thin films. Furthermore, the layers were reported to be free of fluorine after the annealing step. The films have been determined to have crystallized in a β-In_2S_3 structure and feature an increasing lattice parameter towards higher Na-contents by XRD measurements [72]. In contrast to this, the coevaporated films of the present study are fine crystalline as it has been found by Raman spectroscopy (see chapter 6.2.1) and will be discussed later in this thesis. Referring to the dependency of the optical properties of pure In_xS_y films, it already became obvious that the crystallinity has a significant influence on the width of the band gap. Especially, for the phase transition from α-In_2S_3 to β-In_2S_3 this has been found to be the case. Hence, it can be expected that the annealed samples from [72, 73] feature different optical properties than the ones shown here.

6.4 Optimisation of the Na/In and the S/In ratio in the buffer layer

6.4.1 Process variations and layer properties

During the earlier chapters it has already been outlined that the S/In ratio has an impact on the properties of the pure In_xS_y thin film itself and with this on the conversion efficiency of the respective solar cells. Conclusively, this ratio has to be taken into account for an optimisation of the buffer layer. Based on the possibilities of the equipment used to vary the S/In ratio, an experiment has been conducted during which both S/In and Na/In ratio has been varied. During this experiment the cooling shield temperature used to reduce the sulphur partial pressure has been varied in the applicable range at three different settings. The resulting Na/In and S/In ratio of the respective layers, as measured by XRF, are depicted in Fig. 43.

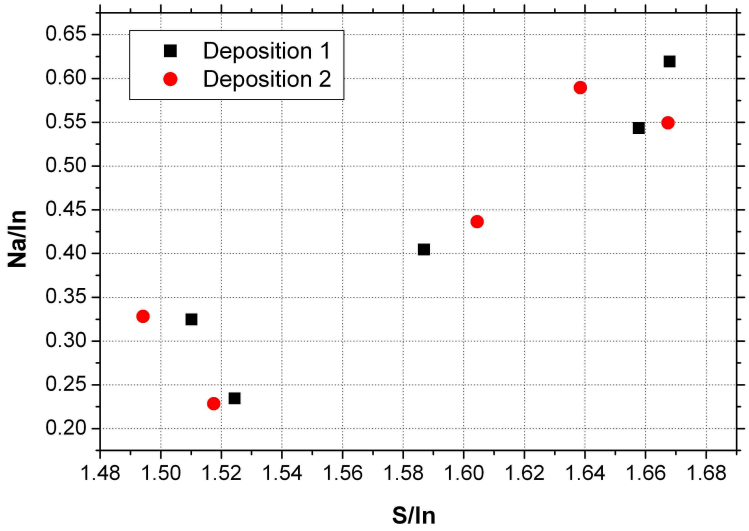

Fig. 43: Compositional variations in the Na/In and the S/In ratio for the conducted experiment (Standard deviations out of XRF measurements for Na/In and S/In equal ± 0.001 and ± 0.003 respectively).

The graph clearly shows that the S/In ratio is also strongly affected when the Na/In ratio is varied during the process. This becomes obvious when taking into account that the doping material is Na_2S. Any increase in the Na-content conclusively leads to a higher S-content. As a result a nearly linear dependency can be withdrawn from the plot, indicating that an alteration of the S/In ratio should be done with a different doping material.

Barreau et al. [67] concluded that the incorporated sodium occupies tetrahedral sites in crystalline β-In_2S_3 until the lattice is saturated and the $NaIn_5S_8$ compound is reached. However, as it has already been mentioned above, the Na-content inside the layers is significantly higher than stated in that publication. In order to obtain knowledge about the structure of the deposited layers, the films have been characterized by GI-XRD in the “as

deposited" situation on silicon wafers and on the CIGSSe-absorber layers. The respective GI-XRD spectra of the different $NaIn_xS_y$ films on Si wafers are shown in Fig. 44. The plot includes five composition combinations representing the five data pairs of Fig. 43 and one pure In_xS_y reference sample from the same experiment.

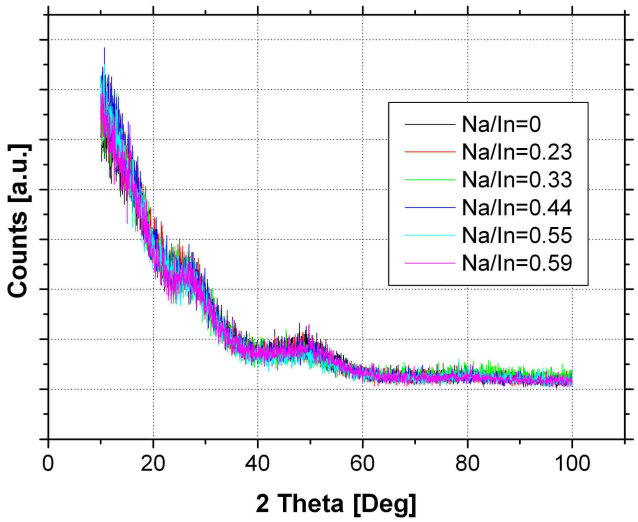

Fig. 44: Result of a GI-XRD analysis of the processed $NaIn_xS_y$ layers and a reference In_xS_y film on Si-wafers (Standard deviations out of XRF measurements for Na/In equals ± 0.001).

From the graph it can be deduced that all deposited layers do not show any designated diffraction peaks. Conclusively, this means that all films are either amorphous or have a fine crystalline structure, as it has already been discussed during the Raman analysis of the doped In_xS_y layers on glass in chapter 6.2.1. For the respective GI-XRD measurements of the equivalent films deposited on absorbers (not shown here), only reflexes of $CuInSe_2$ have been observed. This indicates that no significant difference for the obtained structure of the deposited $NaIn_xS_y$ occurs for the two different substrates. Referring to the hypothesis of the previous chapters that a fine crystalline structure impedes the diffusion of Cu from the absorber into the buffer, this situation should also be beneficial for the electrical properties of the solar cells.

In chapter 6.3 it has been mentioned that the band gap increases when Na_2S is added into the In_xS_y thin films. To verify this behaviour for the layers deposited during this experiment, the respective films have also been characterized by spectroscopic ellipsometry. The resulting band gaps of the two oscillators in the respective ellipsometer model are depicted in Fig. 45. Since the Na/In and the S/In ratio depend on each other and the S/In ratio only had a relatively small influence on the band gap in fine crystalline In_xS_y films, it has been chosen to plot the band gaps only versus the Na/In ratio.

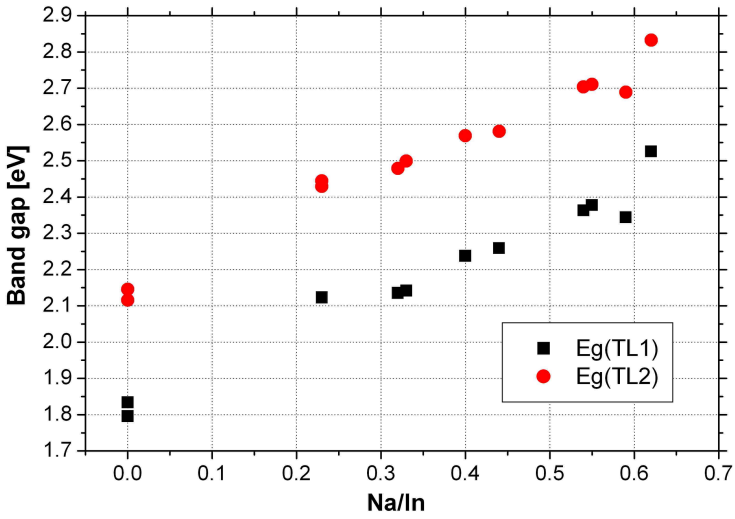

Fig. 45: Evolution of the band gaps of the $NaIn_xS_y$ and In_xS_y reference buffer layers in dependence of the Na/In ratio (Relative error for band gaps and Na/In ratios are in the range of ± 0.003 eV and ± 0.001 respectively).

The band gap increases from about 1.8 eV in case of the reference with no incorporation of Na, to a value of about 2.5 eV at a Na/In ratio of 0.62. The drop in the band gap at a Na/In ratio of about 0.59 correlates with a higher mean square error obtained during the fit procedure. However, the origin of this effect is not clear but might be associated to uncertainties in the process.

6.4.2 Main parameters of the *jV*-measurements

The experiment included a deposition of the buffer layers on top of 10x10 cm² absorber layers. These have gone through the further process steps described in chapter 2.1 and have been evaluated as modules regarding their *jV*-characteristics. To investigate their electrical properties in more detail, Fig. 46 shows a complete overview of the main parameters of the solar modules in dependence of both the Na/In and the S/In ratio, displayed in several scatter plots. The values of the main parameters of a reference sample with a CdS buffer are included as horizontal lines in each graph to outline the improvement achieved with this process variation.

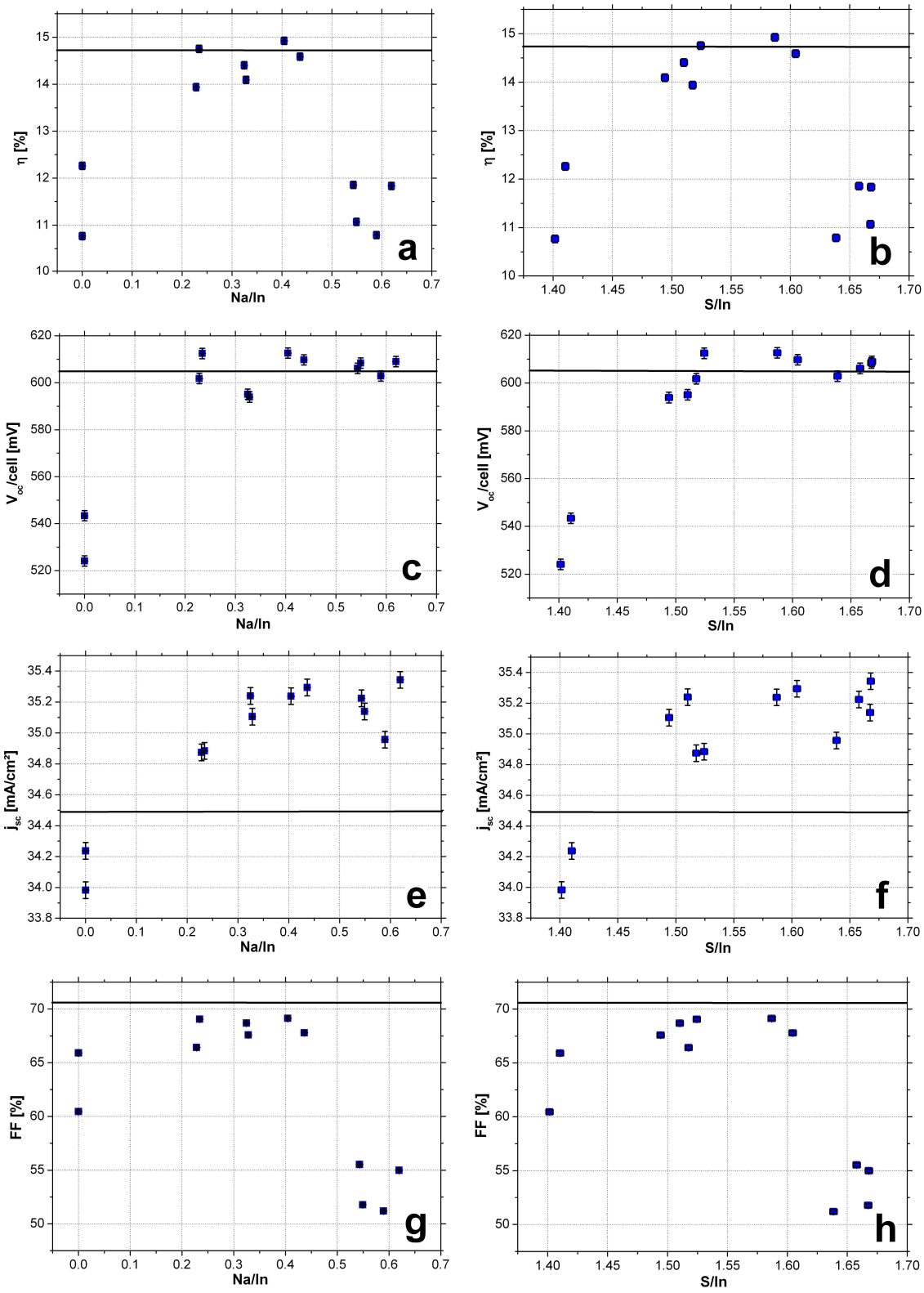

Fig. 46: Efficiency (a, b), open circuit voltage (c, d), short current density (e, f) and fill factor (g, h) of 10x10 cm² solar modules in dependence of the buffer's Na/In and S/in ratios together with the respective parameters of the best module with a CdS-buffer, indicated by a horizontal line (Error bars are partly smaller than symbols).

The graphs of the main parameters in dependence of the Na/In ratio show that the highest conversion efficiency of 14.9 ± 0.1 % can be reached at a Na/In ratio of 0.40.

However, in combination with the dependency of the S/In ratio it becomes obvious that the best parameter combination probably has not been included in this experiment: The evolutions indicate that the parameter combination with the highest potential is located at Na/In≈0.30 and S/In≈1.55. Especially the value of the open circuit voltage is expected to reach a higher value for the best case. Hence, one can expect that the combination of this parameter adjustment would result in an even higher efficiency for a respective solar module. For the CdS reference, the best 10x10 cm² module measured so far was used as benchmark.

Concerning the evolution of the main parameters, it can be deduced that both j_{sc} and V_{oc} show a drastic increase for higher Na/In ratios with respect to undoped buffer layers. As it has been outlined in the beginning of this chapter, the increase in current density can be associated to the reduced photon absorption in the buffer layer due to the larger width of the buffer's band gap. Increasing the Na/In (S/In) ratio to values higher than 0.50 (1.60), a reduction in j_{sc} can be observed. At this point the V_{oc} increase seems to be limited, neither showing a decay nor any further increase. From the evolution of the fill factor, some increase can also be seen when the buffer is doped with Na_2S. However, it features an even stronger decay when the Na/In ratio exceeds a value of 0.55.

Comparing the electrical properties of the modules with a $NaIn_xS_y$ buffer layer to the best one with a CdS buffer layer, it can be seen that the efficiency gap, mentioned in chapter 5.6.1, has been fully closed. The quantitative differences in the respective main parameters of the best solar modules are summarized in Table 6.

Table 6: Comparison of the main electrical parameters of the best solar modules, obtained with a $NaIn_xS_y$ and a CdS buffer layer.

Buffer	$NaIn_xS_y$	CdS
η (%)	14.9 ± 0.1	14.7 ± 0.1
V_{oc} (mV)	613 ± 2	605 ± 2
j_{sc} (mA/cm²)	35.2 ± 0.1	34.5 ± 0.1
FF (%)	69.1 ± 0.2	70.6 ± 0.2

The comparison outlines that the electrical parameters are nearly the same in their achieved electrical parameters. Both V_{oc} and j_{sc} have surpassed the module with the CdS buffer layer, while the *FF* is still higher for the latter one. In total the parameters result in a slightly higher efficiency for the module with the $NaIn_xS_y$ buffer.

Referring to the expected optimum composition of the buffer layer, it becomes obvious that the S/In ratio is close to the one of $NaIn_5S_8$ (S/In=1.60), which has already

been discussed by Barreau et al. [72, 73, 75] and Lafond et al. [68] (see also chapter 2.3.3). Besides the fact that the Na/In ratio of the buffer layers with the highest efficiencies are well above the one of $NaIn_5S_8$ (Na/In=0.20) the Na distribution of the SIMS measurements in Fig. 40 indicate that the composition is not homogeneous throughout the buffer layer. Therefore, it might be possible that the buffer's Na/In ratio approaches the one of the $NaIn_5S_8$ phase after the respective accumulation at the interface has levelled off. A detailed analysis regarding this analysis has to remain open for further investigations.

6.4.3 Secondary parameters and photoconductivity

In order to analyse the observations in more detail and to investigate the underlying reason for the high efficiency of the Cd-free solar module, the secondary parameters of the diode models have to be taken into account. Since both, S/In and Na/In ratio have been varied, the evaluation has to refer to both parameters. A compilation of the secondary parameters (saturation current density j_0, ideality factor n, shunt resistance R_{sh} and series resistance R_s) of the modules discussed above are depicted in Fig. 47 and Fig. 48 for both the dark diode characteristic (DDC) and the illuminated diode characteristic (IDC).

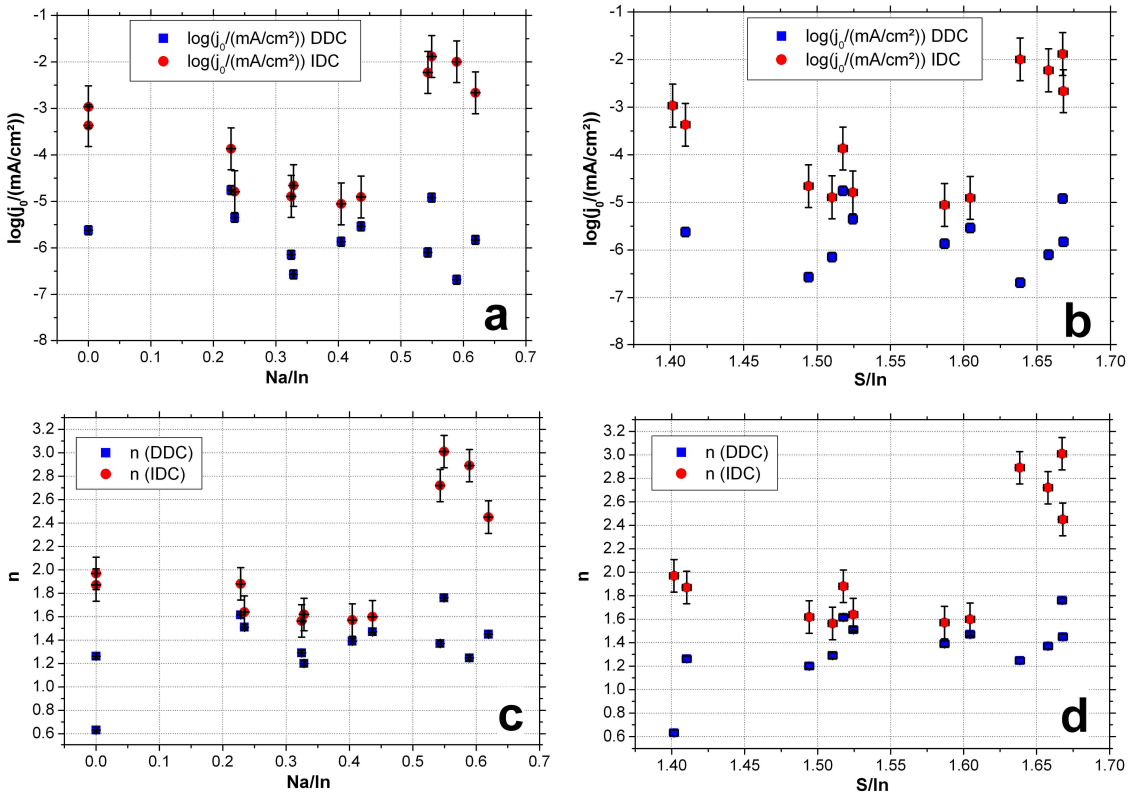

Fig. 47: Compilation of the secondary parameters saturation current density j_0 (a, b) and ideality factor n (c, d) as a function of the buffer's Na/In and S/In ratio (Error bars partly smaller than symbols).

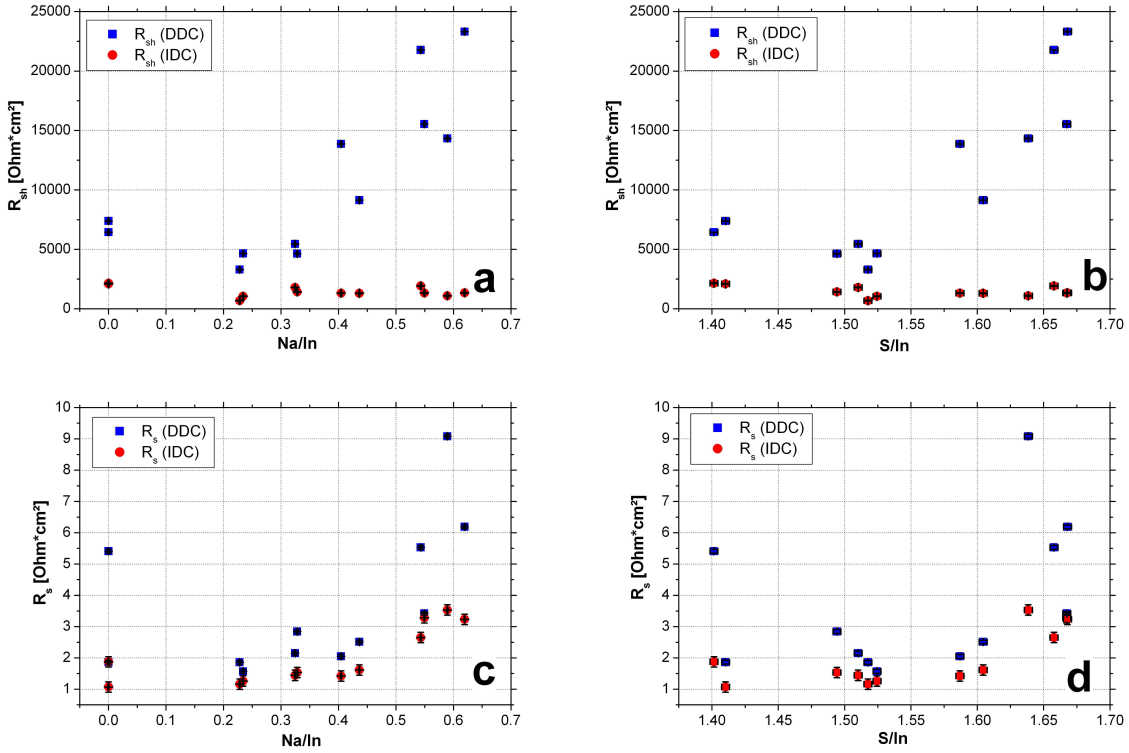

Fig. 48: Compilation of the secondary parameters shunt resistance R_{sh} (a, b) and series resistance R_s (c, d) as a function of the buffer's Na/In and S/In ratio (Error bars partly smaller than symbols)

For the saturation current density and the ideality factor one can observe a similar behaviour, where the parameters of the DDCs hardly show any variation throughout the varied range. However, referring to the values of the IDCs, both values are decreasing to their respective minimum, when proceeding from a Na/In (S/In) ratio of 0 to about 0.4 (1.40 to 1.60). Exceeding these ratios, a strong increase becomes obvious in both cases.

The data point with an ideality factor of 0.6 has to be regarded as outlier. The fit resulted in a saturation current density of about 10^{-11} mA/cm², which is not credible and might have interacted with the other secondary parameters during the fit procedure.

For the case of the DDCs, both the series and the shunt resistance also seem to maintain their values until a Na/In (S/In) ratio of about 0.45 (1.55) is reached and significantly increases when proceeding to higher doping levels. In case of the shunt resistance, the IDC's parameters are reduced and do not change throughout the varied range. However, comparing the series resistances of the IDCs to the ones of the DDCs, a reduced increase of the IDC's parameters towards higher Na/In (S/In) ratios becomes obvious. Referring to the data point with a series resistance of 5.4 Ohm*cm² at Na/In=0 (S/In=1.40), it can be mentioned that this one is connected to the outlier stated above and can hence be explained with a problem during the fit procedure.

From the evaluation of the ideality factor one can conclude that the fraction of recombination in the space charge region or via the interface is continuously reduced until a Na/In (S/In) ratio of about 0.45 (1.60) is reached. In this composition range, a decrease of the saturation current density might be caused by a reduction of the thermal excitation of electrons from the valence band to the conduction band due to the increasing band gap of the buffer as it can be deduced from the ellipsometer measurements in Fig. 45 and reference [113]. The increasing series resistance of the IDCs indicates a growing barrier for the carrier transport towards higher Na/In (S/In) ratios. From reference [68] it is known that the introduction of Na into the buffer does affect both the conduction band and the valence band. Hence, this effect might be related to an increasing spike at the buffer-absorber interface [30].

6.5 Summarizing discussion and conclusion

Referring to chapter 5.6.2, where a band alignment without any significant band offset has been assumed for an undoped buffer layer with an optimal In-content of 42.0 at%, a certain positive conduction band offset has been discussed to be beneficial for the electrical properties of the solar modules. Since an increasing spike enhances the degree of type-inversion at the absorber's surface, the spatial location of the *pn*-junction is pushed into the absorber layer and hence away from the vast amount of defects at the interface to the buffer [34-36]. Part of this effect could also be associated to the slightly increasing *n*-type character, which has been discussed by Barreau el al. [44]. However, as it has been mentioned in chapter 2.2.1, a positive conduction band offset, exceeding a value of about 0.4 eV, is capable of deteriorating the electrical properties of a solar cell [31, 34, 35].

In the first place, a too large conduction band offset could hamper the current flow across the junction [30]. This would be equivalent to an increase in series resistance and affect the fill factor in a disadvantageous way. Furthermore, it can be expected that a continuously increasing spike is connected to an increasing depth of the burial of the *pn*-junction [115]. Hence, a loss in current density for the blue wavelength region should result at some point since the surface of the absorber features a relatively small band gap. Due to the fact that the high energetic light is absorbed in the interface near region and the mobility of holes is in general smaller than the one of the electrons, the hole transport has a reduced contribution to the total current density. Besides this, the increased number of defects at the buffer-absorber-interface is also expected to hamper the charge carrier transport [115].

Hence, the flattening tendency of the current density above Na/In=0.5 (S/In=1.6) can be explained by these mechanisms.

Since the series resistance of the IDCs is reduced compared to the ones of the DDC's, a significant contribution of photoconductivity becomes obvious. This could be explained by a probable compensation of the *n*-type buffer layer when incorporating more Na. As it has been mentioned in chapter 2.3.3, the chemical composition at grain boundaries might be responsible for the occurrence of photoconductivity [66]. In combination with the already stated accumulation of Na at grain boundaries [121], this explanation becomes plausible. According to the model of Eisgruber et al. [123], a negatively charged acceptor level, i. e. the decorated grain boundary [124], has a larger cross-section for a hole capture than in its neutral state for an electron. This means that the acceptor has a higher tendency to stay neutral. Upon the incidence of a photon and the generation of an electron-hole-pair, the buffer will be electronically pushed towards a more positive charge and the height of the conduction band offset is reduced. Hence, this effect would reduce the series resistance and improve the electrical properties of the solar modules upon light irradiation. To verify this hypothesis, the diode characteristics have been evaluated for the appearance of a cross over, as it has also been done in chapter 5.6.3. Referring to the equivalent evaluation, Fig. 49 shows the calculated difference between the voltage of where the cross over appears and the open circuit voltage in dependence of the Na/In ratio.

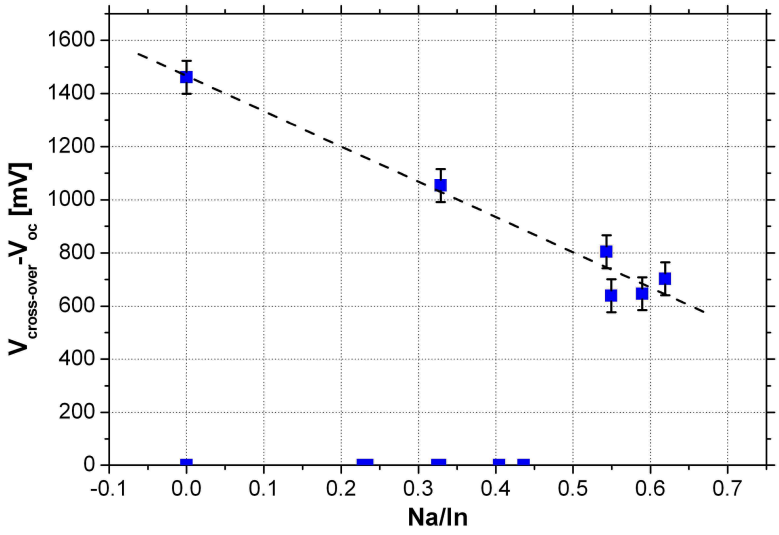

Fig. 49: Distance of the cross over to the open circuit voltage for the respective diode characteristics in dependence on the Na/In ratio (Error in Na/In and $V_{cross\text{-}over}$-V_{oc} equals 0.001 and 17 mV respectively).

Despite the fact that several diode characteristics do not show a cross over in the recorded voltage range, it becomes apparent that the distance of the cross over to the V_{oc} tends to be reduced for increasing Na/In ratios. Due to a limitation of the measurement range to a maximum voltage, some of the possible crossovers might have not been recorded. Nevertheless, due to a changing open circuit voltage and ideality factor in dependence of the Na/In ratio, the calculated difference can still be close to the shown regression line in Fig. 49, if the diode characteristics would have been recorded until higher voltages. As already discussed in chapter 5.6.3, the appearance of a cross over requires the existence of a secondary barrier in the conduction band [30]. Following the argumentation of a relatively flat band alignment for an undoped In_xS_y buffer with an In-content of about 42.0 at%, the tendency towards more pronounced cross overs with increasing Na-contents supports the hypothesis of an increasing spike in the conduction band at the buffer-absorber-interface stated above.

Until now, no reliable measurements have been performed to characterize the conductivity of the $NaIn_xS_y$ layers. However, the increasing band gap already indicates an increasing resistivity [73]. Combining a continuously decreasing conductivity with an increasing photoconductivity, one can also explain the evolution of the shunt resistance. In the dark, an increasingly isolating behaviour can be seen with higher Na/In ratios as the buffer layer's conductivity decreases. Upon irradiation the conductivity increases and lowers the shunt resistance of the solar module.

To summarize the changes in the band alignment described above, Fig. 50 depicts a qualitative sketch of the band alignment for the situations with (dashed line) and without (solid line) the addition of Na_2S to the In_xS_y buffer layer. Effects like a band gap widening towards the surface of the absorber [19] or the possible formation of interface phases [76] have not been taken into account.

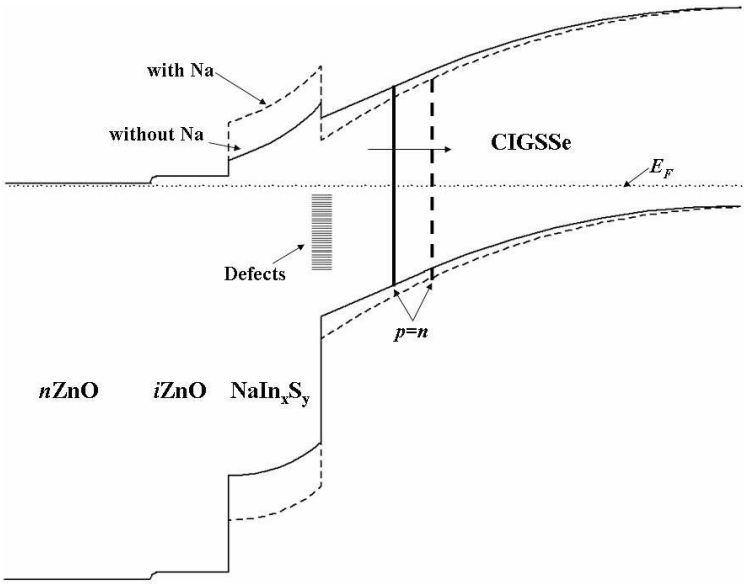

Fig. 50: Qualitative sketch of the changes in the band alignment upon doping of In_xS_y buffer layers with Na_2S (dashed line) compared with the undoped case (solid line).

As discussed above, the introduction of Na into the buffer layer has an effect on both the conduction and the valence band [68] and the *n*-type character is slightly enhanced [44]. Conclusively, the resulting increase in the conduction band offset reduces the respective distance to the Fermi level and shifts the *pn*-junction deeper into the absorber and away from the interface defects [34, 36]. Hence, the amount of interface recombination is reduced, enabling a significant improvement of the gainable conversion efficiency of the respective solar modules.

7 Summary and outlook

Highly efficient thin film solar cells based on CIGSSe require a buffer layer between the absorber layer and the transparent front electrode [23]. Commonly, this task is taken over by a thin CdS layer, deposited by a wet chemical process. However, mostly due to the inherent toxicity of the compound itself and the low productivity of the deposition process, resulting in a reduced compatibility of the process within a large scale production environment, relatively large effort has been conducted to replace this film with an adequate alternative [23, 24, 31]. On the basis of several experiments, the introduction of In_2S_3 as buffer layer has been found to be a promising candidate to replace the CdS buffer. Referring to the present economical situation of the photovoltaic industry, a successful replacement of the buffer layer cannot afford any loss in efficiency of the solar modules. For a successful replacement of the CdS layer it is therefore of essential meaning to understand the crucial dependencies of the predominant effects inside the thin film stack. The present thesis addresses this task and outlines the characteristics and requirements for the alternative material, being relevant for a replacement without any loss in the conversion efficiency of the respective solar modules. In this scope, a detailed analysis of the electrical properties of a series of solar cells and modules is presented and can explain the observed dependencies by changes in the band alignment at the absorber-buffer-interface.

Referring to the properties of the In_2S_3 source material, several characteristics have been identified to be essential for a reproducible and long term stable thermal evaporation process. These are a metal based elemental purity of 99.999 %, an oxygen impurity level below 1.0 wt% and a stoichiometric composition in the tetragonal structure without any phase contaminations. The compliance with the stated requirements is also relevant for the achievement of high conversion efficiencies with the respective solar cells.

As the S/In ratio has been found to be a crucial parameter for the properties of In_xS_y, the deposition process has been refined. In order to vary the S/In ratio of the thin films, several possibilities have been developed within this thesis. The introduced techniques are based on a reduction of the sulphur partial pressure under the utilization of either copper plates or an actively controlled cooling shield inside the vacuum chamber. By applying these techniques it is possible to lower the availability of sulphur during the deposition process and to adjust the composition of the respective films.

By characterizing In_2S_3 source material and decomposed process residuals in Raman spectroscopy, it was possible to identify peak positions for the so far unpublished Raman spectrum of the In_6S_7 phase. This has been done with the help of a comparison of available data from publications for InS and In_2S_3 [104, 105] to the spectrum of the process residuals consisting of In_2S_3, In_6S_7 and InS. Using the knowledge about the different Raman spectra, it has been shown that variations in the S/In ratio in the In-rich regime result in a coexistence of all three phases in thin films on glass. Moreover, an increasing In-content in the thin films has been related to a reduction in the buffer layer's crystallinity. This effect has been attributed to different and incompatible lattice structures of the three phases in connection with a mutual hindering in the respective growth of the individual crystals during deposition.

Besides the structural changes, caused by variations in the S/In ratio, ToF-SIMS analyses indicated an increased amount of Cu and Na to diffuse from the absorber into the buffer layer when the latter is deposited close to its nominal stoichiometry of S/In=3/2. This finding has been confirmed by STEM-EDX measurements. Additionally, the characterization by TEM allowed a quantification of the average grain size in the buffer layers to be in the range of about 10 nm for an In-content of 41.9 at% and 30 nm for an In-content of 40.4 at%. The result supported the analyses and interpretation of the measurements conducted by Raman spectrocopy. Based on the differences found in the structural and chemical changes in dependence of the S/In ratio, it has been concluded that the degree of crystallinity determines the amount of Cu diffusing from the absorber into the buffer layer.

Furthermore, the optical properties of the In_xS_y buffer layers have been characterized by spectroscopic ellipsometry. Both the refractive index and the extinction coefficient strongly depend on the S/In ratio in a way that increasing In-contents result in a stronger absorption and a higher refractive index. Besides this, the evolution of the extinction coefficient clearly shows an indirect band gap for In-contents above 40.5 at%. The width of the band gap has been found to continuously decrease with increasing In-contents. Below 40.5 at%, the band gap discontinuously increases from about 1.8 eV to 2.0 eV and the extinction coefficient features a significantly reduced low energy absorption tail, i. e. an only low difference in energy until a direct transition becomes possible. According to Gödecke et al. [42] this composition marks the phase transition from the tetragonal to the cubic phase of In_2S_3. Since this phase transition is

accompanied with an alteration of the lattice parameters, the observed change becomes plausible.

Moreover, it has been shown that variations in the S/In ratio of the In_xS_y buffer have a significant influence on the electrical properties of fully processed CIGSSe solar cells. For the case of a buffer deposition close to the stoichiometry of In_2S_3, only low conversion efficiencies around 8 % could be obtained. Towards a more In-rich composition, an optimum in the electrical properties has been found at an In-content of about 42.0 at% with solar cell efficiencies of up to 13.6 %. Exceeding this value, also leads to a reduction in the conversion efficiency. A detailed evaluation of the secondary diode parameters and the obtained thin film characterization results made it possible to propose a model that can explain this behaviour:

A buffer layer composition close to its nominal stoichiometry allows an enhanced diffusion of Cu from the absorber into the buffer layer. The diffusion process itself is driven by elevated substrate temperatures during subsequent process steps, i. e. the ZnO window layer deposition. According to observations of other research groups [44, 68, 74, 75], the incorporation of Cu into In_xS_y layers leads to a reduction of the semiconductor's band gap and a loss in charge carrier density. The combination of these effects lowers the band bending from the absorber to the buffer and causes a negative conduction band offset in the band alignment at the absorber-buffer-interface. This results in a loss of type inversion of the absorber's surface and shifts the electronic location of the *pn*-junction to the vicinity of the absorber-buffer-interface. The existence of a vast amount of defects at this location results in an enhanced recombination and deteriorates the conversion efficiency. A lower S/In ratio in the buffer is accompanied by a more fine crystalline structure, which is capable to impede the Cu diffusion from the absorber into the buffer layer. The resulting larger band gap of the buffer avoids the cliff situation and allows a slight inversion of the absorber surface, which pushes the *pn*-junction away from the defect-rich interface into the absorber layer. In this case, a small positive conduction band offset is present at the respective interface. Any further increase of the In-content beyond 42 at% leads to a continuous reduction of the buffer's band gap, leading to an enhanced light absorption in the buffer region and a loss in current density. At the same time, an increasing In-content is accompanied by higher fractions of In_6S_7 and InS. Since these phases have been reported to feature significantly lower charge carrier densities [58, 60, 63, 64], one can conclude that their presence reduces the effective carrier density inside the buffer layer. The consequential reduction

in band bending and positive conduction band offset gradually abolishes the absorber's type inversion and pushes the *pn*-junction back towards the absorber-buffer-interface. Therefore, an increased fraction of interface recombination limits the solar cell efficiency.

Even though a slight inversion of the absorber surface has been found to be present for an optimal S/In ratio, a significant gap between the conversion efficiency of solar cells with an In_xS_y buffer and the ones with a CdS buffer is observed. To close this gap and to optimize the In_xS_y buffer, a doping process based on the implementation of Na_2S has been developed.

Several of the $NaIn_xS_y$ layers have been characterized by Raman, ToF-SIMS, XRD and spectroscopic ellipsometry. The results indicated that the layers maintain a fine crystalline nature, suppressing the diffusion of Cu, while the band gap continuously increases towards higher Na-contents. Furthermore, an accumulation of Na is present at the absorber-buffer-interface. Since other research groups already found that Na is predominantly located at grain boundaries in CIGSe films [121, 122], it is likely that this accumulation is due to the increased defect density amount at such sites. Thus, Na might administer a passivating effect, reducing the amount of electrically active defects, similar to the hydrogenation of polycrystalline thin film silicon [125].

Moreover, an experiment has been conducted during which the buffer's Na/In and S/In ratios have been varied. The respective samples have been fully processed to 10x10 cm² solar modules and were evaluated in their *jV*-characteristics. Based on the analysis of the secondary parameters of these solar modules and the comparison to the characterization results of the respective witness samples, the model for the electronic role of the undoped In_xS_y buffer layers could be extended:

The increasing band gap of the buffer layer partly affects the conduction band [68] and increases the band offset from relatively flat for an undoped In_xS_y film towards an increased positive offset. Furthermore, the implementation of Na slightly enhances the *n*-character of the buffer layer [44], causing an enhanced band bending from the absorber to the buffer. Consistent to the literature [36], the increasing positive band offset leads to a more pronounced inversion of the absorber surface and shifts the *pn*-junction further away from the interface, deeper into the absorber. In this way the contribution of interface-recombination losses is significantly reduced, which has a direct effect on the conversion efficiencies of solar cells and modules. As a result, the efficiency gap between modules with an undoped In_xS_y buffer layer and the reference

module with a CdS buffer layer could be fully closed. The highest efficiency of a module with a CdS-buffer has reached 14.7 %, while the best Cd-free module obtained during this thesis has reached 14.9 %, even slightly surpassing the Cd-containing reference. As it has been emphasized in the introductory chapter, the accomplishment of this goal is an essential requirement for an economically successful replacement of the Cd-containing buffer layer. Moreover, the ecological aspect of the reduction of toxic waste during the production of solar modules is a significant advantage for this process. In general, this result falsifies the historic prerequisite of using a CdS buffer layer for the achievement of high conversion efficiencies.

For future analysis it is of special interest to verify the above described model regarding the band alignment and the evolution of the band offsets in dependence on the buffer's composition. A characterization of stacked absorber-buffer samples by photo electron spectroscopy and electron energy loss spectroscopy is assumed to be able to fulfil this task. For such an analysis it is essential to apply the thermal budget of the ZnO processes to the absorber-buffer stack, which could be simulated by a post-annealing step under vacuum conditions. As outlined by Pistor [43], the elevated substrate temperature initiates the diffusion of elements of the absorber into the buffer, allowing an assessment of the respective influence on the electrical properties inside the solar cell. Despite the consideration of this effect, one still has to be aware that the impact of the sputter processes is not taken into account within this approach. Nevertheless, it is expected that the quantification of the band offsets of both doped and undoped In_xS_y buffer layers is capable of investigating the respective characteristics and to confirm the outlined model. This analysis is planned in collaboration with the University of Würzburg.

Another possible further characterization is the direct determination of the charge carrier density in the buffer layer in dependence of the S/In and the Na/In ratio. As described above, it is expected that an increasing fraction of the In_6S_7 and InS phase is reducing the *n*-type character of the In_xS_y buffer layer. At the University of Jena, several approaches are currently being followed to determine these characteristics by Hall measurements. However, the choice of the substrate and the manufacturing of suitable electrical contacts to the films have been found to be a challenging task which is also currently under investigation. In the same way as for the quantification of the band offsets, the diffused elements from the absorber can be expected to have a

significant influence on the measurement results. To be able to evaluate the impact of Cu in stoichiometric In_2S_3, it might be possible to perform a coevaporation together with Cu or a Cu-containing compound. A direct evaporation of a ternary compound, such as $CuIn_5S_8$, should also be able to fulfil this task.

Referring to the growth of the buffer layer in the direct vicinity of the absorber-buffer-interface, it is not yet clear whether and how differences in the absorber's attributes and the buffer deposition process influence the properties of the solar cells. The formation of an interface phase has already been reported in the literature [126] and might have a significant effect on the electrical properties of the respective solar cells and modules. Hence, a characterization on the nanoscale in a cross section of the buffer region should grant a more detailed comprehension of the film growth processes on the absorber surface.

In connection to the probabilities of efficiency enhancements on the absorber side, it is thinkable to increase the band gap of the absorber at its surface to higher values. This might be done by increasing the sulphur or the gallium content at the respective surface [19]. In this way it should be possible to significantly increase the open circuit voltage [33]. However, since this approach will alter the electronic situation at the buffer-absorber-interface, the band alignment has to be adapted to the new situation. At this point it might be possible that the required amount of Na inside the buffer layer is higher for an optimal band alignment.

Alternatively to the coevaporation of In_2S_3 and Na_2S it might also be desirable to use NaF as dopant. Since it is already known that the fluorine is not incorporated into the In_xS_y layer [72], one could separate the influences of Na/In and S/In and might also find potential for higher efficiencies.

Bibliography

1. Haas, R., *Market deployment strategies for PV systems in the built environment*. 2002, Internationa Energy Agency. p. 94.
2. *Gesetz für den Vorrang erneuerbarer Energien*, Bundesgesetzblatt, Editor. 2000, Bundesministerium der Justiz. p. 305-309.
3. European Photovoltaic Industry Association, *EPIA market report 2011*. 2012: Brussels. p. 1-7.
4. European Photovoltaic Industry Association, *Global market outlook for photovoltaics until 2014*. 2010: Brussels. p. 1-28.
5. Hering, G., *Year of the tiger*, in *Photon International*. March 2011. p. 186-218.
6. Schuessler, B. *Worldwide solar cell production growth flattens but still gigantic in 2011*. 2012 [cited 06.05.13]; Available from: http://www.photon-international.com/news_archiv/details.aspx?cat=News_PI&sub=media&pub=4&parent=4195.
7. Liebreich, M., *Keynote presentation*. 2012, Bloomberg New Energy Finance Summit.
8. Herron, J., *Manufacturing eclipse in 2012*, in *Photon International*. March 2012, Photon International.
9. Bube, R., *Photovoltaic Materials*, ed. R. Newman. Vol. 1. 1998: Imperial College Press. 224.
10. Burger, B., et al., *Photovoltaics Report*. 2012, Fraunhofer ISE: Freiburg. p. 43.
11. Peter, L.M., *Towards sustainable photovoltaics: The search for new materials.* Philosophical transactions of the royal society A, 2011. **369**: p. 1840-1856.
12. Kim, H.C., et al., *Life Cycle Greenhouse Gas Emissions of Thin-film Photovoltaic Electricity Generation.* Journal of Industrial Ecology, 2012: p. 1-12.
13. Delahoy, A.E., et al., *Thin Film CIGS Photovoltaic Technology*. 2000, National Renewable Energy Laboratory. p. 30.
14. Jackson, P., et al., *New world record efficiency for Cu(In,Ga)Se_2 thin-film solar cells beyond 20%.* Progress in Photovoltaics: Research and Applications, 2011. **19**(7): p. 894-897.

15. Schultz, O., S.W. Glunz, and G.P. Willeke, *Multicrystalline silicon solar cells exceeding 20% efficiency.* Progress in Photovoltaics: Research and Applications, 2004. **12**(7): p. 553-558.
16. Green, M.A., et al., *Solar cell efficiency tables (version 41).* Progress in Photovoltaics: Research and Applications, 2013. **21**(1): p. 1-11.
17. Benagli, S., et al. *High-Efficiency Amorphous Silicon Devices on LPCVD-ZnO TCO Prepared in Industrial KAI TM-M R&D Reactor*. in *24th European Photovoltaic Solar Energy Conference*. 2009. Hamburg.
18. Meyer, T. *First Solar Sets New World Record for CdTe Solar Cell Efficiency*. 2013 [cited 02.05.13]; Available from: http://investor.firstsolar.com/releasedetail.cfm?ReleaseID=743398.
19. Palm, J., et al., *CIGSSe thin film PV modules: from fundamental investigations to advanced performance and stability.* Thin Solid Films, 2004. **451-452**(0): p. 544-551.
20. Dalibor, T., et al., *Towards module efficiencies of 16 % with an imporved CIGSSe device design*, in *EU PVSEC 2011*. 2011, AVANCIS GmbH & Co. KG: Hamburg, Germany.
21. *TSMC Solar Module in voller Größe (1.09 m²) stellen Rekord für CIGS-Effizienz von 15.7% auf.* [Press release] 2013 [cited 27.06.13]; Available from: http://www.tsmc-solar.com/Assets/downloads/de-DE/TSMC_Solar_PRESSEMITTEILUNG_DE_Jun_18_2013.pdf.
22. Grünerbl, M., *Measurements at AVANCIS*. 2013.
23. Naghavi, N., et al., *Buffer layers and transparent conducting oxides for chalcopyrite Cu(In,Ga)(S,Se)$_2$ based thin film photovoltaics: present status and current developments.* Progress in Photovoltaics: Research and Applications, 2010. **18**(6): p. 411-433.
24. Hariskos, D., S. Spiering, and M. Powalla, *Buffer layers in Cu(In,Ga)Se$_2$ solar cells and modules.* Thin Solid Films, 2005. **480-481**: p. 99–109.
25. Hariskos, D., et al., *Chemical bath deposition of CdS buffer layer: prospects of increasing materials yield and reducing waste.* Thin Solid Films, 2001. **387**(1-2): p. 179-181.
26. Seyrling, S., et al., *CuIn$_{1-x}$GaxSe$_2$ growth process modifications: Influences on microstructure, Na distribution, and device properties.* Solar Energy Materials and Solar Cells, 2011. **95**(6): p. 1477-1481.

27. Green, M.A., et al., *Solar cell efficiency tables (version 39).* Progress in Photovoltaics: Research and Applications, 2011. **20**(1): p. 12-20.

28. Palm, J., et al., *Raman spectroscopy for quality control and process optimization of chalcopyrite thin films and devices.* Thin Solid Films, 2007. **515**(15): p. 5913-5916.

29. Sterner, J., J. Malmström, and L. Stolt, *Study on ALD In_2S_3/Cu(In,Ga)Se_2 interface formation.* Progress in Photovoltaics: Research and Applications, 2005. **13**(3): p. 179-193.

30. Pudov, A.O., *Impact of secondary barriers on $CuIn_{1-x}GaxSe_2$ solar-cell operation*, in *Department of Physics*. 2005, Colorado State University: Fort Collins, Colorado.

31. Fischer, C.H., et al., *Interface engineering in chalcopyrite thin film solar devices.* Solar Energy Materials and Solar Cells, 2006. **90**(10): p. 1471-1485.

32. Bernéde, J.C., et al., *Band alignment at β-In_2S_3/TCO interface.* Applied Surface Science, 2002. **195**(1-4): p. 222-228.

33. Gloeckler, M. and J.R. Sites, *Efficiency limitations for wide-band-gap chalcopyrite solar cells.* Thin Solid Films, 2005. **480-481**(0): p. 241-245.

34. Klenk, R., *Characterisation and modelling of chalcopyrite solar cells.* Thin solid films, 2001. **387**: p. 135-140.

35. Minemoto, T., et al., *Cu(In,Ga)Se_2 solar cells with controlled conduction band offset of window/Cu(In,Ga)Se_2 layers.* Journal of Applied Physics, 2001. **89**(12): p. 8327-8330.

36. Shafarman, W. and L. Stolt, *Cu(InGa)Se_2 Solar Cells*, in *Handbook of photovoltaic science and engineering*, A. Luque and S. Hegedus, Editors. 2003, John Wiley & Sons Ltd. p. 567-616.

37. D. Hariskos, S.S., M. Powalla, *Buffer layers in Cu(In,Ga)Se_2 solar cells and modules.* Thin Solid Films, 2005. **480-481**: p. 99– 109.

38. Erfurth, F., et al., *Chemical structure of the (Zn_{1-x},Mg_x)O/CuIn(S,Se)$_2$ interface in thin film solar cells* Applied Physics Letters, 2009. **95**(12): p. 122104 - 122104-3.

39. Fischer, C.-H., et al., *The spray-ILGAR® (ion layer gas reaction) method for the deposition of thin semiconductor layers: Process and applications for thin film solar cells.* Solar Energy Materials and Solar Cells, 2011. **95**(6): p. 1518-1526.

40. Duffin, W.J. and J.H.C. Hogg, *Crystalline phases in the system In-In_2S_3.* Acta Crystallographica, 1966. **20**(4): p. 566-569.

41. King, G., *The space group of β-In_2S_3.* Acta Crystallographica, 1962. **15**(5): p. 512.

42. Gödecke, T. and K. Schubert, *On the phase diagram InS_M.* Z. Metallkd., 1985. **76**: p. 568-364.

43. Pistor, P., *Formation and electronic properties of In_2S_3 / Cu(In,Ga)Se_2 junctions and related thin film solar cells*, in *Physik*. 2009, Freie Universität Berlin: Berlin. p. 174.

44. Barreau, N., *Indium sulfide and relatives in the world of photovoltaics.* Solar Energy, 2009. **83**(3): p. 363-371.

45. Diehl, R. and R. Nitsche, *Vapour growth of three In_2S_3 modifications by iodine transport.* Journal of Crystal Growth, 1975. **28**(3): p. 306-310.

46. Hahn, H. and W. Klingler, *Über die Kristallstrukturen des In_2S_3 und In_2Te_3.* Zeitschrift für anorganische Chemie, 1949. **260**(1-3): p. 97-109.

47. Diehl, R., C.D. Carpentier, and R. Nitsche, *The crystal structure of γ-In_2S_3 stabilized by As or Sb.* Acta Crystallographica Section B, 1976. **32**(4): p. 1257-1260.

48. Hogg, J.H.C. and W.J. Duffin, *The crystal structure of In_6S_7.* Acta Crystallographica, 1967. **23**(1): p. 111-118.

49. Schubert, K., E. Dörre, and E. Günzel, *Kristallchemische Ergebnisse an Phasen aus B-Elementen.* Naturwissenschaften, 1954. **41**(19): p. 448-448.

50. Nishino, T. and Y. Hamakawa, *Preparation and properties of InS single crystals.* Japanese Journal of Appliend Physics, 1977. **16**(8): p. 1291-1300.

51. Yoshida, T., *Chemical bath deposition of band gap tailored indium sulfide thin films*, in *Photoelectrochemistry*, Rajeshwar, et al., Editors. 1997, The Electrochemical Society, Inc. p. 37-57.

52. Barreau, N., et al., *Evolution of CBD-$In(OH)_xS_y$ thin film band structure with its optical band gap*, in *Chemical solution deposition of semiconducting and non-metallic films*, D. Lincot and G. Hodes, Editors. 2006, The Electrochemical Society Inc. p. 82-88.

53. Naghavi, N., et al., *Growth studies and characterisation of In_2S_3 thin films deposited by atomic layer deposition (ALD).* Applied Surface Science, 2004. **222**(1-4): p. 65-73.

54. Rehwald, W. and G. Harbeke, *On the conduction mechanism in single crystal β-indium sulfide In_2S_3.* Journal of Physics and Chemistry of Solids, 1965. **26**(8): p. 1309-1324.

55. Barreau, N., et al., *Bandgap properties of the indium sulfide thin-films grown by co-evaporation.* Thin Solid Films, 2009. **517**(7): p. 2316-2319.

56. Herrero, J. and J. Ortega, *n-Type In_2S_3 thin films prepared by gas chalcogenization of metallic electroplated indium: Photoelectrochemical characterization.* Solar Energy Materials, 1988. **17**(5): p. 357-368.

57. Verma, R., *Vacuum evaporated In_2S_3 buffer layer for Cu(In, Ga)Se_2 thin film solar cell*. 2010, Eidgenössische Technische Hochschule (ETH): Zürich. p. 171.

58. Gamal, G.A., *On the conduction mechanism and thermoelectric phenomena in In_6S_7 layer crystals.* Crystal Research and Technology, 1997. **32**(5): p. 723-731.

59. Ching-Hwa, H., W. Yi-Ping, and H. Ying-Sheng, *Optical characterization of band-edge property of In_6S_7 compound.* Applied Physics Letters. **100**(13): p. 131905.

60. Seyam, M.A.M., *Optical and electrical properties of indium monosulfide (InS) thin films.* Vacuum, 2001. **63**(3): p. 441-447.

61. Yoosuf, R. and M.K. Jayaraj, *Optical and photoelectrical properties of β-In_2S_3 thin films prepared by two-stage process.* Solar Energy Materials and Solar Cells, 2005. **89**(1): p. 85-94.

62. Al-Orainy, R.H., et al., *Transport properties of hexaindium Heptasulfide single crystals.* Australian Journal of Basic and Applied Sciences, 2011. **5**(6): p. 6-13.

63. Qasrawi, A.F. and N.M. Gasanly, *Acoustic phonons scattering mobility and carrier effective mass in In_6S_7 crystals.* Journal of Alloys and Compounds, 2006. **426**(1-2): p. 64-66.

64. Qasrawi, A.F. and N.M. Gasanly, *Carrier Transport Properties of InS Single Crystals.* Crystal Research and Technology, 2002. **37**(10): p. 1104-1112.

65. Asikainen, T., M. Ritala, and M. Leskelä, *Growth of In_2S_3 thin films by atomic layer epitaxy.* Applied Surface Science, 1994. **82-83**(0): p. 122-125.

66. Jayakrishnan, R., et al., *Do the grain boundaries of β-In_2S_3 thin films have a role in sub-band-gap photosensitivity to 632.8 nm?* Journal of Applied Physics, 2008. **103**(5): p. 053106.

67. Barreau, N., et al., *New Cd-free buffer layer deposited by PVD: In_2S_3 containing Na compounds.* Thin Solid Films, 2003. **431-432**(0): p. 326-329.

68. Lafond, A., et al., *Structural study and electronic band structure investigations of the solid solution $Na_xCu_{1-x}In_5S_8$ and its impact on the $Cu(In,Ga)Se_2/In_2S_3$ interface of solar cells.* Thin Solid Films, 2007. **515**(15): p. 6020-6023.

69. Barreau, N., et al., *Structural, optical and electrical properties of β-$In_2S_{3-3x}O_{3x}$ thin films obtained by PVD.* Thin Solid Films, 2002. **403-404**(0): p. 331-334.

70. Bär, M., *Depostion of In_2S_3 on $Cu(In, Ga)(S,Se)_2$ thin film solar cell absorbers by spray ion layer gas reaction: Evidence of strong interfacial diffusion.* Applied physics letters, 2007. **90**: p. 132118-2 - 132118-3.

71. Gall, S., et al., *Material analysis of PVD-grown indium sulphide buffer layers for $Cu(In,Ga)Se_2$-based solar cells.* Thin Solid Films, 2005. **480 - 481**(0): p. 138-141.

72. Barreau, N., et al., *Study of the new β-In_2S_3 containing Na thin films Part I: Synthesis and structural characterization of the material.* Journal of Crystal Growth, 2002. **241**(1-2): p. 4-14.

73. Barreau, N., J.C. Bernède, and S. Marsillac, *Study of the new β-In_2S_3 containing Na thin films. Part II: Optical and electrical characterization of thin films.* Journal of Crystal Growth, 2002. **241**(1-2): p. 51-56.

74. Barreau, N. and M. Tessier. *Characterization of Indium Sulfide Thin Films Containing Copper*. in *MRS spring meeting*. 2009. San Francisco.

75. Barreau, N., et al., *A study of bulk $Na_xCu_{1-x}In_5S_8$ and its impact on the $Cu(In,Ga)Se_2/In_2S_3$ interface of solar cells.* Solar Energy Materials & Solar Cells, 2006. **90**: p. 1840 - 1848.

76. Abou-Ras, D., et al., *Structural and chemical analyses of sputtered In_xS_y buffer layers in $Cu(In,Ga)Se_2$ thin-film solar cells.* Thin Solid Films, 2009. **517**(8): p. 2792-2798.

77. Emery, K., *Measurement and characterization of solar cells and modules*, in *Handbook of photovoltaic, science and engineering*, A. Luque and S. Hegedus, Editors. 2003, Wiley. p. 701-746.

78. Gray, J.L., *The Physics of the Solar Cell*, in *Handbook of photovoltaic, science and engineering*, A. Luque and S. Hegedus, Editors. 2003, Wiley. p. 61-111.

79. Burgers, A.R., et al. *Improved treatment of the strongly varying slope in fitting solar cell I-V curves* in *25th IEEE Photovoltaics Specialists Conference*. 1996. Washington D. C.

80. Schroder, D., *Semiconductor materials and device characterization*. 3 ed. 2006: John Wiley & Sons. 779.

81. Shockley, W. and H.J. Queisser, *Detailed balance limit of efficiency of pn junction solar cells* Journal of applied physics, 1961. **32**(3): p. 510-519.

82. Kirchartz, T., K. Ding, and U. Rau, *Fundamental electrical characterization of thin film solar cells*, in *Advanced characterization techniques for thin film solar cells*, D. Abou-Ras, Editor. 2011, Wiley-VCH. p. 35-60.

83. Abou-Ras, D., *Electron microscopy on thin films for solar cells*, in *Advanced characterization techniques for thin film solar cells*, D. Abbou-Ras, Editor. 2011, Wiley-VCH. p. 299-345.

84. Bruker-AXS, *S8 Tiger - Spectrometry solutions*. 2008.

85. Haken, H. and H.C. Wolf, *Atom- und Quantenphysik*. 8 ed. 2004, Berlin, Heidelberg, New York: Springer-Verlag. 531.

86. Tauc, J. and A. Menth, *States in the gap.* Journal of Non-Crystalline Solids, 1972. **8-10**: p. 569-585.

87. Qasrawi, A.F., *Refractive index, band gap and oscillator parameters of amorphous GaSe thin films.* Crystal Research and Technology, 2005. **40**(6): p. 610-614.

88. Sanz, C., C. Guillén, and M.T. Gutiérrez, *Study of preparation parameters for indium sulfide thin films obtained by modulated flux deposition.* Thin Solid Films, 2006. **511-512**(0): p. 121-124.

89. Asenjo, B., et al., *Indium sulfide buffer layers deposited by dry and wet methods.* Thin Solid Films, 2007. **515**(15): p. 6041-6044.

90. Marsillac, S., et al., *Spectroscopic Ellipsometry*, in *Acvanced characterization techniques for thin film solar cells*, D. Abou-Ras, T. Kirchartz, and U. Rau, Editors. 2011, Wiley-VCH. p. 125-149.

91. Röseler, A. and B. Gruska, *Ellipsometry*, SENTECH Instruments GmbH. p. 1-12.

92. Meschede, D., *Gerthsen Physik*. 21 ed. 2002: Springer. 1288.

93. *The Nobel Prize in Physics 1930.* 1930 [cited 13.01.13]; Available from: http://www.nobelprize.org/nobel_prizes/physics/laureates/1930/.

94. Àlvarez-Garcia, J., *Raman spectroscopy on thin films for solar cells*, in *Advanced characterization techniques for thin film solar cells*, D. Abbou-Ras, Editor. 2011, Wiley-VCH. p. 365-386.

95. Kittel, C., *Einführung in die Festkörperphysik*. 13 ed. 2002: Oldenburg Wissenschaftsverlag GmbH.

96. Abbou-Ras, D., *Electron microscopy on thin films for solar cells*, in *Advanced characterization techniques for thin film solar cells*, D. Abbou-Ras, Editor. 2011, Wiley-VCH. p. 299-345.

97. Hoffmann, V., et al., *Elemental Distribution profiling of thin films for solar cells*, in *Advanced Characterization techniques for thin film solar cells*, D. Abou-Ras, T. Kirchartz, and U. Rau, Editors. 2011, Wiley -VCH. p. 411 - 448.

98. Susan Schorr, et al., *X-Ray and neutron diffraction on materials for thin film solar cells*, in *Acvanced characterization techniques for thin film solar cells*, D. Abou-Ras, Editor. 2011, Wiley-VCH. p. 347-363.

99. Miller, A.R. and A.W. Searcy, *The sublimation of indium sesquisulfide1*. The Journal of Physical Chemistry, 1963. **67**(11): p. 2400-2404.

100. Ferro, D., V. Piacente, and P. Scardala, *Sublimation behaviour of indium trisulphide studied by a simultaneous torsion and Knudsen technique.* Journal of Materials Science Letters, 1988. **7**(12): p. 1301-1304.

101. Palm, J., et al., *Vorrichtung und Verfahren zum Abscheiden einer Schicht auf einem Substrat*. 2011, European Patent Office: Patent nr.: PCT/EP2011/052609

102. *Material safety data sheet*. 2009 [cited 13.01.13]; Available from: http://www.alfa.com/content/msds/english/45563.pdf.

103. Pohlner, S., et al., *Schichtsystem für Dünnschichtsolarzellen mit Indiumsulfid-Pufferschicht*. 2013, European Patent Office: Application nr: EP 13173945.0.

104. Kambas, K., J. Spyridelis, and M. Balkanski, *Far Infrared and Raman Optical Study of α- and β-In_2S_3 Compounds.* physica status solidi (b), 1981. **105**(1): p. 291-296.

105. Faradzhev, F.E., et al., *Pressure dependence of the Raman spectra of indium sulphide.* Solid State Communications, 1981. **39**(4): p. 587-589.

106. Quiroga-González, E., et al., *Transmission Electron Microscopy Study of Copper Containing Spinel-type In_2S_3 Nanocrystals Prepared by Rapid Pyrolysis of a Single Molecular Precursor.* Zeitschrift für anorganische und allgemeine Chemie, 2010. **636**(13-14): p. 2413-2421.

107. Niesen, T., *Etching of ZnO using diluted acetic acid*. 2010. p. Personal communication.

108. Knoke, I. 2011, Friedrich-Alexander University Nürnberg-Erlangen.

109. Jellison, G.E. and F.A. Modine, *Parameterization of the optical functions of amorphous materials in the interband region.* Applied Physics Letters, 1996. **69**(3): p. 371 - 373

110. Papula, L., *Mathematische Formelsammlung*. 7 ed. 2001: Vieweg. 496.

111. Abdallah, H.B. and R. Bennaceur, *Electronic structure of the hexaindium heptasulfide In_6S_7.* Physica B: Condensed Matter, 2006. **382**(1-2): p. 181-188.

112. Strohm, A., et al., *ZnO/In_xS_y/Cu(In,Ga)Se_2 solar cells fabricated by coherent heterojunction formation.* Thin Solid Films, 2005. **480-481**: p. 162-167.

113. Sze, S.M. and K.N. Kwok, *Physics of semiconductor devices*. 3 ed. 2007: John Wiley & Sons. 815.

114. Ho, C.H., et al., *Temperature-dependent photoconductivity in β-In_2S_3 single crystals.* Journal of Applied Physics, 2010. **108**(4): p. 043518-1 - 043518-4.

115. Hengel, I., *Ladungsträgertransport und Rekombinationsmechanismen in Chalkopyrit-Dünnschichtsolarzellen*, in *Pysik*. 2000, Freie Universität Berlin: Berlin. p. 105.

116. Saad, M. and A. Kassis, *Effect of interface recombination on solar cell parameters.* Solar Energy Materials and Solar Cells, 2003. **79**(4): p. 507-517.

117. S. M. Sze, K.K.N., *Physics of semiconductor devices*. 3 ed. 2007: John Wiley & Sons. 815.

118. Malmström, J., *On generation an recombination in Cu(In, Ga)Se_2 thin-film solar cells*, in *Faculty of science and technology*. 2005, Uppsala University: Uppsala. p. 112.

119. Gnauk, M. 2012, Friedrich-Schiller-University Jena.

120. Pohlner, S., et al., *Schichtsystem für Dünnschichtsolarzellen mit Natriumindiumsulfid-Pufferschicht*. 2013, European Patent Office: Application nr.: EP13173956.7.

121. Cadel, E., et al., *Atom probe study of sodium distribution in polycrystalline Cu(In,Ga)Se_2 thin film.* Acta Materialia, 2010. **58**(7): p. 2634-2637.

122. Cojocaru-Miredin, O. *Characterization of CIGS grain boundaries using Atom Probe Tomography*. in *Photovoltaic Specialists Conference*. 2011. Seatle: 37th IEEE.

123. Eisgruber, I.L., et al., *Blue-photon modification of nonstandard diode barrier in $CuInSe_2$ solar cells.* Solar Energy Materials and Solar Cells, 1998. **53**(3-4): p. 367-377.

124. Weis, T., *Modellstudien zum Ladungsträgertransport über Korngrenzen in photovoltaischen Materialien*, in *Hahn-Meitner-Institut*. 1999, Freie Universität Berlin: Berlin. p. 100.

125. Honda, S., et al., *Hydrogenation of polycrystalline silicon thin films.* Thin Solid Films, 2006. **501**(1-2): p. 144-148.

126. Schmid, D., et al., *Chalcopyrite/defect chalcopyrite heterojunctions on the basis of $CuInSe_2$.* Journal of Applied Physics, 1993. **73**(6): p. 2902-2909.

Acknowledgements

In the first place my gratitude goes out to Prof. Dr. Carsten Ronning for accepting me as a PhD student and for your continuous support. Thank you also for proof reading this thesis and for the hints on how to improve it. In the same place I would like to express my appreciation to Prof. Dr. Gerhard Franz and Prof. Dr. Friedrich Reinert who agreed to act as co-examiner for this thesis.

I would also like to express my gratitude to Dr. Jörg Palm who made it possible to realize my intent to write this thesis. Thank you very much for your support throughout this topic, for all the discussions, ideas and hints on this work and for enabling the possibility to use the generated data within the cooperation with the University of Jena. Thank you also to Heike Degen and Dr. Franz Karg for the support regarding this topic.

Another major thanks goes to Dr. Roland Dietmüller and Dr. Thomas Happ for proof reading this thesis and for all the discussions and hints on it. It's a pleasure to work with you.

In the following I would like to thank everybody who supported me during the scope of this thesis with their work done, the hints and the numerous discussions lead throughout the different topics:

- Thierry Cretin from Saint Gobain Recherche for all SIMS measurements
- Dr. Patrick Eraerds for highly valuable discussions and for the cross-checking of the *jV*-data
- Martin Gnauk from the University of Jena for all discussions, support and EQE measurements
- Dr. Stefan Jost for all discussions and the contribution to the presence of different phases in indium sulphide
- Dr. Ulrike Hermeking-Göbel and Dr. Herbert Göbel from Laboratorium für kristallographische Analytik for all XRD measurments
- Dr. Isabel Knoke from the University of Erlangen for all TEM measurements
- Michael Wendl for your continuous support on the XRF tool and for all calibrations on this system
- The characterization group for discussions, *jV*-measurements and the work done on these tools: Dr. Alejendro Avellan, Dr. Peter Borowski, Dr. Felix Braun,

Dr. Thomas Dalibor, Manfred Grünerbl, Mila Limunovic, Jasna Maksimovic, Christian Schubbert

- The pilot-line- and process-development-group also for discussions and for the allocation of all related processes for the preparation of all solar cells and modules: Ralf Blockus, Rainer Emmer, Martin Fürfanger, Andreas Heiß, Detlef Helmeke, Harald Langer, Dr. Robert Lechner, Denis Lemke, August Lerchenberger, Dr. Thomas Niesen, Markus Micossi, Perka Prastalo, Reinhard Rasch, Sebastian Sarrach, Andreas Schmid, Eduard Schrag, Falk Schubert, Klaus Stießberger, Dr. Rajneesh Verma, Dr. Sven Visbeck, Helmut Vogt, Michael Wendl

Abbreviations and symbols

ALD	Atomic layer deposition
AM	Air mass
a-Si	Amorphous silicon
CBD	Chemical bath deposition
CIGSSe	Copper, indium, gallium, sulphur, selenium
DDC	Dark diode characteristic
EDX	Energy dispersive X-ray spectroscopy
EELS	Electron energy loss spectroscopy
EPBT	Energy payback time
EQE	External quantum efficiency
FIB	Focused ion beam
FWHM	Full width at half maximum
GIXRD	Gracing incidence X-ray diffraction
HR-TEM	High resolution transmission electron microscopy
IDC	Illuminated diode characteristic
ILGAR	Ion-layer gas reaction
mc-Si	Multicrystalline silicon
MPP	Maximum power point
MSE	Mean square error
ODR	Orthogonal distance regression
Oh	Octahedral site
PV	Photovoltaic
PVD	Physical vapour deposition
RBS	Rutherford backscattering
SIMS	Secondary ion mass spectroscopy
SLG	Soda lime glass
SGR	Saint Gobain Recherche
STEM	Scanning transmission electron microscopy
Td	Tetrahedral site
ToF	Time of flight
TL	Tauc-Lorentz-Oscillator
UPS	Ultraviolet photoelectron spectroscopy

USP	Ultrasonic spray pyrolysis
UV/VIS	Ultraviolet / visible
WDX	Wavelength dispersive X-ray spectroscopy
XPS	X-ray photoelectron spectroscopy
XRD	X-ray diffraction
XRF	X-ray fluorescence spectroscopy

A	Prefactor in the Tauc-Lorentz-oscillator
d	Layer thickness, lattice distance
E_0	Field vector, peak in the combined density of states
ΔE_c	Conduction band offset
E_g	Band gap
h	Planck constant
j	Current density
j_0	Saturation current density
j_{lt}	Light generated current density
j_{MPP}	Current density at maximum power point
j_{sc}	Short circuit current density
FF	Fill factor
k	Extinction coefficient
k_B	Boltzmann constant
n	Ideality factor, refractive index
N	Complex refractive index
p_{in}	Power density
Q_e	External quantum efficiency
q	Elementary electric charge
r_p, r_s	Parallel and perpendicular complex amplitude reflection coefficients
R_s	Series resistance
R_{sh}	Shunt resistance
T	Temperature
V	Voltage
V_{oc}	Open circuit voltage
V_{MPP}	Voltage at maximum power point

α	Absorption coefficient
$\varepsilon_{1,2}$	Real and imaginary part of the dielectric function
$\varepsilon_1(\infty)$	High frequency dielectric constant
η	Conversion efficiency
λ	Wavelength
ν	Frequency
ω	Angular frequency
Γ	Broadening factor in a Tauc-Lorentz-oscillat
Δ	Ellipsometric parameter
Θ	Glance angle; heavy side theta function
Φ	Photon flux
Φ_i, Φ_t	Angles of incidence and transmission
Ψ	Ellipsometric parameter
□	Vacancy

Ehrenwörtliche Erklärung

Ich erkläre hiermit ehrenwörtlich, dass ich die vorliegende Arbeit selbständig, ohne unzulässige Hilfe Dritter und ohne Benutzung anderer als der angegebenen Hilfsmittel und Literatur angefertigt habe. Die aus anderen Quellen direkt oder indirekt übernommenen Daten und Konzepte sind unter Angabe der Quelle gekennzeichnet.

Bei der Auswahl und Auswertung folgenden Materials haben mir die nachstehend aufgeführten Personen in der jeweils beschriebenen Weise unentgeltlich geholfen. Alle finanziellen Aufwendungen für Auftragsanalysen und Kooperationen wurden durch AVANCIS getragen.

- Prozessierung aller nicht den Puffer betreffenden Fertigungsschritte der gezeigten Solarzellen und Solarmodule durch Mitarbeiter von AVANCIS
- Charakterisierung aller Solarzellen und Solarmodule bzgl. ihrer *jV*-Kennlinien durch Mitarbeiter von AVANCIS
- Erste Charakterisierungen zur Präsenz von Sekundärphasen in In_xS_y mittels Raman Spektroskopie in Zusammenarbeit mit Dr. Stefan Jost (AVANCIS)
- Durchführung aller TEM-Messungen durch Dr. Isabel Knoke an der Friedrich-Alexander University Nürnberg-Erlangen innerhalb der Forschungsgruppe von Prof. Dr. Erdmann Spiecker
- Durchführung aller EQE-Messungen durch Martin Gnauk an der Friedrich-Schiller-Universität Jena innerhalb der Forschungsgruppe von Prof. Dr. Carsten Ronning
- Durchführung aller SIMS-Messungen durch Thierry Cretin bei Saint Gobain Recherche in Paris
- Durchführung aller XRD-Messungen durch Dr. Ulrike Hermeking-Göbel und Dr. Herbert Göbel im Laboratorium für kristallographische Analytik in München
- Durchführung aller RBS-Messungen durch Dr. Wolfgang Hösler bei Siemens Corporate Research and Technologies in München
- Durchführung aller Analysen zur Stöchiometrie von In_2S_3-Quellmaterial über Titration durch Mitarbeiter von Currenta.

- Durchführung aller RFA-Messungen zur Bestimmung der Elementreinheit von In_2S_3-Quellmaterial und Abschätzung der Informationstiefe der In-L_α-Strahlung an In_2S_3-Tabletten durch Dr. Manfred Schuster und Dr. Matthias Honal bei Siemens Corporate Research and Technologies in München
- Durchführung aller RFA-Kalibrierungen durch Michael Wendl (AVANCIS)

Weitere Personen waren an der inhaltlich-materiellen Erstellung der vorliegenden Arbeit nicht beteiligt. Insbesondere habe ich hierfür nicht die entgeltliche Hilfe von Vermittlungs- bzw. Beratungsdiensten (Promotionsberater oder andere Personen) in Anspruch genommen. Niemand hat von mir unmittelbar oder mittelbar geldwerte Leistungen für Arbeiten erhalten, die im Zusammenhang mit dem Inhalt der vorgelegten Dissertation stehen.

Die Arbeit wurde bisher weder im In- noch im Ausland in gleicher oder ähnlicher Form einer anderen Prüfungsbehörde vorgelegt.

Die geltende Promotionsordnung der Physikalisch-Astronomischen Fakultät ist mir bekannt.

Ich versichere ehrenwörtlich, dass ich nach bestem Wissen die reine Wahrheit gesagt und nichts verschwiegen habe.

Ort, Datum Unterschrift d. Verfassers